Inductively Coupled Plasma Mass Spectrometry

Yan Hu, Frédéric Moynier

Inductively Coupled Plasma Mass Spectrometry

Yan Hu*,[1] and Frédéric Moynier*,[1]

1. Université Paris Cité, Institut de Physique du Globe de Paris, CNRS, UMR 7154, Paris 75005, France

Text: 20748 words

Figures: 29

Keywords: Inductively coupled plasma; Mass spectrometry; Nebulization; Detectors; Spectral interferences; Collision/reaction cell; Instrumental isotope fractionation; Isotope analyses

Key points:

-History of ICP-MS

-Presentation of the essential components of ICP-MS

-How to overcome analytical interferences

-How to correct for instrumental mass bias

*Corresponding authors' emails: yanhu@ipgp.fr; moynier@ipgp.fr

Contents

Abstract

Inductively coupled plasma mass spectrometry (ICP-MS) has grown tremendously since its introduction in 1980, owing to its multi-element and isotopic analytical capability with flexible sample introduction, high sensitivity, and fast sample throughput. In particular, integrating ICP with a magnetic sector mass spectrometer and multiple collectors significantly improves the precision of isotopic analysis for many elements that are difficult to measure with alternative techniques. This chapter reviews the history of ICP-MS, its fundamental principles, and its development for measuring concentrations and isotope ratios of elements prepared in aqueous solutions. The review highlights critical technical advancements, novel approaches to address spectral interferences, and the geochemical and cosmochemical applications that emerged from these advances. Finally, potential avenues for future research are discussed.

1 Introduction

Over the past four decades, inductively coupled plasma mass spectrometry (ICP-MS) has become the quintessential tool for analyzing the concentration and isotopic composition of most elements across the Periodic Table. The ICP source features high efficiency for element ionization with simple and flexible sample introduction (e.g., Houk et al., 1980; Houk 1986). The analytical strength of ICP-MS is further enhanced by coupling with a multi-collector array for simultaneous detection of different isotopes separated by a magnetic sector (i.e., MC-ICP-MS, Walder and Freedman 1992; Walder et al., 1993), which provides sensitive and precise isotopic ratio measurements at high sample throughput (e.g., Halliday et al., 1995; Hirata 1996; Vanhaecke et al., 1996; Belshaw et al., 1998; Halliday et al., 1998; Maréchal et al., 1999).

The development of MC-ICP-MS has profoundly facilitated the isotopic measurement of elements with high first ionization energies (Fig. 1) and low natural abundances, such as Hf (e.g., Blichert-Toft and Albarède 1997; Blichert-Toft et al., 1997), Zr (e.g., Schönbächler et al., 2004; Inglis et al., 2018; Tompkins et al., 2020; He et al., 2021), W (e.g., Lee and Halliday 1995; Lee and Halliday 1995; Yin et al., 2002; Kleine and Walker 2017), Fe (e.g., Belshaw et al., 2000; Zhu et al., 2000; Weyer and Schwieters 2003; Dauphas et al., 2004), Ru (e.g., Becker et al., 2002; Hopp et al., 2016), Os (e.g., Schoenberg et al., 2000; Norman et al., 2002; Nozaki et al., 2012; Ohta et al., 2022), Ni (e.g., Moynier et al., 2007; Gueguen et al., 2013), Zn (e.g., Maréchal et al., 1999; Luck et al., 2005), Cd (Wombacher et al., 2003; Cloquet et al., 2005; Ripperger and Rehkämper 2007), Hg (e.g., Evans et al., 2001; Lauretta et al., 2001; Chen et al., 2010; Geng et al., 2018), Si (e.g., De La Rocha 2002; Cardinal et al., 2003; Georg et al., 2006; van den Boorn et al., 2006), Ge (e.g., Hirata 1997; Luais et al., 2000; Rouxel et al., 2006; Siebert et al., 2006), Sn (e.g., Clayton et al., 2002; Moynier et al., 2009; Balliana et al., 2013; Yamazaki et al., 2013; Creech et al., 2017; Wang et al., 2017; She et al., 2023), Mo (e.g., Anbar et al., 2001; Siebert et al., 2001; Wieser et al., 2007), Se (e.g., Rouxel et al., 2002; Elwaer and Hintelmann 2008; Zhu et al., 2008), and Te (Lee and Halliday 1995; Fehr et al., 2004; Fornadel et al., 2014; Brennecka et al., 2017; Hellmann et al., 2020).

MC-ICP-MS is the preferred method for isotopic analyses of elements with less than four stable isotopes, for which instrumental isotope fractionation cannot be corrected by the conventional double-spike method used in thermal ionization mass spectrometry (TIMS). A critical limitation of TIMS is that the isotope ratio changes progressively as an analysis proceeds. This fractionation occurs because samples are loaded as salts and heated on a metal filament, with light isotopes being preferentially evaporated and ionized. In contrast, sample solutions are

continuously aspirated into the MC-ICP-MS during an analysis, leading to a relatively time-independent instrumental isotope fractionation that can be corrected by external normalization. Furthermore, MC-ICP-MS has a higher sample throughput than TIMS. These analytical advantages of MC-ICP-MS have contributed significantly to the development of isotope geochemistry of elements such as Li (e.g., Tomascak et al., 1999; Bryant et al., 2003; Liu et al., 2023), K (e.g., Li et al., 2016; Wang and Jacobsen 2016; Hu et al., 2018; Morgan et al., 2018; Moynier et al., 2021; Télouk et al., 2022; An et al., 2023), Rb (e.g., Waight et al., 2002; Nebel et al., 2005; Nebel et al., 2011; Pringle and Moynier 2017; Nie and Dauphas 2019; Wang et al., 2023), Mg (e.g., Galy et al., 2001; Teng et al., 2007; Young et al., 2009; Teng et al., 2010; Bizzarro et al., 2011; Coath et al., 2017), Lu (e.g., Blichert-Toft et al., 1997; Vervoort et al., 2004), V (e.g., Nielsen et al., 2011; Prytulak et al., 2011; Nielsen et al., 2016; Wu et al., 2016), Cu (e.g., Maréchal et al., 1999; Luck et al., 2003; Liu et al., 2014; Wang et al., 2022; Télouk et al., 2023; Luu et al., 2024), B (e.g., Lécuyer et al., 2002; Aggarwal et al., 2003; Foster 2008; Louvat et al., 2011; Chen et al., 2019), Ga (e.g., Yuan et al., 2016; Zhang et al., 2016; Kato et al., 2017), In (Liu et al., 2023), Tl (e.g., Rehkämper and Halliday 1999; Nielsen et al., 2004), and Sb (e.g., Rouxel et al., 2003).

With the high-precision isotopic measurements of state-of-the-art MC-ICP-MS, non-radiogenic isotope variations have been revealed for an increasing number of heavy elements, such as Ti (Millet and Dauphas 2014; Millet et al., 2016; Greber et al., 2017; Deng et al., 2019; Aarons et al., 2020; Deng et al., 2023), Fe (Poitrasson et al., 2004; Williams et al., 2004; Weyer and Ionov 2007; Teng et al., 2008; Sio et al., 2013), Sr (e.g., Fietzke and Eisenhauer 2006; Ohno and Hirata 2007; Moynier et al., 2010; Ma et al., 2013; Shalev et al., 2013), Nd (e.g., Ma et al., 2013; Ohno and Hirata 2013; Saji et al., 2016), and U (e.g., Stirling et al., 2005; Rademacher et al., 2006; Weyer et al., 2008; Brennecka et al., 2010; Hiess et al., 2012; Cheng et al., 2013; Tissot and

Dauphas 2015; Tissot et al., 2016). These findings have revolutionized the field of non-traditional isotope geochemistry (see recent reviews by Johnson et al., 2004; Teng et al., 2017).

There are numerous reviews on various aspects of ICP-MS along with its progressive development (e.g., Jarvis et al., 1992; Montaser 1998; Taylor 2001; Becker 2002; Albarède and Beard 2004; De Groot 2004; Nelms 2005; Becker 2008; Hill 2008; Jakubowski et al., 2011; Vanhaecke and Degryse 2012; Thomas 2013; Olesik 2014; Balcaen et al., 2015; Beauchemin 2020; Van Acker et al., 2023). A critical aspect of ICP analyses is the presence of three essential components in the instrument: sample introduction, excitation, and detection. These components have undergone several major developments in the various types of ICP analyses. The characteristic feature of all ICP analyses is that samples are excited in the plasma to a very high temperature and broken down into their constituent elements. The excited atoms are then separated and detected in a mass spectrometer based on their mass-to-charge ratios. In mass spectrometry, it is convenient to express the mass-to-charge ratio as m/z, which is the ratio between the mass (m) of an ion in daltons and the number (z) of elementary charges (e) it carries. Because most ions produced by Ar ICP carry a single positive charge, the m/z ratio is equivalent to the atomic (or molecular) mass of an ion.

This chapter starts with a brief review of the history of ICP-MS, followed by a comprehensive overview of the fundamental principles and recent developments in ICP-based analytical techniques. The evolution of mass spectrometry for elemental concentration and isotopic ratio analysis is discussed, including developing sample introduction systems, plasma interfaces, mass analyzers, and highly sensitive detection techniques. In addition, novel approaches to overcoming spectral interferences are presented. The discussion covers applications of ICP-MS in cosmochemistry and geochemistry, and extends to future research directions.

2 History of ICP-MS

This section highlights significant milestones in the rich history of ICP. The development of ICP began with the discovery of electric discharge in gases in the 1800s (e.g., Plucker and Hittorf 1865). Langmuir (1928) introduced the term "plasma" to describe the phenomenon of charged particles carried in a neutral gaseous medium by analogy to electrolytes in blood plasma fluids. Since then, it has evolved into a vital tool for breaking apart molecules and exciting the resultant atoms to be analyzed [see the historical account by Ohls and Bogdain (2016)]. Initially, ICP technology was developed to analyze solid samples (arc-spark) but was limited by ionization efficiency and electrode contamination. In the 1940s, researchers developed electrodeless discharges in high-frequency electromagnetic fields operated at atmospheric pressure (Babat 1947), which was the predecessor to modern ICP. The next innovation was the induction plasma torch, capable of sustaining and thermally isolating a stable atmospheric plasma with flowing gas streams inductively heated by a radio-frequency (RF) coil (Reed 1961a; b). Nevertheless, a major obstacle to the application of ICP in analytical chemistry remained: developing an aqueous sample introduction system for ICP-mass spectroscopy and spectrometry.

The application of ICP as an excitation source for atomic emission spectrometry (AES) was pioneered by Greenfield et al. (1964) in the UK and Wendt and Fassel (1965) in the USA, utilizing modified torch designs to introduce aerosols generated from liquid samples (Greenfield et al., 1975; Fassel 1978). The Fassel torch is smaller than the Greenfield torch and has similar analytical performance using lower gas flows and RF power; therefore, it has become widely adopted (Greenfield 2000). Since ICP-AES is based on light emission and does not require a primary light source, it is more convenient for multi-element analyses than atomic absorption spectroscopy

(AAS) and atomic fluorescence spectroscopy (AFS) (Fassel and Kniseley 1974). In addition, ICP is a more effective excitation source than the combustion flame because of its high temperature, allowing for elemental analyses with lower detection limits and greater dynamic ranges. Since its inception, Ar plasma has become the standard ionization source for various ICP-based instruments.

ICP-MS evolved from ICP-OES (optical emission spectroscopy), with both methods sharing similar sample introduction systems but different detector systems. In ICP-OES, the plasma excites atoms to higher energy levels, and as they return to lower discrete energy levels, characteristic optical emissions are measured with an optical spectrometer. The intensity of these emissions is proportional to the concentration. In contrast, in ICP-MS, the plasma breaks apart molecules and produces charged ions, which are separated by electromagnetic fields in a mass spectrometer and detected as electric signals. A significant analytical difference between ICP-OES and ICP-MS is that the former detects the total elemental concentration, whereas the latter detects individual isotopes of each element. Furthermore, the detection limits of ICP-MS are generally several orders of magnitude lower than for ICP-OES (Todolí 2019). Building on the pioneering work of Gray (1974; 1975a; b), who successfully coupled a capillary-arc plasma with a mass spectrometer for direct analyses of aqueous solutions introduced at atmospheric pressure, the first analytical ICP-MS was presented by Houk et al. (1980). The high sensitivity of ICP-MS and its ability to measure individual isotopes have led to the development of various types of mass analyzers for analyzing the constituent masses of a variety of samples.

The magnetic sector ICP-MS and MC-ICP-MS are essential instruments for today's high-precision elemental concentration and isotopic ratio measurements. Their working concepts can be traced back to the end of the 19th century when physicists attempted to measure the m/z ratios of cathode and anode rays within gas discharge tubes, which led to the discovery of electrons,

protons, and isotopes. Thomson (1897) and Wien (1898) independently observed the deflection of cathode rays in an electrostatic field and identified them as streams of negatively charged particles with weight, i.e., electrons. Wien (1898) also observed the deflection of collimated anode rays in a strong magnetic field in the opposite direction to the cathode rays and found that these were positively charged particles with the mass of hydrogen atoms, i.e., protons. Building on these findings, J. J. Thomson designed the archetypal mass spectrograph that deflected ions by parallel magnetic and electric fields and imaged their parabolic trajectories on a photographic plate. Using this parabola spectrograph, Thomson (1913) provided the first proof of stable isotopes (^{20}Ne and ^{22}Ne). This discovery motivated ongoing efforts to determine the exact atomic masses of elements and to develop improved analytical instruments for quantitative isotopic analyses, paving the way for the development of modern MC-ICP-MS.

MC-ICP-MS was invented to overcome the limitations of high-precision isotopic analyses using existing mass spectrometry techniques. Substituting the thermal ionization source (< 2800 K) with a more energetic ICP source (5000-10,000 K) substantially improves the ionization efficiency for elements with high first ionization energies (Fig. 1). Also, instrumental isotope fractionation is relatively stable during MC-ICP-MS analysis. Source instability, which is the primary limiting factor for high-precision isotopic measurements with ICP instruments, is overcome by using a magnetic sector to spatially separate ion beams according to their m/z ratios and direct them into a set of designated collectors. This capability of simultaneous analyses of multiple isotopes over a narrow mass range is the primary purpose of MC-ICP-MS, which contrasts with traditional ICP-MS techniques that focus on multi-element analyses by sequentially detecting individual ion beams rapidly scanned across a wide mass range. The original MC-ICP-MS, known as the Plasma 54, was a hybrid between the VG PlasmaTrace magnetic sector ICP-

MS and the Sector 54 TIMS. Analyses of U and Pb isotopic ratios with this instrument yielded accuracy and precision similar to those obtained using TIMS (Walder and Freedman 1992). Since then, MC-ICP-MS instruments have been advancing rapidly to achieve unprecedented precision, and ICP-MS has become a leading technique for elemental and isotopic analyses.

3 Primary components of ICP-MS

ICP-MS has undergone significant development in its primary components, leading to the current state-of-the-art systems. These components are as follows (Fig. 2):

(1) a sample introduction system that brings a solution or solid sample to the ICP to break it down into ionizable atoms

(2) an ion source that forms ions and accelerates the positively charged particles

(3) an interface that samples ions formed at atmospheric pressure into the vacuum of the mass spectrometer

(4) a mass analyzer that sorts ions by their m/z ratios

(5) an ion detection system that produces electrical signals

3.1 Sample introduction

ICP-based analyses produce free atoms that can be readily excited and ionized by the plasma. Initially, samples must be effectively introduced to the plasma. Solution nebulization is most commonly used, where a liquid sample is converted into a fine aerosol using a nebulizer (from Latin *nebula*, meaning "mist"). In contrast, laser ablation is used for *in situ* analysis of solid samples, as discussed in another chapter of this volume. This chapter mainly concerns the solution nebulization method that delivers a fine aerosol to the plasma. Since only a few percent of an

aspirated sample eventually reaches the plasma (Gray 1975), efficient and consistent sample introduction is critical for reproducible signal output and the stable operation of the plasma.

3.1.1 Nebulization

Most ICP-based analyses use a pneumatic nebulizer that passes a high-speed gas through a converging nozzle to break liquids into aerosols (e.g., Sharp 1988; Todoli and Mermet 2011). Liquid samples are aspirated by a sampling probe connected to a fine capillary in the center of the nebulizer. The nebulizer is typically fed with a stream of compressed argon gas that accelerates to sonic velocity when it emerges from the nebulizer nozzle, providing the mechanical force to disperse the liquid and form an aerosol. The gas is commonly supplied in the outer capillary concentric to the central sample capillary (concentric nebulizer, Fig. 3A) (e.g., Meinhard 1976; Meinhard 1979) or at a right angle to the sample capillary by a second gas capillary (cross-flow nebulizer, Fig. 3B) (e.g., Valente and Schrenk 1970; Kniseley et al., 1974). Concentric nebulizers have fine-bore capillaries that facilitate the kinetic energy transfer between gas and liquid. They create a fine aerosol within a narrow size range, offering superior sensitivity and stability for routine analyses of clean solutions. In comparison, cross-flow nebulizers allow wider liquid capillaries and are preferred for samples containing undissolved particles or high levels of heavy element matrices. Parallel path nebulizers are also used for samples with larger particles and high salt contents, whereby a liquid sample is pumped parallel to the nebulizer gas stream, thereby being entrained into the gas flow and forming an aerosol.

The development of low-flow nebulizers has facilitated effective ionization using a significantly reduced sample volume (Olesik et al., 1994; Vanhaecke et al., 1996; Boulyga and Becker 2001; Todolí and Mermet 2006). For instance, a 50-μL/min nebulizer with 50% efficiency consumes 20-40 times less sample than a standard flow nebulizer (1-2 mL/min) with $\leqslant$ 5%

efficiency, while sensitivity is only reduced by a factor of ⩽ 2 (Fig. 3C). The increased efficiency of sample transport and fragmentation is likely due to increased kinetic energy to liquid ratio and decreased droplet coalescence at reduced sample uptake rates (Meinhard 1979; Todoli and Mermet 2011; Olesik et al., 2021). These micro-nebulizers enable the analysis of samples of limited size and contribute to a more robust plasma by reducing solvent loading to the plasma and preventing the formation of solvent-related interferences.

Nebulization can proceed with or without external pumping, depending on the nebulizer and ICP-MS system in use. While self-aspiration occurs due to the pressure drop created as argon flows through the nebulizer nozzle and is accelerated (Venturi effect), a peristaltic pump is recommended for elemental analyses in ICP-MS to ensure a constant, regulated sample flow and to minimize the impact of sample viscosity on the uptake rate. In contrast, isotopic ratio analyses in MC-ICP-MS usually do not require a peristaltic pump for sample uptake, as the elements of interest are analyzed in dilute concentrations with little differences in viscosity. This direct sample uptake without a peristaltic pump shortens the sample path to the nebulizer and reduces sample consumption. In addition, sample contamination is minimized as interactions with the pump tubing are avoided, which is beneficial for isotope analysis. However, if no peristaltic pump is used, keeping the liquid surfaces of the sample and standard solutions at the same height is crucial to avoiding differential uptake rates between analyses.

3.1.2 Conventional sample introduction systems

Depending on analytical needs, the nebulizer is fitted onto a spray chamber (Fig. 4), a desolvation device (Fig. 5), or it can be mounted directly on the torch, corresponding to three types of sample introduction systems: "wet" plasma introduction, "dry" plasma introduction, and direct injection nebulization (DIN). "Wet" plasma introduction is the simplest and most compact, using

a spray chamber to filter large droplets. This sample introduction typically provides the best stability and precision and is preferred when there is sufficient sample. In comparison, "dry" plasma introduction uses a semi-permeable heated Teflon® membrane to remove most of the solvent, thereby offering substantially higher sensitivity than the "wet" plasma introduction (Fig. 6). It is preferred when the analyte is limited or if solvent-related spectral interferences occur. Finally, the less common DIN requires a specially designed nebulizer and generally provides sensitivity between "wet" and "dry" plasma introduction (Fig. 6).

3.1.2.1 "Wet" plasma introduction using a spray chamber

The aerosols formed by a pneumatic nebulizer have a range of diameters, and only those smaller than ~10 μm can be efficiently ionized by the plasma (e.g., Olesik 2014). This size limit occurs because the evaporation rate of solvent in a droplet increases with its surface area to volume ratio. Larger droplets that are not entirely vaporized upon entering the plasma can significantly cool the plasma or even cause it to extinguish. The stability of the plasma can be improved by using a spray chamber to condense larger aerosol particles; however, this also removes about 95% of the liquid sample taken up by the nebulizer.

The two most common designs of spray chambers are the cyclonic type and the Scott type; both can have baffles that serve as a secondary droplet size separator to further reduce aerosol size distribution (Fig. 4). When passing through a spray chamber, the fine aerosol travels in the streamline of the carrier gas. In contrast, the larger droplets, due to their greater size and momentum, impinge on the spray chamber wall or the baffle and form a condensate, which is pumped out to the waste. A cyclonic spray chamber separates larger liquid droplets by centrifugal force during the angular flow of the sample aerosols. In comparison, a double-pass Scott-type spray chamber selectively funnels the small droplets into a central tube, whereas the larger droplets

will condense and divert to the drain. Spray chambers are typically cooled thermoelectrically (Peltier cell) to minimize water vapor entering the plasma and forming associated oxides. The cooling device also stabilizes the spray chamber temperature, thereby reducing temperature-related signal drift.

Both nebulizers and spray chambers can be manufactured from glass, quartz, or Teflon®, depending on their intended use. Quartz nebulizers and spray chambers have the longest lifespan and are recommended for clean samples with low salt contents. On the other hand, Teflon® nebulizers and spray chambers resist hydrofluoric acid (HF) but are more expensive and softer than quartz ones.

3.1.2.2 "Dry" plasma introduction using desolvation membrane

In contrast to "wet" plasma introduction, where solvent vapors condense on the cooled spray chamber walls, desolvation can be enhanced by heating the spray chamber with a downstream mechanism to remove solvent vapors (e.g., a membrane desolvator or cold condenser). In a typical desolvation nebulizer system, the sample aerosol is transported into a heated, semi-permeable Teflon® membrane, through which solvent vapors can pass freely and be removed by an external gas flow (Fig. 5). The desolvated sample contained in the membrane is carried into the plasma. Inlet gas is preheated and directed at the chamber walls to prevent condensation of sample aerosols. For applications unaffected by nitrogen-based interferences, a small amount of N_2 can be blended into argon to enhance sensitivity and reduce oxide formation (see Section “Mixed-gas plasma”).

Several desolvation nebulizer systems are commercially available (Fig. 5). The DSN-100 from Nu Instruments is the only one that works with glass instead of Teflon® nebulizers, but its production has been discontinued. Teledyne CETAC produces the Aridus series (Aridus, Aridus II, and Aridus 3), with the Aridus 3 featuring software control of gas flow and temperature.

Elemental Scientific Inc. (ESI) offers a selection of systems for specific applications, such as Apex Q (Quartz flow path), Apex IR (for Isotope Ratio analysis), and Apex HF (for samples containing HF). The latest software-controlled Apex Omega combines a heated cyclonic spray chamber, a multi-pass Peltier-cooled condenser, and a heated membrane desolvator to achieve multi-stage solvent vapor removal. This system improves sample introduction efficiency and sensitivity, which is particularly useful for samples that contain high levels of dissolved solids or that are difficult to analyze by conventional nebulization methods.

3.1.2.3 Direct injection nebulizer (DIN)

Some elements (e.g., B, Hg, Mo, Si, Sn, W, Zn, and Zr) tend to be absorbed in the introduction system and released during subsequent runs, causing memory effects and inaccurate analyses. To alleviate this carry-over effect, DIN has been developed, whereby a micro-concentric nebulizer is mounted at the base of the plasma torch so that the aerosol sprays directly into the plasma without passing through and contacting a spray chamber. This design not only reduces memory effects but also achieves ~ 100% sample transport efficiency to the plasma, which is a significant improvement over the 1 - 2% efficiency of conventional nebulizer-spray chamber arrangements (Browner and Boorn 1984). The DIN was first used in single-collector ICP-MS and ICP-AES for elemental analyses (LaFreniere et al., 1985; LaFreniere et al., 1987), and it has later been employed for isotopic measurements using MC-ICP-MS (e.g., B, Smith et al., 1991; Louvat et al., 2011).

3.1.3 Sample introduction accessory: Hydride generation system

Hydride generation (HG) is an effective technique for introducing As, Bi, Ge, Pb, Sb, Se, Sn, Te, and Hg (e.g., Thompson et al., 1978a; b; Godden and Thomerson 1980; Date and Gray 1983; Powell et al., 1986; Wang et al., 1988; Dean et al., 1990). These elements are difficult to detect using conventional nebulization due to their low natural abundances, high first ionization energies

(Fig. 1), and widespread matrix- or solvent-related interferences. In an HG system, the liquid sample is introduced using a peristaltic pump and mixed online with a strong acid (e.g., HCl or HNO_3). Further down-line, the acidified sample is mixed with a reducing agent (e.g., $NaBH_4$ stabilized with NaOH), converting the analyte elements to volatile species that evolve from the bulk liquid and are entrained by the argon stream into the torch. A spray chamber is often used as a gas-liquid separator to improve plasma stability and detection limits, and to allow the simultaneous detection of non-hydride forming elements (e.g., Huang et al., 1987; Huang et al., 1988; Heitkemper and Caruso 1990; Zhang and Combs 1996).

This technique offers two advantages over standard nebulization. First, the generation and transport of volatile analytes can approach 100% efficiency, which increases sensitivity by two orders of magnitude. Second, most matrix effects and spectral interferences (e.g., $^{40}Ar^{35}Cl^{+}$ on $^{75}As^{+}$) are eliminated prior to detection by separating the volatile analytes from the bulk liquid containing sample matrices, solvents, and reaction solutions. The coupling of HG with MC-ICP-MS is particularly beneficial to isotopic analyses, as the HG settings can be optimized for a single element. High-precision isotopic analyses have been achieved for Se (e.g., Rouxel et al., 2002; Ellis et al., 2003; Kurzawa et al., 2017; Stüeken 2017), Te (e.g., Brennecka et al., 2017; Wasserman and Johnson 2020), Ge (e.g., Escoube et al., 2012; Karasiński et al., 2021), and Hg (e.g., Geng et al., 2018; Moynier et al., 2020) using as little as nanograms of samples.

3.2 The ICP discharge

Sample aerosols are carried by gas flowing into the ICP torch that sustains the plasma. The torch typically comprises three concentric quartz tubes (Fig. 7), which withstand the significant temperature gradient toward the plasma owing to the low thermal expansion coefficient and thermal conductivity of quartz (e.g., Reed 1961; Greenfield et al., 1964; Fassel and Kniseley 1974).

A fast stream of *cooling gas* (12-18 L/min) and a slower stream of *auxiliary gas* (~ 1 L/min) spiral around the outer and middle tube, respectively, which sustain the plasma, centering and constricting it radially to prevent the torch from melting. These vortex gas flows create a low-pressure central channel for sample injection by the *nebulizer gas* (~ 1 L/min). The three tubes are usually assembled as one piece. Alternatively, the sample injector can be a demountable piece for applications requiring a specific bore size, configuration, or more corrosive-resistant materials (e.g., sapphire, alumina, platinum, and ceramic).

Argon is considered the most practical gas for generating and sustaining an ICP at atmospheric pressure for the following reasons. First, argon is chemically inert because it has a completely filled valence shell that stabilizes its electronic configuration without bonding to other atoms. Second, a monatomic gas like argon can only store heat as translational kinetic energy, unlike diatomic gases (e.g., N_2 and O_2), which may also store energy through rotation and vibration at ionization temperatures. Hence, argon absorbs less heat per degree of temperature rise than diatomic gases. Third, argon is the most abundant among the noble gases. It is heavier than air and accumulates in the atmosphere. Therefore, it is less expensive to purify in bulk than neon and helium. Last, the lower ionization energy of argon relative to neon and helium requires a less powerful system to sustain an Ar plasma (Fig. 1A).

Argon ICP is a weakly-ionized plasma (~ 0.1%, Niu and Houk 1996) sustained by converting the electrical energy from an RF generator into gas enthalpy via inductive heating (Fig. 7). Coupling is achieved by sending an oscillating RF signal (typically 0.5-1.5 kW at 27.12 or 40.68 MHz) through a copper coil (2-3 turns) encircling the torch exit, which induces a poloidal electromagnetic field oscillating at the same frequency (e.g., Todolí 2019). When the gas in the coil space is seeded with electrons, conventionally by a high-voltage spark from a Tesla coil, some

406 gas atoms are ionized on collisions. The charged particles are accelerated by the RF magnetic field
407 and set to move in closed circular paths, leading to a cascade propagation of collisional ionizations
408 almost instantaneously and heating of the plasma once initiated.

409 Toroidal plasma is a robust source for excitation and ionization. Critically, sample aerosols are
410 able to retain their compositional integrity due to limited mixing with the annular plasma. Sample
411 aerosols are injected through the central channel of the plasma, traveling an extended time (1-2
412 ms) in the flame-like plasma with minimal disturbance to the induction region. Plasma
413 temperatures can reach 8000 to 10000 K in the induction zone and are slightly lower (5000-7000
414 K) in the plasma tail (analytical zone). The high temperature evaporates aqueous solvents from the
415 analyte salt, breaking down constituent ionic bonds and converting the gaseous atoms into positive
416 ions. Ionization occurs via several pathways. Thermal ionization occurs during collisional energy
417 transfer between atoms, ions, and electrons (e.g., $Ar + e^- \rightarrow Ar^+ + 2e^-$). Penning ionization occurs
418 when ground-state atoms interact with metastable Ar species ($Ar^m + M \rightarrow Ar + M^+ + e^-$). Charge
419 transfer occurs when electrons are transferred between ions and atoms ($Ar^+ + M \rightarrow Ar + M^+$).

420 Argon ICP primarily produces singly charged ions because argon has a first ionization energy
421 (15.8 eV) that lies between the first and second ionization energies of most elements (Fig. 1A).
422 According to Houk (1986), elements with first ionization energies lower than 8 eV achieve over
423 90% ionization, and alkali and alkaline earth elements are the easiest to ionize. Furthermore, the
424 alkaline earth elements and rare earth elements (REEs) have sufficiently low second ionization
425 energies that doubly charged ions may occur (e.g., Ca^{2+}, Sr^{2+}, and Ba^{2+}) (Fig. 1B). Non-metals,
426 metalloids, and certain metals have lower ionization efficiencies. Elements with first ionization
427 energies of 8-9 eV (B, Si, Pd, Cd, Os, Ir, and Pt) reach 93-58% ionization, of 9-10 eV (Be, Zn, As,

Se, Te, and Au) reach 75-33% ionization, and of 10-11 eV (P, S, I, and Hg) reach 38-14% ionization, respectively. Only a few percent are ionized for elements such as Br and Xe.

3.3 The ICP-MS interface

The interface region extracts ions formed in the ICP (~ 1000 mbar) into a differentially pumped vacuum system (10^{-5} to 10^{-10} mbar) in which the mass spectrometer is contained (Fig. 8A). An atmospheric-pressure ion source offers the flexibility of switching between different introduction systems and using alternative gases to adapt to specific application needs. By contrast, mass spectrometers operate under high vacuum, allowing the sampled ions to reach the detectors with minimal reaction, neutralization, scattering, or fragmentation due to collisions with other ions or gas molecules. A well-maintained vacuum is vital for accurate and precise measurements. It minimizes spectral interferences from air, water, gas molecules, or other contaminants. It also improves peak shape by reducing ion scattering and background noise, and prevents arcing in the high electric potential field. The substantial pressure and temperature gradients across the interface present a fundamental challenge for its design, and high ion transmission into the mass spectrometer has to be achieved without compromising its high vacuum.

The concept of mass spectrometric sampling of plasma ions stems from the use of supersonic free jets to form molecular beams. This concept was established by the theoretical work of Owen and Thornhill (1948) and Kantrowitz and Grey (1951) and was experimentally demonstrated by Johnson (1927; 1928), Kistiakowsky and Slichter (1951), and Becker and Bier (1954). By admitting gas into a low-pressure chamber through a small nozzle, the emerging stream undergoes a near-adiabatic, enthalpy-driven expansion. During this expansion, a substantial portion of the random thermal motion upstream of the nozzle is converted into an ordered motion with a narrow velocity distribution, forming a high-intensity, directed, and nearly collisionless beam. This nozzle

451 expansion is accompanied by rapid rarefaction and cooling of the admitted gas stream; therefore,
452 it is an ideal mechanism for interfacing a continuum gas flow from the high-temperature,
453 atmospheric ICP source with a mass spectrometer kept under vacuum.

454 Following the practice of sampling flames (Hayhurst et al., 1971), a conical metal duct ("cone")
455 with a circular orifice in its tip is typically used for plasma extraction. It allows the plasma gas to
456 sweep smoothly over its surface with little disturbance from the back pressure, and the central flow
457 passing through the tip to expand freely inside the cone into the first vacuum stage of the
458 instrument. The cone is supported on a grounded, water-cooled mount to prevent melting by the
459 plasma. When the plasma impinges on the cone, a boundary layer of cool gas forms over the cone
460 (Hayhurst and Kittelson 1977), where unwanted chemical and physical interactions may occur to
461 alter the relative populations of the plasma constituents. In addition, a thin electron-poor sheath
462 may develop around the sampling orifice as electrons have a smaller mass and greater velocity
463 than cations and, therefore, have a higher frequency of striking the cone to be neutralized (e.g.,
464 Chambers et al., 1991; Niu and Houk 1996). It is essential to prevent significant charge separation
465 during ion sampling and to ensure the integrity of the sampled plasma.

466 The diameter of the sampling orifice is a limiting factor for a representative ion sampling. The
467 orifice should be sufficiently large so that a fraction of the bulk plasma can flow through it in an
468 ordered motion as a continuum. The flow regime is determined by the Knudsen number (K_n),
469 which is the ratio of the mean free path (λ) of the plasma gas at the throat of the sampling orifice
470 to its diameter (D_0). Continuum flow occurs if $K_n < 0.01$, which means that D_0 should be at least
471 100λ wide. The mean free path ($\lambda = 1/n\sigma$) of a conventional Ar ICP is less than 2×10^{-3} mm,
472 assuming a number density of the gas $n = 1.5 \times 10^{-18}/cm^3$ and an Ar collision cross section $\sigma = 5$
473 $\times 10^{-15}$ cm^2 (Douglas and Tanner 1998). The sampling diameter also needs to be substantially

474 larger than the Debye length of the ICP (λ_D), estimated to be 10^{-3} to 10^{-4} mm (Douglas and Tanner
475 1998), to shield the charged plasma species from external fields and avoid significant charge
476 separation. Given these considerations, an orifice wider than 0.2 mm is preferable (Date and Gray
477 1983; Gray and Date 1983).

478 Early efforts to extract ions from the plasma relied on a high-capacity pump to maintain a low
479 background pressure ($< 10^{-3}$ Torr) in the first vacuum stage (e.g., Gray 1975a; b; Houk et al., 1980),
480 similar to the Fenn-type expansion used in molecular beam studies (Fenn 2000). Nevertheless, the
481 size of the sampling orifice used in these earlier studies (0.050-0.125 mm) was limited by the mass
482 throughput the oil diffusion pumps could handle and the frequent occurrence of secondary
483 discharge when the sampler orifice exceeded 0.1 mm (e.g., Gray and Date 1981; Houk et al., 1981).
484 Due to the weaker suction of a smaller orifice, the sampled gas has to traverse a thicker boundary
485 layer (Hayhurst and Kittelson 1977). This boundary layer sampling was prone to orifice clogging,
486 undesirable oxide formation, and ion-molecule reactions (e.g., Date and Gray 1983a; b).

487 To overcome the practical limitations of boundary layer sampling, an alternative sampler-
488 skimmer interface has been developed for continuum sampling from the bulk plasma (Douglas and
489 French 1981; Date and Gray 1983; Douglas et al., 1983). This sampling arrangement utilizes the
490 Campargue-type expansion (Campargue 1964; 1984), by which the atmospheric plasma gas
491 propagates supersonically into a relatively high background pressure (a few Torr), forming a
492 concentric barrel shock that terminates at a perpendicular shock wave (i.e., the Mach disk) (Fig.
493 8B). The core of the supersonic expansion is effectively shielded from the background gas by the
494 shock-wave structure (i.e., zone of silence), and the center-line flow is skimmed into the second
495 vacuum stage at a much lower pressure (10^{-3} to 10^{-4} Torr). A mechanical pump is sufficient for
496 evacuating the region between the sampler and skimmer cones. The relatively high background

pressure in this region permits the use of a larger orifice (~ 0.41 to 1 mm diameter) to sample the bulk plasma with an increased ion flux, which improves the detection limits and dynamic range of the ICP-MS while reducing oxide formation and salt deposition at the orifice (Douglas and Houk 1985). The impedance matching network and tank circuit were modified accordingly to prevent the occurrence of secondary discharges (Douglas and French 1986). This improved interface design eventually led to the introduction of the first commercial ICP-MS by PerkinElmer-SCIEX in 1983.

A typical interface of modern ICP-MS is shown in Fig. 8B), and the gas dynamics of the interface is detailed by Douglas and French (1988). For sampling an Ar ICP with a gas kinetic temperature of 6000 K, as the plasma is drawn adiabatically through the sampling orifice (diameter $D_0 \sim 1$ mm), the axial flow accelerates to local speed of sound ($a_0 = (\gamma k T_0/m)^{0.5} = 1.4 \times 10^5$ cm/s) at a distance of $x = 0.5D_0$ downstream of the sampler, and reaches terminal speed ($u = (5kT_0/m)^{0.5} = 2.5 \times 10^5$ cm/s) at $x \geq 2D_0$. Assuming the plasma expands from atmospheric pressure (P_0) into a background pressure (P_1) of ~ 2 Torr, the shock wave terminates at the Mach disk located at $x_m = 0.67D_0(P_0/P_1)0.5 = 13$ mm. The skimmer is typically placed before the Mach disk at ~ $2/3x_m$ to allow high ion transmission while minimizing background gas penetration into the supersonic jet, corresponding to a sampler-skimmer spacing of 7-8 mm and a travel time of about 3 μs. This short transit time limits the occurrence of ion-molecule chemistry. In addition, while electron density decreases with $1/x^2$, resulting in an increase in λ_D from ~ 10^{-4} mm at the sampler to 10^{-3}-10^{-2} mm at the skimmer tip, λ_D remains much smaller than a typical skimmer orifice (0.4-0.8 mm diameter). Therefore, the ion population sampled through the sampler and skimmer resembles that in the plasma source.

519 Downstream of the skimmer orifice, the electron density continues to decrease to the extent
520 that λ_D becomes significant for charge separation (Niu and Houk 1994). With their high mobility,
521 electrons diffuse readily to the inner wall of the skimmer cone where an electron sheath forms.
522 The initially quasi-neutral beam takes on a positive net charge and expands radially (defocuses)
523 due to coulomb repulsion. The heavier ions, which have greater momentums, are repelled less than
524 the lighter ions and are transmitted preferentially. Thus, analyte transmission efficiency is affected
525 by the concentration and atomic mass of the constituent elements, and the isotopic composition
526 measured for a given element is likely to be heavier than the true isotope ratio. This mass
527 discrimination due to space charge accounts for many aspects of the matrix effects (e.g., Gillson
528 et al., 1988; Tanner 1992) and must be corrected appropriately (see Section "Instrumental isotope
529 fractionation"). To mitigate space charge and matrix effects, a triple-cone interface has been
530 developed, which produces a less dispersed ion beam with a reduced ion current flux through the
531 interface orifices (Tanner et al., 1994a; b).
532 Ions emerging from the interface have divergent trajectories along the slope of the skimmer
533 cone due to space charge effects and the variable ion kinetic energies acquired during the
534 expansion-driven acceleration. The Ar flow and entrained ionized species accelerate to a similar
535 velocity of ~ 2500 m/s, resulting in a mass-dependent spread in ion kinetic energy from 0.5 to 10
536 eV for a mass range from Li to U. The ion kinetic energies may be increased by an additional
537 voltage offset of 10 to 20 eV between the plasma and the sampler cone due to capacitive coupling
538 between the induction coil and the plasma (Douglas and French 1986). This wide dispersion of ion
539 kinetic energy creates problems for ion focusing and reduces the achievable mass resolution of a
540 mass analyzer. These detrimental effects can be reduced by accelerating the positive ions to a
541 suitable velocity to travel toward the detection system. A high acceleration voltage (typically 4000-

10,000 V) is applied in magnetic sector-ICP-MS to dilute the initial ion kinetic energy spread, whereas a smaller acceleration voltage (~ 300 V) is used in quadrupole-ICP-MS to allow ions to pass sufficient RF cycles for mass selection.

The sampler and skimmer cones are commonly made from nickel, a durable metal suitable for most samples, while platinum cones are preferred for more corrosive samples or rinsing solutions. The geometry of the cone has a crucial impact on ion transmission, space charge effects, and the introduction of sample matrices into the mass spectrometer. Notably, "wet" and "dry" sample introduction systems are paired with separate sets of cones, which vary by manufacturer and can be tailored to specific analytical requirements. For example, a Jet sampler cone with a slightly wider orifice and an X-skimmer cone with a trumpet-shaped entrance can be used for the Neptune Plus MC-ICP-MS to increase sensitivity by 5-10 times (e.g., Newman 2012; He et al., 2016).

3.4 Ion optics

The ion beam leaves the interface with a defocused circular profile. It then passes through an ion-focusing system to be reshaped into a narrow rectangular profile while being directed toward the detectors. This focusing system consists of a series of metal slits, plates, barrels, and cylinders. By varying the polarity and strength of applied voltages, the ion trajectory and the degree of focusing can be adjusted. A circular or conical extraction lens is placed after the skimmer cone to extract positive ions while rejecting electrons, neutral atoms, and molecules as much as possible. This lens significantly improves the tranmission efficiency of low-mass elements that are displaced further away from the centerline of the ion beam by the heavier elements. Succeeding lenses adjust the ion beam in vertical and horizontal directions, refining its focus, alignment, and trajectory. Focusing the ion beam precisely through these lenses reduces ion loss and increases analytical sensitivity.

For instruments that employ a multi-collector block with fixed physical spacing, additional zoom lenses are placed between the magnet and the collector block to adjust the mass dispersion between ion beams, thereby directing them into designated collectors. As an illustration, Nu instruments use a magnet with an effective radius of ~ 500 mm. It has a dispersion for Nd isotopes of 3.4 mm per amu, which is set to be the fixed spacing between adjacent collectors. This spacing is wider than the dispersion between adjacent isotopes of elements heavier than Nd (e.g., U), and a negative quadratic voltage is applied to magnify the ion beam image at the collectors (Fig. 9A). For lighter elements such as Sr, the magnet leads to a dispersion of ~ 5.8 mm between its isotopes (Fig. 9B). While applying a positive quadratic voltage can demagnify the ion beam image into adjacent collectors, this may lead to significant distortions. Alternatively, the dispersion is widened to 6.8 mm by applying a negative quadratic voltage so that different Sr isotopes can be directed into every other collector with appropriate peak shapes (Fig. 9C).

3.5 Mass analyzer

The mass analyzer is the central component of an ICP-MS; it uses magnetic and electric fields to separate ions based on their m/z ratios. Ions with different m/z ratios are separated according to their kinetic energies, momentums, and velocities. These properties form the basis for designing various mass analyzers, with magnetic sector, quadrupole mass filter, and time-of-flight (TOF) analyzers being the most prevalent in ICP-MS. They use different mass separation mechanisms, which lead to their characteristic resolution and detection capabilities.

3.5.1 Critical characteristics of mass analyzers

3.5.1.1 Mass resolution

The resolution of a mass spectrometer defines its ability to distinguish ions with small mass differences. Resolution is typically quantified by the ratio of the mass being analyzed (m) to the

588 smallest increment in mass (Δm), i.e., m/Δm, and can be described in three ways (Fig. 10). The
589 10% valley definition applies to two adjacent peaks of equal height, which are considered
590 resolvable if the valley between them is no more than 10% of their height. In this definition, the
591 smallest resolvable mass difference is determined by the widths of the ion beam and the collector
592 slit. The second definition is quantified by the width of a single ion peak at a given fraction (e.g.,
593 50%, 5%, or 0.5%) of its maximum peak height. The 5% peak width definition is equivalent to the
594 10% valley definition. The third definition is based on the peak edge resolving power, which
595 measures how well the ion beam is defined at the source slit. This is calculated from the mass
596 difference at 5% and 95% of the maximum height on the leading edge of the peak, and it may
597 exceed the peak width resolution and the 10% valley resolution. A steeper peak corresponds to a
598 narrower beam and a higher resolving power.

599 **3.5.1.2 Mass dispersion**

600 The mass dispersion (D) of a magnetic sector mass spectrometer refers to the physical distance
601 between adjacent masses. This property is determined by its geometric configuration. For two
602 peaks at masses m and (m + Δm), the physical distance between the two (X) is related to D by the
603 following equation:

604 $$\frac{D}{X} = \frac{m}{\Delta m}$$

605 For peaks at adjacent masses (ΔM = 1 amu), X corresponds to the physical separation between
606 two adjacent masses, which decreases as the analyte mass increases.

607 **3.5.1.3 Abundance sensitivity**

608 Abundance sensitivity refers to the tailing of a peak at mass m into its neighboring masses at
609 m±1. Tailing arises primarily from collisions of high-velocity ions with background gas molecules

along the flight path. If collisions occur before the magnet, ions affected by the collisions will have a reduced kinetic energy and be deflected more in the magnetic field than those with the same m/z ratios but unaffected by the collisions. The more deflected lower-energy ions may enter the collector below the correct mass. Since ions most likely lose energy during collisions, this tailing effect is largely absent on the high-mass side of the peak, resulting in asymmetric tailing. Alternatively, if collisions occur after the magnet, a small percentage of ions will be diverted into the lower and higher mass collectors with equal possibility, resulting in symmetric tailing on both sides of the peak. The effect of tailing is particularly significant when a low-intensity peak is adjacent to peaks of much higher intensities.

3.5.2 Motion of charged particles in electric and magnetic fields

The Lorentz force describes the combined effect of electric and magnetic forces exerted on a charged particle and varies in proportion to its electric charge:

$$F = q(E + v \times B)$$

where F stands for the force applied to the ion, q for the electric charge (q = ze), E for the electric field, and $v \times B$ for the cross product of the ion's velocity and the magnetic flux density.

The force accelerates an ion inversely proportional to its mass, according to Newton's second law:

$$F = ma$$

where m stands for the mass of the ion and a for the acceleration.

Therefore, ions in a mass spectrometer are separated by their m/z ratios. The electric force accelerates an ion in the direction of the applied electric field, and a radial electric field deflects incoming ions according to their velocity and kinetic energy. The magnetic force does not change

the speed and kinetic energy of a moving ion but deflects it along a circular path in the plane of $v \times B$ according to its momentum and charge.

3.5.2.1 Acceleration between parallel plates

In the magnetic sector ICP-MS, ions are accelerated to reach a high velocity and kinetic energy before entering the magnet, such that their mass separation in the magnetic field is less affected by their initial kinetic energy spread, and sensitivity is improved. Assuming that an ion starts to accelerate from rest and move along the electric field across a potential difference of $\boldsymbol{U}$ (acceleration voltage), the change in potential energy is converted into its kinetic energy:

$$qU = \frac{1}{2}mv^2$$

This acceleration gives the ion a velocity of:

$$v = \sqrt{\frac{2qU}{m}}$$

At an acceleration voltage of 6-10 kV, as commonly used in MC-ICP-MS, a proton with a mass of 1.67×10^{-27} kg and a charge of 1.6×10^{-19} coulombs will reach a velocity of ~1000 to 1400 km/s after the acceleration.

3.5.2.2 Deflection between cylindrical capacitors

An electric field between two cylindrical plates exerts a radial force that pulls ions toward its center. The voltage is set such that the electric force equals the centripetal force to steer a moving ion along the curve of the electrode plates with a radius of r_E:

$$qE = \frac{mv^2}{r_E}$$

The radius of ion paths is determined by the kinetic energies (E_K) of ions and the potential field (E) between the plates:

$$r_E = \frac{mv^2}{qE} = \frac{2 \times \left(\frac{1}{2}mv^2\right)}{qE} = \frac{2E_K}{qE}$$

Ion beams with the same kinetic energy will be brought to a focus despite their divergent velocity vectors at entry, achieving energy focusing (Fig. 11). In contrast, ions with slightly different kinetic energies will be deflected to various degrees. By placing a narrow collimating slit at either end of the electric sector, only ions that fall within the selected kinetic energy range will pass through.

3.5.2.3 Deflection in a static magnetic field

A magnetic sector focuses ions with equal momentum and deflects ions with different m/z ratios. When incoming ions enter a magnetic field with velocities perpendicular to the plane of v × B, they will be forced onto circular paths (Fig. 12A), and the magnetic force equals the centripetal force:

$$F_B = qvB = \frac{mv^2}{r_B}$$

The radius of the circular path r_B is given by:

$$r_B = \frac{mv}{qB} = \frac{\sqrt{2mE_K}}{qB}$$

According to the equation above, singly charged ions with equal momentum will travel in circles with the same radius (r). If they enter the magnetic field from a common point with a divergence in the direction of α, their circular paths will intersect after traveling approximately a semicircle (Fig. 12B). With small-angle approximation, a monoenergetic ion beam with an angular divergence of 2α will converge to a limited width of b at the exit slit:

672 $$b \approx 2r(1-cos\alpha) \approx r\alpha^2$$

673 Furthermore, ions with identical kinetic energy will be deflected according to their masses,
674 whereby ions with smaller masses will be deflected more than those with higher masses. The
675 physical dispersion (D) of two masses, m and (m+Δm), along the focal plane is twice the difference
676 in the radii (Δr_B) of their circular paths through the 180° magnet (Fig. 12C). Given that

677 $$r_B = \sqrt{\frac{2U}{qB^2}}\sqrt{m}$$

678 thus

679 $$\Delta r_B = r_B \frac{\Delta m}{2m}$$

680 and

681 $$D = 2\Delta r_B = \frac{\Delta m}{m} r_B$$

682 The natural mass dispersion of a given magnetic sector thus depends on its effective radius.

683 The equation for r_B can be rearranged as below:

684 $$\frac{m}{z} = \frac{B^2 r_B^2 e}{2U}$$

685 This equation demonstrates that for singly charged ions, the radius of ion trajectory is
686 positively correlated with mass under a constant magnetic field and acceleration voltage. In single-
687 collector ICP-MS, ions with different masses can be sequentially focused onto the detector by
688 adjusting the magnetic field strength, the acceleration voltage, or a combination of both. This
689 allows for a complete scan of m/z ratios from low mass to high mass. However, magnet scanning
690 is slower than acceleration voltage scanning as a settling period of ~10-200 ms is required for each
691 scan to ensure a stable magnetic field. In comparison, MC-ICP-MS analyses are typically

692 performed in static mode, with both the acceleration voltage and the magnetic flux density held
693 constant, while ions with different masses are collected along a focal plane for simultaneous
694 detection.

695 **3.5.2.4 Deflection in perpendicular electric and magnetic fields**

696 If an ion enters crossed electric (*E*) and magnetic (*B*) fields with the velocity *v* perpendicular
697 to the lines of force of both fields, the ion will be deflected unless the electric and magnetic forces
698 are of equal magnitude but opposite directions:

699 $$qE = qvB$$

700 which gives the velocity of $v = E/B$ for undeflected ions (Fig. 13). Wien (1898) used a similar
701 device to measure the m/z ratios of electrons and protons. This design led to the development of
702 the "Wien filter" as a velocity selector in ICP-MS applications (e.g., Tsuno and Ioanoviciu 2013).

703 **3.5.3 Magnetic sector mass spectrometer**

704 The magnetic sector mass analyzer has its roots in the archetypal mass spectrograph developed
705 by Thomson (1913), which led to the discovery of stable isotopes. In Thomson's experiment,
706 gaseous atoms were ionized by an electric current in a partially evacuated tube. The positively
707 charged ions were set in a circular motion by the magnetic force, while the electric field applied
708 an acceleration in the direction parallel to the magnetic field. These combined fields caused the
709 ions to leave parabolic traces on the photographic plates corresponding to their m/z ratios. The
710 resolving power of this parabola apparatus was limited to ~15. As an alternative to photographic
711 film, Thomson (1912) also used a Faraday cup and an electroscope to quantify the charge intensity
712 of the beam, with which he obtained a mass spectrum. By gradually changing the magnetic field
713 strength, beams of different masses could be admitted sequentially through a slit into the Faraday
714 cup, working as a scanning mass spectrometer.

In separate but complementary efforts to improve the mass resolution, A. J. Dempster and F. W. Aston attempted to focus ions of a certain m/z ratio onto a single detection point. Dempster (1918) utilized electron bombardment to produce roughly monoenergetic ions and a 180^{o} magnetic sector to achieve direction focusing of the ions. Ions of similar kinetic energy followed semicircular paths of equal radius and crossed their paths at the detector slit regardless of their divergent angles at the entrance (Fig. 12B). The ions were collected in Faraday cups and detected with an electrometer. This mass spectrometer provided a resolution of 100 and was particularly useful for determining the relative abundances of ionic species. Bainbridge (1932) further improved the resolution of the Dempster-type instrument to 500 by adding a velocity selector ("Wien filter") before the magnet. Based on the mass of ^{7}Li measured with this instrument (Bainbridge 1933), together with the masses of ^{4}He and ^{1}H reported by Aston (1927), Bainbridge (1933) presented experimental proof of Einstein's mass-energy relation through the reaction of ^{7}Li + ^{1}H → 2^{4}He. Dempster (1935) later introduced spark ionization to analyze conductive solids, with which he discovered the rare isotope ^{235}U.

Alternatively, Aston (1919) designed a spectrograph that compensated for ion energy spread by velocity focusing, using spatially separated electric and magnetic fields. A vertical diaphragm was positioned behind the electric field to select ion beams with nearly parallel velocities. Upon entering the magnetic field, the ions were deflected in a direction opposite to their deflections in the electric field, and ions with lower velocities were deflected more than those with higher velocities in both fields. Consequently, ions with the same m/z ratio but slightly different velocities arrived at the same position on the photographic plate. With this mass spectrograph, isotope masses can be measured with an accuracy of 0.1% and a mass resolving power of 130. Aston (1927; 1937) upgraded his first spectrograph by using finer slits, more stable and stronger electric and magnetic

738 fields that doubled ion deflection angles. These improvements increased the resolution to 2000
739 and the accuracy to ~0.001%, which enabled Aston (1927; 1937) to precisely determine the
740 deviation of isotope masses from the whole number rule. The concept of using velocity focusing
741 together with direction focusing led to the development of double-focusing mass spectrometers, in
742 which the achievable mass resolution is not compromised by the initial divergence and energy
743 spread of ions.

744 Effective double-focusing relies on the coincidence of direction focusing with energy focusing,
745 which has benefited from the comprehensive formulation of ion trajectories through various
746 combinations of magnetic and electric fields in superimposition, or in tandem (e.g., Bartky and
747 Dempster 1929; Mattauch and Herzog 1934; Johnson and Nier 1953). The most common
748 configurations are derivatives of the Mattauch-Herzog and Nier-Johnson geometries. The
749 Mattauch-Herzog geometry uses a 31.82° electric sector followed by a 90° magnetic sector in the
750 opposite direction of curvature (Fig. 14A), offering simultaneous detection of a broad mass
751 spectrum along a focal plane. In comparison, the Nier-Johnson geometry uses a 90° electric sector
752 and a 60° magnetic sector with the same direction of curvature (Fig. 14B), which is widely used
753 in MC-ICP-MS for precise measurement of isotope ratios. In reversed Nier-Johnson geometry, the
754 magnetic sector is placed before the electric sector. This geometry is often used in single-collector
755 ICP-MS, where most ions are removed from the beam by mass filtering in the magnetic sector,
756 thereby reducing beam aberration, peak tailing, and backgrounds.

757 Sector-field mass analyzers provide flat-topped peaks and superior mass resolution (~ 300 to
758 over 10,000) for resolving isobaric interferences from analyte ions. This resolution is a significant
759 improvement over quadrupole-based instruments (~300-400) that typically have the unit mass
760 resolution, as discussed in the following section. In addition, the magnetic sector provides spatial

761 separation of ions according to their m/z ratios, which facilitates the simultaneous detection of
762 multiple ion beams with a detector array, thereby minimizing the temporal fluctuations associated
763 with ionization and ion transmission for isotopic ratio analyses with MC-ICP-MS.

764 **3.5.4 Quadrupole mass spectrometer**

765 Quadrupole-ICP-MS has dominated the first decade of ICP-MS development since its
766 commercialization in 1983. It remains the most widely used ICP-MS instrument today, owing to
767 its relatively small size, mechanical simplicity, and affordable cost. A quadrupole mass filter
768 contains four cylindrical or hyperbolic rods arranged parallel in a square array (Fig. 15). The metal
769 rods are commonly 15-25 cm long, and the ion source and detector are closely packed. The mass-
770 filtering mechanism is based on applying direct and alternating electric currents to the conductive
771 rods to allow the transmission of ions of one m/z ratio at a time. A reasonably good mass resolution
772 can be achieved at a rapid scanning rate (typically 2500-5000 amu/s) and a relatively low vacuum
773 requirement ($\sim 5 \times 10^{-5}$ Torr), with no need for an additional device for energy focusing.

774 An important analytical strength of the quadrupole mass analyzer is its ease of use in tandem
775 mass spectrometry (see review by Balcaen et al., 2015). For example, both gas chromatography
776 (GC) and liquid chromatography (LC) can be conveniently interfaced with a quadrupole to identify
777 separated compounds (e.g., Finnigan 1994). Quadrupole ICP-MS is also frequently combined with
778 LA and MC-ICP-MS for in situ geochemical analyses of mineral grains. For instance, a volume of
779 laser-ablated zircon fragments can be split into a quadrupole-ICP-MS for trace elemental analyses
780 and a MC-ICP-MS for U-Pb zircon dating and Hf isotopic analyses (e.g., Yuan et al., 2008).

781 The concept of a quadrupole mass filter, published by Paul and Steinwedel (1953), differs in
782 principle from mass spectrometers that produce a spectrum of ions separated in space (magnetic
783 sector instruments) or time (time-of-flight instruments). Instead, it works analogously to an

784 adjustable bandpass filter. It utilizes oscillating electric quadrupole fields to selectively transmit
785 ions within a specific m/z range (typically ≤ one mass unit) through the quadrupole each time. Ions
786 with m/z ratios beyond this narrow range will strike the rods before reaching the exit of the
787 quadrupole. The separation of ions with a specific m/z ratio is achieved by adjusting the electric
788 field and oscillating frequencies applied to the metal rods, and ions of each m/z ratio pass through
789 the quadrupole in sequence. While different masses are filtered sequentially, rapid ramping of the
790 voltages allows scanning over 0-250 amu within 100 ms. This high scanning speed gives
791 quadrupole mass spectrometers the ability to measure multiple elements rapidly.

792 The four rods of a quadrupole are arranged as two pairs in diagonal directions of the sample
793 path (Fig. 15). Both electrode pairs are supplied with a combination of constant direct current (dc)
794 of the same magnitude but opposite polarity, and RF alternating current (ac) that is 180° out of
795 phase. When no dc is applied, the RF-only electrodes serve as an ion-focusing component to direct
796 a wide range of m/z ions traveling down the quadrupole along its central axis. The ac voltages
797 applied to the electrodes focus and defocus the ion beams alternately every half period according
798 to their RF. When the rods are electrically positive, they exert equal forces on the positively
799 charged ions in opposite directions so that the ion beams converge to the center of the quadrupole
800 and get focused. By contrast, when the rods are electrically negative, the positively charged ions
801 are attracted toward the rods and defocused from the center.

802 Mass separation occurs when offsetting the ac voltage of each pair of electrodes by a constant
803 dc voltage in opposite directions to the same degree (Fig. 15). One pair of electrodes carries an
804 oscillating voltage with brief excursions to negative voltage during each period. The positively
805 charged ions are focused to the center of the quadrupole, except for a brief attraction toward the
806 rods when switched to the negative voltage. High-mass ions carry more momentum and stay longer

along the central axis of the quadrupole than ions with lower masses, which are attracted further toward the rods when the voltages are switched to negative. These low-mass ions get increasingly defocused from the central ion beam during every negative excursion of the voltages supplied to the rods. Eventually, they collide with the rods and become neutralized. Therefore, this electrode pair serves as a high-mass filter that blocks the transmission of ions with m/z ratios below a specific value.

The other pair of electrodes is supplied with an oscillating voltage with brief excursions to positive voltage during each period. In this case, positively charged ions are defocused from the central ion beam most of the time due to attraction to the negative electrodes, except for a brief focusing when the electrodes switch to positive voltage. These short excursions to positive voltage within each period would only exert sufficient focusing on relatively light ions to prevent them from striking the electrodes. In contrast, the brief focusing would be insufficient for ions with m/z ratios above a specific value. As a result, these high-mass ions are increasingly attracted toward the negative electrodes and eliminated from the ion beams as they reach the electrodes. Consequently, this pair of electrodes acts as a low-mass filter. The two pairs of electrodes work together to remove the transmission of ions with masses below and above a specific range at each setting. This way, the voltages can be adjusted to have a narrow bandpass that allows transmission through the quadrupole (Fig. 15).

3.5.4.1 Mathematical expression

In a quadrupole mass filter field, there is no acceleration along the central z-axis, and ions travel with constant velocity along this axis. The motions along the x and y directions of the symmetric hyperbolic electric field are governed by the Mathieu equation below [see Miller and Denton (1986) for the derivation of these equations].

$$\frac{d^2u}{d\xi^2} + [a_u - 2q_u \cos(2\xi)]u = 0$$

where u represents the coordinate axes x or y, and

$$a_x = -a_y = \frac{8zeU}{mr_0^2\omega^2}$$

$$q_x = -q_y = \frac{4zeV}{mr_0^2\omega^2}$$

$$\xi = \omega t/2$$

where U is the magnitude of the dc voltage, Vcos(ωt) describes the amplitude of the RF voltage, ω is the angular frequency, *t* is time in seconds, and r_0 represents the inscribed radius between the electrodes.

3.5.4.2 The a-q stability diagram

The parameters a and q in the Mathieu equation correlate positively with the magnitude of the dc potential (U) and the ac potential (V) applied to a quadrupole during a scan. Solutions of the equation can be plotted in *a-q* space to indicate whether an ion of a given mass has a stable trajectory through the quadrupole filter at the applied voltages. Any combination of *a* and *q* that lies within the triangular area corresponds to a stable ion trajectory along the X-Z and Y-Z planes (Fig. 16A). In practice, the dc and ac potentials are adjusted proportionally so that their ratios and the resolution are held constant, forming a scan line with a slope of 2U/V. A mass scan is completed by increasing U and V to allow ions with higher m/z ratios to pass through the quadrupole in succession (Fig. 16A and B).

The resolution of a quadrupole mass filter corresponds to the width of the scanning bandpass, which varies with the RF frequency and the U/V ratio. Increasing the RF frequency at a constant

U/V ratio causes ions to pass through more RF cycles in the quadrupole, leading to more efficient separation and higher resolution. Increasing the U/V ratio leads to a steeper slope and higher mass resolution, whereas decreasing the U/V ratio results in a broader bandpass (Fig. 16C) and possible peak overlap between ions with similar m/z ratios. Because the stability boundary on the high-mass side is steeper than that on the low-mass side, a decrease in resolution will cause the leading edge of the peak to shift more toward the lower mass than the shift of the trailing edge to the higher mass. Tailing on the low mass side of an ion peak can be reduced by limiting the kinetic energy spread of ions entering the quadrupole.

The application of quadrupole mass spectrometry is mainly limited by its unit mass resolution, which is insufficient to separate analyte ions from isobaric interferences in most cases. Therefore, quadrupole ICP-MS is primarily used for measuring elemental concentrations at high sample throughput (e.g., Houk et al., 1980; Date and Gray 1981; Date and Hutchison 1986). Stable isotope analyses by quadrupole instruments are restricted to low-mass elements where natural isotope fractionation is large and isobaric interferences are less of an issue. For example, Liu and Li (2019) achieved a long-term precision of 1.1‰ (2SD) for Li isotope analysis using only 2.5 ng Li. They pointed out that quadrupole ICP-MS is a practical alternative to MC-ICP-MS for analyzing low-Li samples with high matrix contents because the quadrupole mass filter is less sensitive to matrix effects, and electron multiplier detectors provide better counting statistics than Faraday cups at low-Li concentrations.

As an advantage of its robust unit mass resolution, the quadrupole mass filter can handle incoming ions with wide momentum and kinetic energy distribution. Furthermore, a quadrupole is an ideal preliminary mass filter because it filters mass by varying electric fields and rapid mass scanning. These analytical benefits have found wide applications in triple-quadrupole ICP-MS for

analyzing chemical structures or specific chemical reactions, where the first quadrupole selects a specific ion to be fragmented in the second quadrupole and analyzed in the third quadrupole (e.g., Yost and Enke 1979; Yost 2022). More recently, the quadrupole has also been used as a pre-collision-cell mass filter in MC-ICP-MS (e.g., Thermo-Fisher Proteus, Bevan et al., 2021; Lewis et al., 2022; Mahan et al., 2022).

3.5.5 Time-of-flight mass spectrometer

Time-of-flight (TOF) mass spectrometers measure the mass-dependent time required for microsecond pulses of accelerated ions to drift through a field-free vacuum flight tube (30-100 cm long) (Fig. 17). It can generate consecutive mass spectra of ions formed by laser ablation, electrothermal vaporization, and flow injection. In principle, TOF analysis is analogous to an ion race (Stephens 1946; Wolff and Stephens 1953): an electric field first accelerates a package of ions to the same kinetic energy. This acceleration gives each ion a characteristic velocity dependent on its m/z ratio, at which it drifts along a vacuum tube. Ions with different m/z ratios are spatially separated along the flight tube, and ions with lower mass reach the detector earlier than the heavier ions:

$$t = \frac{L}{v} = \sqrt{\frac{m}{z}} \times \frac{L}{\sqrt{2eV}}$$

The entire mass spectrum of the introduced ions is completed as ions arrive sequentially at the end of the flight tube and are registered digitally. The detection of ions with various m/z ratios is quasi-simultaneous as the process occurs rapidly.

The TOF analysis requires a precisely defined starting time for the ion race. Ions are sampled in pulses instead of being introduced continuously into the flight tube, so that a lighter ion introduced later would not overtake a heavier ion introduced earlier during free drift. The matrix-assisted laser desorption/ionization technique (MALDI) is typically used for pulsed ionization.

Alternatively, ions can be released from the source in packages through electrical "gates." In cases where ICP is used as the ionization source, the continuously formed ions are regulated by orthogonal acceleration using a set of pulsed-repeller plates aligned horizontally to the flight tube. The repeller plates send ions into the flight tube by applying a positive voltage to accelerate them perpendicular to their original direction. In contrast, no ions will be admitted into the flight tube when the repeller plates are uncharged. Current TOF analyzers can process up to 30,000 ion packages per second; therefore, they are ideal for monitoring transient signals.

The major limiting factor for the mass resolution of early TOF-MS instruments is the kinetic energy spread of ions prior to their admission to the flight tube (Cameron and Eggers Jr. 1948; Wiley and McLaren 1955). To overcome this limitation, an electrostatic reflector, known as the ion mirror, was developed (Mamyrin et al., 1973). The reflector is placed at the end of the flight tube and consists of a series of high-voltage electrode rings. The reflector first decelerates the incoming ions to a stop and then accelerates them again in the opposite direction (Fig. 17). In this way, the initial distribution of kinetic energy between ions is compensated for by the different distances the ions travel in the reflector: ions with higher velocities travel further into the reflector and fly longer distances than those with lower velocities. Consequently, ions with the same m/z ratio arrive at the detector concurrently regardless of their differences in kinetic energy.

3.6 Detectors

The detection system collects ions emerging from the mass analyzer and, based on the rate of ions delivered to the detector, generates electrical signals proportional to the concentration of analyte ions in a sample. The ion intensities of different m/z ratios are compared with the calibration or reference standards with known concentrations. Thus, the elemental concentrations in an unknown sample can be calculated. In isotopic ratio analyses, the relative beam intensities

of isotopes measured in a sample are compared with those of a standard. The precision of isotope analyses is primarily limited by the counting statistics and the electrical Johnson-Nyquist noise of the resistor in the feedback loop. This electrical noise arises from the random thermal motion of electrons in an amplifier when no current is applied (Nyquist 1928).

Most ICP-MS analyses involve measurements of ion beam intensities ranging from sub-femtoampere (1 fA = 10^{-15} A = 6242 ions/s) to nanoampere (1 nA = 10^{-9} A), which are amplified for quantification. Ion signals are typically detected by counting the number of electron pulses from single ion impacts per second, or by converting the induced electric current to a voltage for analog measurements (Fig. 18). Depending on the dynamic range required for the measurements, ion multipliers are used to measure low ion currents (e.g., between 10^{-19} A and 10^{-13} A), whereas Faraday cups are preferable for higher ion beams (e.g., between 10^{-15} A and 10^{-9} A) due to their exceptional linearity and stability at high ion currents (Fig. 19). The difference in dynamic range between these two types of detectors reflects their different mechanisms for detecting ions, which are described below.

3.6.1 Ion multipliers

The number of incoming ions is "multiplied" due to the emission of secondary electrons when the incident ion impacts the dynode surface of the detector. In a Daly detector (Daly 1960), positive ions are attracted to an off-axis conversion dynode held at a high negative voltage (~20 kV), which repels and accelerates secondary electrons toward a scintillator. The photons emitted from the phosphor screen are amplified and detected by a photomultiplier, which can be outside the vacuum chamber. In contrast, electron multipliers work under vacuum. The incident ion strikes the detector surface in the line of sight, releasing secondary electrons that cascade, leading to a gain of 10^3 to

941 10^8 so that the signal is readily detected as individual electron pulses (< 10^6 cps) or as an electron
942 current (~ 10^6 cps to >10^9 cps).

943 There are two main types of electron multipliers, depending on the number of electrodes used
944 (Fig. 18). In the discrete dynode multiplier, electron multiplication takes place between individual
945 dynodes that are connected by a series of resistors. The gain is adjusted by changing the negative
946 voltage (a few kV) applied to the first dynode. The voltage steps between dynodes are adjusted to
947 output the signal at ground potential. In comparison, the continuous dynode multiplier amplifies
948 the number of secondary electrons within a curved, cone-shaped glass tube. The inside of the tube
949 is coated with a thin layer of semiconducting material that has a high resistance to create a gradual
950 voltage drop along the path. A conversion dynode with a high negative voltage can be added before
951 the conventional electron multiplier so that the secondary electrons strike the multiplier with
952 substantially higher kinetic energy, thereby reducing the mass dependence of the secondary
953 electron emission.

954 Daly detectors and electron multipliers offer complementary advantages. Daly detectors are
955 more robust and deliver better linearity, especially at high count rates. Furthermore, the dynamic
956 range of Daly detectors are wider than that of electron multipliers. On the other hand, electron
957 multipliers are smaller and less expensive. They are the standard detector for single-collector ICP-
958 MS and their high signal-to-noise ratio is suitable for counting low-intensity ion beams. The
959 background noise of an ion multiplier is typically a few counts per minute, which is negligible
960 compared to ion signals of hundreds to millions per second (Carlson 2014). However, the counting
961 capability of the electron multiplier becomes limited at count rates higher than a few million cps
962 (Fig. 19), as there will be a short "dead time" (a few ns to tens of ns) during which the detector
963 cannot identify an incoming signal. Due to the restricted dynamic range of electron multipliers, a

Faraday cup can be added to the single-collector ICP-MS to extend the maximum countable rate from 10^9 cps to 10^{12} cps, enabling measurements of trace and major elements during a single scan (Wiedenbeck et al., 2012).

3.6.2 Faraday cup

A Faraday cup is an electrode connected to the electrical ground via a high-resistance amplifier for signal integration. The Faraday cup detects ions by neutralizing their positive charges with electrons flowing from the electrical ground. As the electric current passes through the amplifier, it is converted to a voltage for measurement. Assuming that 10^8 ions with a fundamental electron charge of 1.6×10^{-19} coulomb strike the collector per second, together they deliver a beam current of 1.6×10^{-11} A, which corresponds to an output voltage of 1.6 V for a standard Faraday cup with a 10^{11} Ω amplifier. The use of such a high-ohm resistor for signal amplification causes a background noise on the order of 10^{-16} A, which is significant compared to typical ion signals of 10^{-14} to 10^{-10} A (Carlson 2014), and is compensated for by an extended measurement duration of several hundred seconds. Isotope abundance ratios are often measured with inter-calibrated Faraday cups, as their high signal stability facilitates high-precision ratio measurements.

A critical consideration in designing Faraday cups is to reduce the generation and scattering loss of secondary electrons. Therefore, Faraday cups have a long and narrow "bucket" shape, with a base typically made of highly porous carbon. The electron trapping efficiency of the Faraday cup can be enhanced by steering electrons through a magnetic field in a spiral trajectory and increasing their chance of hitting the collector wall. In addition, Faraday cups have a metal slit, behind which a second electrode, known as the suppressor, is inserted and supplied with a potential of –50 V to –100 V (Fig. 18). This negative electrode effectively repels the secondary electrons emitted from

the slit when ions strike on it. It also helps to prevent the loss of electrons formed within the Faraday cup by repelling them back to the base.

3.6.3 Multi-detection arrangement

A major advance in the ion detection system came with the coupling of a multi-collection array (Fig. 18) to the ICP-MS, which enables simultaneous detection of all relevant ion signals for high-precision isotopic ratio analyses (e.g., Walder and Freedman 1992; Walder et al., 1993; Wieser and Schwieters 2005). Given their compact size, more than 10 Faraday cups can be readily fitted into a multi-collection block, and several ion multipliers can be accommodated in addition to them. Since the introduction of MC-ICP-MS, the detection system has undergone several significant upgrades, including an increased number of detectors (up to 16 Faraday cups), a larger dynamic range for standard Faraday cups (55 V vs. 11 V on 10^{11} Ω resistors), an improved signal-to-noise ratio of the Faraday cup with new amplifier designs, and a dual-mode detector arrangement for convenient switching between the Faraday cup and electron multiplier.

The state-of-the-art multi-detection system features a switchable amplifier design to accommodate diverse applications. Amplifiers with 10^{9} Ω and 10^{10} Ω feedback resistors facilitate the measurement of elements with isotopes that occur in significantly different abundances, such as V (e.g., Nielsen et al., 2011; Wu et al., 2016). On the other hand, amplifiers with 10^{12} Ω and 10^{13} Ω resistors have been developed to bridge the detection limits between Faraday cups and ion multipliers (Fig. 19) (e.g., Wieser and Schwieters 2005; Breton et al., 2015). Results from Koornneef et al. (2014) show that with a 100-fold increase in resistivity, the signal-to-noise ratio of the amplifier is improved by a factor of up to five. Furthermore, the 10^{13} Ω Faraday cup potentially offers higher precision than electron multipliers for beam sizes greater than 20 kcps. This new amplifier has greatly expanded the potential for high-precision isotopic analyses for

small-sized samples (e.g., laser ablation, carbonate, or biological samples) and low-abundance isotopes (e.g., Ta and Re) using MC-ICP-MS (Pfeifer et al., 2017; Steinmann et al., 2019; e.g., Dellinger et al., 2020; Grigoryan et al., 2020).

4 Analytical interferences in ICP-MS

While a highly efficient ICP source offers valuable analytical benefits, the trade-off is that a variety of interfering species could be introduced into the analyzer region along with the ions of interest. These interferences are the main factor limiting the accuracy and precision of ICP-MS analyses. They can be divided into two broad groups, i.e., spectral and non-spectral, which are discussed below.

4.1 Spectral interferences

Spectral interferences occur when unwanted ionic species, either isobaric or polyatomic, have the same nominal m/z ratio as the analyte ions. These interferences result in spectral overlap, causing the true analyte signal to be overestimated. Isotopic analysis is particularly susceptible to spectral interferences as it requires the measurement of two or more interference-free isotopes. In contrast, a small amount (0.1-1%) of spectral overlap can be tolerated in elemental analysis. Spectral interferences originate from various sources, including the sample matrix, solvent (e.g., H_2O, HNO_3, and HCl), plasma gas (typically Ar), and plasma-entrained air (e.g., N_2, O_2, and CO_2). Isobaric interferences occur when other elements have naturally occurring isotopes at the same mass as the analyte (e.g., Ar, K, and Ca at mass 40). Polyatomic interferences arise from the combination of two or more atomic ions, typically in the form of Ar-related species, oxide and hydroxide, and Cl-, S-, or P-based species.

When Ar serves as the plasma gas, the most common interferences are Ar^+, Ar_2^+, and argides. Argon has three naturally occurring isotopes: ^{36}Ar (0.337%), ^{38}Ar (0.063%), and ^{40}Ar (99.6%). ^{40}Ar is a severe isobaric interference on ^{40}K, a minor isotope of K (0.0117%). It also interferes with ^{40}Ca (94.961%), the dominant Ca isotope. The various combinations of Ar isotopes form a series of interferences on Se isotopes, particularly $^{40}Ar_2$ that interferes with the major Se isotope (^{80}Se). A variety of Ar-related polyatomic ions can form in the mass range between 14 and 90 due to the combination of Ar with the sample solvent (e.g., Tan and Horlick 1986). For example, $^{40}Ar^{16}O^+$ interferes with the dominant Fe isotope ($^{56}Fe^+$), while $^{40}Ar^{14}N^+$ and $^{40}Ar^{16}O^1H^+$ interfere with $^{54}Fe^+$ and $^{57}Fe^+$, respectively. Argides also significantly affect K isotope measurements, with $^{38}ArH^+$ and $^{40}ArH^+$ directly interfering with $^{39}K^+$ and $^{41}K^+$, respectively. For samples containing organics, $^{40}Ar^{12}C$ may interfere with the dominant Cr isotope (^{52}Cr), and $^{40}Ar^{14}N$ may interfere with ^{54}Cr.

While an ICP source produces mainly singly charged ions, a small percentage of other ionic forms may be present. Doubly charged ions occur mostly in alkaline earth elements, forming interference peaks at half their masses (e.g., $^{48}Ca^{2+}$ on $^{24}Mg^+$). Refractory elements typically combine with ^1H, ^{16}O, or $^{16}O^1H$ from the air or sample solvent to form molecular interferences such as hydrides, oxides, and hydroxides. For example, Ti has five naturally occurring isotopes: ^{46}Ti (7.99%), ^{47}Ti (7.32%), ^{48}Ti (73.98%), ^{49}Ti (5.46%), and ^{50}Ti (5.25%). Their oxides form interferences on ^{62}Ni ($^{46}Ti^{16}O$), ^{63}Cu ($^{47}Ti^{16}O$), ^{64}Zn ($^{48}Ti^{16}O$), ^{65}Cu ($^{49}Ti^{16}O$), and ^{66}Zn ($^{50}Ti^{16}O$). The formation of oxides relative to atomic ions depends on their respective bond strength with oxygen, and is particularly problematic for refractory elements with high bond strength (e.g., REEs, Ba, and Ca).

4.2 Non-spectral interferences

In contrast to spectral interferences that directly overlap with the m/z ratio of the analyte, non-spectral interferences reflect changes in analyte throughput between samples due to physical and chemical differences in the sample matrices. The physical properties of the sample matrices, such as viscosity, surface tension, evaporation rate, and vapor pressure, can affect the ionization temperature in the plasma or the mass discrimination as an ion beam passes through the expansion chamber (Longerich 1989). In addition, analyte transmission efficiency is susceptible to matrix elements. For example, a high loading of easily ionizable elements (e.g., Na) to the plasma may reduce plasma energy and suppress the ionization of analytes. The suppression of the analyte signal can also be due to space charge effects in the interface region, where coulomb repulsion between positively charged ions defocuses the ion beams (Gillson et al., 1988; Tanner 1992). If a sample contains an excess of heavy matrix elements, the lighter analyte ions will be more strongly deflected from the central ion path than the heavier matrix ions, resulting in a lowered analyte sensitivity.

5 Approaches to overcome interferences

Spectral and non-spectral interferences significantly affect the accuracy of elemental concentration and isotopic ratio analyses; therefore, they must be eliminated or corrected appropriately. An ideal approach to avoid spectral interferences of an analyte is to measure the signals of its interference-free isotopes with relatively high natural abundances. However, this approach does not apply to elements with isotopes of low natural abundances, or with only a single isotope (e.g., As, Co, Sc, and Mn). Therefore, various alternative approaches have been developed to reduce the interferences with ICP-MS (e.g., see reviews by Evans and Giglio 1993; Lum and

Leung 2016). It is important to emphasize that the most practical approaches should be tailored for the specific element.

5.1 Choice of sample solvents

For ICP-MS measurements, samples are usually dissolved in dilute HNO_3 because its three constituent elements are also present in the entrained atmospheric gases. In contrast, HCl is less frequently used because Cl readily forms complex ions interfering with analyte ions. This is particularly the case for As, which occurs only as ^{75}As (overlapping with $^{40}Ar^{35}Cl^+$), and for V, which has its dominant isotope (^{51}V) overlapping with $^{35}Cl^{16}O^+$. Sulfuric acid and H_3PO_4 are generally not recommended because they can form a variety of S- and P-bearing polyatomic ions. For example, $^{32}S^{16}O^+$ and $^{31}P^{16}O^1H^+$ are direct interferences on $^{48}Ti^+$, and $^{32}S^{16}O_2^+$ is a direct interference on $^{64}Zn^+$. In addition, $^{31}P^{14}N^+$ interferes with ^{45}Sc, the only Sc isotope, and $^{31}P^{16}O_2^+$ interferes with ^{63}Cu, the major Cu isotope. One effective approach to suppress hydride formation is to replace H_2O with D_2O, which eliminates the major polyatomic interference of $^{36}ArH^+$ on $^{37}Cl^+$, thereby enabling the accurate determination of $^{37}Cl/^{35}Cl$ ratios (Smith and Houk 1990).

5.2 Analyte-matrix separation

For precise and accurate isotopic analyses, it is recommended to separate the analyte from the matrix elements. Chromatographic separation is commonly used, and is based on affinity to the ion exchanger, hydrophobic/hydrophilic properties, size (size-exclusion chromatography), or other less frequently used methods. Chromatographic separation can be performed online or offline, depending on the nature of the sample and analyte. Matrix components that readily form insoluble compounds can be removed by precipitation. For example, Cl-related interferences can be removed by adding $AgNO_3$ to precipitate as AgCl (Lyon et al., 1988). Precipitation of Ca in the form of calcium sulfates has also been used to separate Mg from Ca in carbonates (Bao et al.,

2019). Alternatively, a vapor generation device can be used to convert hydride-forming elements into volatile species, which are subsequently separated and concentrated from the residual solutions (e.g., Powell et al., 1986; Buckley et al., 1992; and see section 3.1.3).

5.3 Sample desolvation

Because water is the primary source of H- and O-related polyatomic interferences, the formation of these molecular ions can be effectively reduced by a desolvation nebulization system (e.g., Gustavsson and Hietala 1990; and see section 3.1.2.2). This method applies to all elements, regardless of their tendency to form volatile species. As measured by the ratios of CeO^+/Ce^+, oxide formation decreases from 3.5% for typical "wet" plasma introduction to 0.01-0.08% for various designs of "dry" plasma introduction systems, with an increase in sensitivity by at least an order of magnitude.

5.4 Modifying the plasma

5.4.1 Mixed-gas plasma

By feeding an extra gas to a desolvation nebulization system, it is possible to further reduce polyatomic interferences, mass bias, and oxide formation (e.g, Lam and McLaren 1990). This additional gas is usually blended into the nebulizer gas, as this causes less plasma perturbation and is more efficient than mixing it into the coolant gas at a much higher flow rate. The most commonly used gas is N_2, a molecular gas with a similar ionization energy to Ar (Fig. 1(a)) but a higher thermal conductivity and electrical capacity. The presence of N changes the electrical and spectral properties of the Ar plasma, its ionic composition, and the population of Ar energy levels.

The principal ionization mechanism in an Ar-N_2 plasma may differ from that in an all-Ar plasma. It has been suggested that abundant metastable Ar atoms are present in Ar plasma, which can be readily ionized to Ar^+, or they can enhance the ionization of analyte elements by Penning

ionization (Boumans and De Boer 1977). In an Ar-N_2 plasma, the energy of the lower metastable level of Ar atoms is slightly higher than the excitation of vibrational levels of N_2 molecules by electron impact. This leads to efficient collisional energy transfer that quenches the metastable Ar by exciting the vibrational levels of N_2 molecules (Wagatsuma and Hirokawa 1989). The reduced density of metastable Ar in the plasma makes Penning ionization of the analyte less likely. On the other hand, the N_2, N_2^+, and N^+ species are highly active in scavenging O_2 to form NO^+. Based on ion distributions measured in a mixed Ar-N_2 plasma, ionization is suggested to occur primarily by charge transfer with NO^+, N_2^+, or Ar^+ (Houk et al., 1983; Holliday and Beauchemin 2002; Holliday and Beauchemin 2003).

The formation of polyatomic and oxide interferences can be significantly reduced in an Ar-N_2 plasma where ionization is dominated by charge transfer with NO^+. Adding low-flow of N_2 (30 mL/min, < 5% vol./vol.) to the nebulizer gas has been shown to considerably reduce the formation of $ArCl^+$, $ArAr^+$, and ArO^+, possibly due to the competitive formation of N-based polyatomic species (Evans and Ebdon 1989; Evans and Ebdon 1990). In addition, the ionization energy of NO^+ is lower than that for most Ar- and Cl-based polyatomic interferences, which limits their production in an Ar-N_2 plasma. The formation of NO^+ also effectively sequesters oxygen, thereby reducing oxide production (Lam and Horlick 1990; Holliday and Beauchemin 2003). Moreover, N actively quenches excited state pathways of certain oxide species in the expansion chamber, as illustrated by NdO^+ (Newman et al., 2009). Finally, the presence of N in the nebulizer gas has also been shown to mitigate the effects of matrix elements on sensitivity (van der Velde-Koerts and de Boer 1994).

Along with the reduced formation of polyatomic ions in a mixed Ar-N_2 plasma, it has been observed that the sensitivity of many elements increases with careful optimization of gas flow

rates, sampling depths, and other parameters. The addition of N_2 causes the plasma volume to contract along the torch axis (Greenfield and McGeachin 1978; Choot and Horlic 1986; Lam and Horlick 1990; Sesi et al., 1994), thus the power density increases around its toroidal region. Since N_2 has a higher thermal conductivity than Ar, the presence of N_2 may lead to enhanced energy transfer from the toroidal region of the plasma to its central channel. However, N_2 molecules also absorb energy, which results in the cooling of the central channel. Therefore, the amount of N_2 added to the nebulizer gas likely affects the competition between energy loss to the central channel and energy transfer from the toroidal region. In ICP-OES and ICP-MS analyses, signal enhancement is generally observed at a low flow rate of N_2. In contrast, high flow rates of N_2 can lead to signal reduction or even plasma extinction (see review by Scheffler and Pozebon 2014).

The effect of N_2 addition on signal enhancement depends on the element being analyzed, particularly its ionization energy and its tendency to form a strong metal-oxygen bond. The efficient formation of NO^+ molecules in an Ar-N_2 plasma would reduce oxygen availability for metals that tend to form oxides, and these metals may exhibit a corresponding increase in ionic signals (Lam and Horlick 1990). In addition, charge transfer with NO^+ can enhance the ionization of elements with relatively high ionization energies. The improved thermal conductivity in Ar-N_2 plasma may also be responsible for the observed signal enhancements, as supported by a broad positive correlation between the signal enhancement factor and ionization energy of various elements in LA-ICP-MS measurements (Hu et al., 2008).

5.4.2 Cold plasma

Operating the Ar plasma at a reduced RF power (i.e., cold plasma) can effectively suppress the formation of Ar-related spectral interferences (Jiang et al., 1988). This method leverages the high ionization energy of Ar compared to elements with masses similar to Ar and its polyatomic ions

1168 (e.g., K, Ca, Fe, Cr, and Cu, see Fig. 1). Elements with sufficiently low ionization energies can be
1169 efficiently ionized in a cold plasma while the ionization of Ar is strongly reduced. Moreover,
1170 ionization in a cold plasma is suggested to occur primarily via charge transfer with NO^+, similar
1171 to that in a mixed Ar-N_2 plasma (Tanner 1995; Holliday and Beauchemin 2002). Therefore, when
1172 using cold plasma, especially with a desolvation nebulization system, NO^+ becomes the
1173 predominant background species, while Ar^+, ArO^+, and ArH^+ are significantly reduced (Jiang et
1174 al., 1988).

1175 The use of cold plasma has shown enhanced detection limits for elemental concentrations (low
1176 ppt levels) and improved precision for isotope ratio measurements, as studied for Li, Fe, K, and
1177 Ca (e.g., Sakata and Kawabata 1994; Tanner et al., 1995; Murphy et al., 2002). Notably,
1178 Chernonozhkin et al. (2017) have shown that a precision of ±0.04‰ (2SD) can be achieved for
1179 $^{56}Fe/^{54}Fe$ ratios with a low mass resolving power ($RP_{edge\ 5,95\%}$) of 300, owing to negligible
1180 interferences from $^{40}Ar^{16}O^+$ (on $^{56}Fe^+$) and $^{40}Ar^{14}N^+$ (on $^{54}Fe^+$) and reduced instrumental mass
1181 discrimination using cold plasma (600 W) (Fig. 20). This level of precision is similar to that
1182 typically achieved using hot plasma (1260 W), with which a significantly higher $RP_{edge\ 5,95\%}$ of
1183 4500 is required to resolve Ar-related interferences. Likewise, direct measurement of the $^{44}Ca/^{40}Ca$
1184 ratio with MC-ICP-MS is made possible by a decreased $^{40}Ar/^{40}Ca$ ratio from 0.1 to 0.002 when
1185 the RF power is reduced from 1250 W to 400 W (Fietzke et al., 2004). In addition to Ar, carbon-
1186 based interferences (C_2^+, C_2H^+, $C_2H_2^+$ and CN^+) are significantly reduced, which facilitates high-
1187 precision measurements of Mg isotopes (Choi et al., 2012) and Li isotopes (Bryant et al., 2003;
1188 Choi et al., 2013), particularly for the analysis of low-Li carbonate samples using single-collector
1189 quadrupole ICP-MS (Misra and Froelich 2009).

While cold plasma is a valuable option for analyzing elements susceptible to Ar-related interferences, it has several potential drawbacks compared with conventional hot plasma (Tanner 1995; Bryant et al., 2003). First, non-spectral interferences appear to be greater under cold plasma conditions. Second, oxide formation may be more pronounced for some metals under cold plasma conditions. For example, the formation of $^{40}CaO^{+}$ would directly interfere with $^{56}Fe^{+}$ and underestimate the $^{40}Ca^{+}$ signal. Third, certain interferences remain at significant levels, and in these cases, a combination of cold plasma and high mass resolution is necessary, such as for the accurate determination of $^{41}K^{+}$ ($^{40}Ar^{1}H^{+}$), $^{57}Fe^{+}$ ($^{40}Ar^{16}O^{1}H^{+}$), and $^{54}Fe^{+}$ ($^{40}Ar^{14}N^{+}$). Considering these limitations, hot plasma is preferred for most elements due to its higher sensitivity and stability.

5.5 Collision/reaction cell

Collision/reaction cell (CRC) technology has found diverse applications before being adapted for removing polyatomic interferences in ICP-MS. The early development of CRC was motivated by research in the physical chemistry of gaseous ions. For example, Von Zahn and Tatarczyk (1964) used an RF-only quadrupole field in a pressurized flight tube between two mass spectrometers to quantify collision-induced dissociations (CID) of polyatomic ions. Futrell and Miller (1966) added a collision chamber between two double-focusing mass spectrometers to study ion-molecule reactions. In subsequent studies, the sector-field mass spectrometers were replaced by two quadrupole mass filters to improve the ion transmission efficiency (Iden et al., 1972; Yu et al., 1972), and an RF-only quadrupole was inserted in between for photodissociation of polyatomic ions (Vestal and Futrell 1974; McGilvery and Morrison 1978). In a following study, Yost and Enke (1978) introduced triple quadrupole mass spectrometry to analytical chemistry, with mass selection of ions in the first quadrupole, collisional fragmentation of selected ions in the second quadrupole (RF-only), and analysis of fragmented ions in the third quadrupole. Since then, this

1213 configuration has become widely adopted for structural and trace mixture analyses of complex
1214 organic molecules (Yost and Enke 1979; Yost 2022).

1215 Several techniques have been explored to remove polyatomic interferences using CID. Initial
1216 experiments with triple quadrupole mass spectrometers yielded promising results from glow
1217 discharge mass spectra, suggesting that specific polyatomic ions (e.g., ArO^+) can be eliminated or
1218 reduced by dissociating their chemical bonds (King and Harrison 1989). However, using ICP-MS,
1219 Douglas (1989) found that the collision energy required to dissociate many polyatomic ions is
1220 greater than the difference in ionization energy between the analyte ions and the Ar atoms. As a
1221 result, CID would promote the neutralization of analyte ions by electrons transferred from Ar
1222 atoms. In this case, the loss of analyte ions due to scattering and charge transfer outweighs the
1223 benefit of dissociating polyatomic ions by collision. Nevertheless, D.J. Douglas noticed that Ce^+
1224 reacted with O_2 much more efficiently than CeO^+ when air was introduced into the quadrupole and
1225 suggested that ion-molecule chemistry in a collision cell might help alleviate molecular
1226 interferences.

1227 Rowan and Houk (1989) investigated the potential for chemical resolution of polyatomic
1228 interferences using a quadrupole collision cell connected between the ICP source and a quadrupole
1229 mass filter. They observed effective attenuation of Ar_2^+, ArO^+, and ArN^+ when Xe or CH_4 were
1230 used for the reactions, and efficient removal of unwanted ions by kinetic energy discrimination.
1231 Subsequent work has elaborated on the high selectivity of ion-molecule chemistry using different
1232 gases (H_2, O_2, and CH_4) to remove plasma matrix ions (Barinaga et al., 1994; Koppenaal et al.,
1233 1994; Eiden et al., 1996; Eiden et al., 1997; Eiden et al., 1999). At the same time, efforts were
1234 made to reduce the substantial loss of analyte ions (30-50%) due to collisions with the background
1235 gas. Douglas and French (1992) reported improved ion transmission by feeding the cell with a

buffer gas, which provides collisional focusing of the ion beam. Further improvements in transmission were achieved by using a higher-order multipole (Eiden et al., 1997; Turner et al., 1997; Feldmann et al., 1999). These improvements led to commercially available CRC-equipped ICP-MS instruments.

The use of RF-driven multipole CRC in ICP-MS has been discussed in detail by Koppenaal et al. (2004). The choice between quadrupole, hexapole, or octopole depends on the specific analytical purpose. A quadrupole offers the unique advantage of selecting target ions through a narrow, user-chosen m/z range while rejecting all ions outside this range. However, a quadrupole produces a steep and narrow potential field (Fig. 21) that requires collisional focusing to reduce scattering losses. It is thus necessary to use relatively heavy molecular gases with large cross-sections (e.g., NH_3 and CH_4) to induce abundant ion-molecule interactions. In comparison, lighter gases (e.g., He and H_2) are generally used in a hexapole or octopole because they have wider and flatter potential well minima, which result in a larger ion stability region that allows simultaneous transmission of ions with different masses at high efficiency (Fig. 21). Furthermore, the larger ion stability region in higher-order multipoles ensures a greater gas thickness (at comparable pressures), which increases the number of collisions and, thus, the reaction efficiency. In summary, a quadrupole CRC works with more reactive gases, while a hexapole or octopole CRC works with more selective gases.

In essence, CRC is a type of ion-guiding lens pressurized with gases. When filled with a chemically inert gas (e.g., He), it acts as a collision cell that attenuates polyatomic interferences by kinetic energy discrimination (Fig. 22). Because polyatomic ions have larger sizes than atomic analytes with the same nominal mass, they would collide more frequently with the buffer gas and lose more kinetic energy. These low-energy polyatomic interferences can thus be readily filtered

out at the exit of the cell by applying a bias voltage. However, kinetic energy discrimination is less effective for isobaric interferences that occur as singly and doubly charged ions (Fig. 23A), which require chemical resolution (Fig. 23B-D).

When the CRC is supplied with a reactive gas (e.g., H_2), ion-molecule reactions are the primary mechanism to achieve chemical resolution between analyte ions and spectral interferences (see reviews by Tanner et al., 2002; Balcaen et al., 2015). By supplying a specific reactive gas, ion-molecule chemistry can either occur exclusively with the spectral interferences to eliminate them from the m/z region of interest (on-mass reaction mode, Fig. 23B), or the reaction gas selectively reacts with the atomic ions of interest to form molecular ions that can be measured in a higher m/z, 'cleaner' region (mass-shift mode, e.g., detection of $^{75}As^+$ as $^{75}As^{16}O^+$). In mass-shift mode, it is possible that certain matrix elements in the sample (e.g., $^{91}Zr^+$) form isobaric interferences with the product molecular ions ($^{75}As^{16}O^+$, Fig. 23C). A mass filter can be added before the reaction cell to reject non-target masses (Fig. 23D), ensuring that the ions entering the reaction cell are not affected by the composition of the sample matrices.

The on-mass reaction mode is widely used in ICP-MS to electrically neutralize and remove Ar-related interferences (e.g., Ar^+, ArO^+, $ArCl^+$, and ArH^+). This process involves charge transfer between the interference species and the reaction gas, taking advantage of the high ionization energy of Ar-based interferences ($\geq$ 15.76 eV) compared to most analyte ions. Spontaneous charge transfer occurs when the ionization energy of the reaction gas is lower than that of the interfering species but higher than that of the analyte ions (Fig. 24A). Hydrogen gas with an ionization energy of 15.42 eV is often used to react with Ar^+, while the analyte ions are unaffected. The reaction forms simple product ions with low m/z ratios (Eiden et al., 1996). For example, electrons can be

spontaneously transferred from H_2 to Ar^+ (e.g., $Ar^+ + H_2 \rightarrow Ar + H_2^+$), freeing m/z = 40 for the measurement of $^{40}Ca^+$.

On-mass interferences can also be eliminated by converting into a new ionic species with a different m/z ratio. These reactions typically involve proton transfer ($AH^+ + B \rightarrow BH^+ + A$), hydrogen atom transfer ($A^+ + BH \rightarrow AH^+ + B$), and hydride ion transfer ($A^+ + BH \rightarrow B^+ + AH$) due to the fast reaction rate of small-sized hydrogen (Tanner et al., 2002). For instance, ArO^+ and $ArOH^+$ have lower ionization energies than H_2, so they cannot be neutralized by charge transfer with H_2. Instead, these interferences can be removed through successive exothermic reactions of $ArO^+ + H_2 \rightarrow ArOH^+ + H$ and $ArOH^+ + H_2 \rightarrow H_2O^+ + Ar + H$ (Arnold et al., 2008). Another example is the proton transfer reaction of $ArH^+ + H_2 \rightarrow H_3^+ + Ar$ to remove ArH^+, which is a major interference on $^{41}K^+$ (e.g., Li et al., 2016).

Instead of using a gas to selectively react with the interferences (i.e., the on-mass reaction mode), the mass-shift mode increases the mass of an analyte ion by a known value, thus separating it from the spectral interferences. This approach is particularly useful for ionic species that exhibit significantly different chemical reactivity toward a specific reactive gas. Oxidation is commonly used because it exploits the large difference in oxygen affinity between the atomic ions of interest and the polyatomic interferences (Fig. 24(b)). General oxidizing agents such as N_2O and CO_2 have the advantage of forming stable reaction products (e.g., N_2 and CO). In comparison, targeted oxidation of specific ions can be achieved by reactions with O_2 or NO, which require strong A^+-O bonding. Exothermic oxidation by O_2 has facilitated the measurement of S and P concentrations by converting them to SO^+ and PO^+, thereby shifting their masses away from those of polyatomic interferences (e.g., NO^+, NOH^+, CH_3O^+, $^{16}O_2^+$) (Bandura et al., 2002).

The mass-shift mode has also been applied to in situ Rb-Sr dating with LA-ICP-MS(-MS) (e.g., Moens et al., 2001; Cheng et al., 2008). These applications are based on the significantly different electronic configurations of $Sr^+(s^1)$ and Rb^+ (s^0), which result in their distinctive chemical reactivities. $Sr^+(s^1)$ is highly reactive toward a variety of gases (denoted as MX) and forms Sr-bearing complexes, such as SrF^+ by F-atom transfer with CH_3F and SF_6, $SrCl^+$ by Cl-atom transfer with CH_3Cl, and SrO^+ by O-atom transfer with N_2O. In contrast, Rb^+ (s^0) has a noble-gas electronic configuration and is inert or reacts only very sluggishly with these gases. Therefore, the ratios of $^{87}Sr/^{86}Sr$ and $^{87}Rb/^{86}Sr$ can be measured as $^{87}SrMX/^{86}SrMX$ and $^{87}Rb/^{86}SrMX$, respectively.

The CRC has proven to be an effective and affordable technique for overcoming spectral interferences in quantitative elemental analysis with the ICP quadrupole mass spectrometer. Its previous application in magnetic sector mass spectrometers was limited to a discontinued single-focusing MC-ICP-MS (i.e., IsoProbe-P, Feldmann et al., 1999). This instrument primarily utilized the CRC to reduce the ion kinetic energy spread (from 20-30 eV to ≤ 2 eV) by collisional energy damping; therefore, high-precision isotopic analysis can be performed (Turner et al., 1997). IsoProbe-P has achieved variable levels of success in determining isotope ratios, particularly for isotopes that are severely affected by polyatomic interferences but are of significant planetary, geological, and biological importance, such as Si (Chakrabarti and Jacobsen 2010; Sun et al., 2010), Fe (Guilbaud et al., 2010), Se (Rouxel et al., 2002), Ca (Huang et al., 2010), and K (Li et al., 2016; Wang and Jacobsen 2016). These promising results have sparked interest in using a CRC on double-focusing MC-ICP-MS for more precise and accurate isotopic analysis.

Currently, four models of MC-ICP-MS offer a CRC option, all of which utilize an RF-only hexapole. The Sapphire model, manufactured by Nu Instruments, features a switchable conventional mode and CRC mode (Fig. 25). The conventional mode functions as a Nu Plasma 3

1326 double-focusing MC-ICP-MS with an acceleration voltage of 6 kV. When switching to the CRC
1327 mode, ions are first accelerated with a voltage of 4 kV and then slowed down slightly before
1328 entering an off-axis CRC. After the reaction, the ion beam is focused onto the exit slit and
1329 reaccelerated by a voltage of 4 kV. Compared with isotopic analyses performed using high mass
1330 resolution with considerably reduced sensitivity (e.g., Hu et al., 2018; Morgan et al., 2018), the
1331 Sapphire CRC mode provides high-precision isotopic analyses for K (Ku and Jacobsen 2020; Chen
1332 et al., 2021; Moynier et al., 2021; Li et al., 2022; Zheng et al., 2022; An et al., 2023), Ca (Dai et
1333 al., 2022; Gao et al., 2022), and Fe (Wang et al., 2022) using low mass resolution without
1334 compromising the sensitivity. The CRC unit can also be implemented on the Nu Sapphire 1700
1335 platform with an extended geometry (An et al., 2023), achieving high chemical resolution and high
1336 mass resolution.

1337 The other three models of CRC-MC-ICP-MS are built on platforms from Thermo Fisher
1338 Scientific, with the addition of a pre-cell mass filter to select the m/z "windows" entering the CRC
1339 (Fig. 26). This configuration is promising for laser-ablation applications that do not require
1340 chemical purification of the analyte. A prototype model named Proteus was built by combining
1341 the ion source, a modified quadrupole mass filter, and the CRC of the iCAP-Q-MS with a Neptune
1342 Plus MC-ICP-MS. While this instrument has been used for high-precision K (Mahan et al., 2022)
1343 and Ca (Lewis et al., 2022) isotopic analyses and in situ Rb-Sr dating (Bevan et al., 2021), its
1344 analytical capability was limited by the low sensitivity and strong non-exponential mass bias
1345 associated with the quadrupole mass filter (Craig et al., 2021). To overcome these limitations, an
1346 upgraded prototype instrument named Vienna was developed. This instrument, commercially
1347 known as Neoma, features a double "Wien filter" for mass selection and is tailored for coupling
1348 with the Neptune XT MC-ICP-MS (Craig et al., 2021). The potential of this new instrument has

been successfully demonstrated by a study of in situ ^{87}Rb-^{87}Sr measurements on minerals using SF_6 gas (Dauphas et al., 2022) and high-precision Cu isotopic analysis using helium gas to remove $^{40}Ar^{23}Na^+$ interferences on $^{63}Cu^+$ (Télouk et al., 2023). The conventional applications of Neoma were also illustrated by high-precision K (Télouk et al., 2022), U (Zirakparvar et al., 2023), and Ti (Deng et al., 2023) isotopic analyses.

5.6 High-resolution

For ICP-MS instruments with a magnetic sector, their inherent high mass resolution can physically separate spectral interferences from analyte masses (e.g., Bradshaw et al., 1989). This method is a convenient alternative to chemical resolution with a CRC. It has been widely used for precise and accurate isotopic analysis where two or more isotopes need to be measured without the influence of interfering species. Typically, three options for mass resolving power ($RP_{edge\ 5,95\%}$) are achievable, ranging from low (~300-400) through medium (~4000-9000) to high (≥10000). The state-of-the-art MC-ICP-MS instruments are capable of providing an $RP_{edge\ 5,95\%} \geq 15000$, either by an innovative slit design (for Nu Plasma HR, II, 3, and Nu Sapphire) or by the use of an additional ultra-high-resolution (XHR) unit (for Neptune XT and Neoma MC-ICP-MS). These high-resolution instruments are well suited for the isotopic analyses of Si, Mg, Cl, and K (e.g., Hobin et al., 2021).

The mass resolution of an instrument can be adjusted by varying the slit widths. The Nu Instruments MC-ICP-MS, for example, has three types of slits: the source slit with three width options (0.03, 0.05, and 0.3 mm, Fig. 27A), the two symmetrical alpha slits that can be adjusted continuously from 0-7 mm (Fig. 27B), and three sets of collector slits (0-1 mm) located in front of the low, medium, and high mass collectors (Fig. 27C). For high-precision analysis, the collector slit is usually wider than the ion beam, i.e., the source image (Fig. 27D). During the mass scan, the

entire ion beam is collected and appears as a flat-topped peak, so that slight or transient shifts in the ion image position in the focal plane have a negligible effect on the measured intensity and precision. In contrast, if the beam is as wide as the collector slit, any mass instability would have a significant effect on the registered signal.

In low-resolution mode, all slits are set to their maximum widths. Polyatomic ions may overlap with the peaks of the analytes in the absence of a CRC (Fig. 28A and B). Narrowing the source slit and the collector slit leads to a steeper peak slope and a higher mass resolution (Fig. 27D and 28C-E). The two alpha slits reduce the aberration of a diverging beam by passing a small current through each alpha slit wire, which cuts off the beam from both sides until the beam intensity is halved (Fig. 27(b)). The adjustable collector slit can then be moved to improve the alignment of the analyte peaks and their separation from the interferences (Fig. 27C). As a trade-off for the increased resolution, the sensitivity is reduced by a factor of ~10 in medium resolution and 15-20 in high resolution.

In most applications, polyatomic interferences occur on the high-mass side of the analyte peaks (Fig. 28C). Isotopic measurements can be performed on the low-mass side, where an interference-free, flat-topped section is provided by setting the collector coincidence to block the interfering ions (Fig. 28D). This pseudo-high-resolution mode is preferred over the true high-resolution mode (Fig. 28E) because it provides a wider flat-topped peak shoulder for the analysis. However, interferences can occur on both sides of the analyte ions, especially if the analyte elements have not been chemically separated from the matrix elements prior to isotopic analysis (e.g., in laser ablation applications). For example, $^{48}Ca^{2+}$ occurs on the low-mass side of the Mg isotope peaks, while $^{12}C^{14}N^{+}$, $^{12}C_2{}^{1}H_2{}^{+}$, $^{12}C^{13}C^{+}$, and $^{12}C_2{}^{+}$ occur on the high-mass side. In this case, the true high-

resolution mode is necessary as it allows complete separation of the interferences from the analyte peaks without further reducing the beam sensitivity (Fig. 28E and F).

To achieve high resolution with improved ion transmission, Nu Instruments introduced a large-geometry double-focusing MC-ICP-MS, i.e., the Nu Plasma 1700, in 1999. It features a substantially wider mass dispersion of ~1700 mm compared to conventional MC-ICP-MS (~500 mm), achieved by combining a 943 mm radius, 70° sector electrostatic analyzer with a 750 mm radius, 70° laminated magnet. The large geometry offers a high base resolution of > 800 (10% valley definition), which is sufficient for analyzing approximately 40% of the isotopes at 100% ion transmission. The flat-topped peak, which is critical for isotopic ratio analysis, can be maintained at a 10% valley resolution of > 5000 (e.g., Fig. 28F). Additional features of this instrument include a continuously adjustable source entrance slit and independent collector slits that allow variable resolutions to be set for individual collectors. These features lead to a wide range of selectable $RP_{edge\ 5,95\%}$ from 5000 to 30000. For a given resolving power, the Nu Plasma 1700 has considerably higher transmission than a conventional MC-ICP-MS. A major limitation of this instrument is being unable to resolve $^{36}Ar^+$, $^{40}Ar^+$, and Ar_2^+ from $^{36}S^+$, $^{40}Ca^+$ and $^{80}Se^+$, respectively. This limitation motivated the invention of the *Nu* Sapphire 1700 CRC-MC-ICP-MS.

6 Instrumental isotope fractionation

An inherent issue with ICP-MS analysis is mass-dependent ion transmission efficiency, resulting in preferential extraction and transmission of heavier ions through the interface and ion optic system. This instrumental mass bias poses a particular challenge for isotope ratio measurements. The magnitude of this bias varies with the analyte mass, ranging from <1%/amu for heavy elements (e.g., Hf, Tl, Pb, and U) to ~20 %/amu for light elements such as Li and B (Fig.

29). To obtain accurate isotopic ratios, it is crucial to correct the instrumental isotope fractionation appropriately. The two general correction methods for stable isotope ratio measurements are double spike and standard-sample bracketing (with or without element doping). Comprehensive reviews of different correction methods can be found in the literature (e.g., Albarède et al., 2004; Yang 2009; Albarède et al., 2015; Yang et al., 2018; Klaver and Coath 2019), and brief descriptions are provided below.

6.1 Double-spike approach

The most robust correction is the isotope mixture approach and its derivative, the double-spike method, whereby the sample solution is mixed with a double-spike solution enriched in two isotopes relative to their natural abundances (Nier 1950; Dodson 1963; Rudge et al., 2009). If the spike is added during sample digestion, the isotope fractionation generated during sample preparation, chromatographic purification, and instrumental analyses are all corrected by assuming an identical fractionation being passed onto the double-spike. In cases where the isotope ratio of an unknown sample can be related to that of the reference standard by a mass fractionation factor α:

$$R_{sample}^{\square} = R_{standard}^{\square} \cdot \left(\frac{m_j}{m_i}\right)^{\alpha}$$

where m_i and m_j are masses of the denominator and numerator isotopes, respectively, the isotopic ratio of a spiked sample solution can be solved from the mixing equation:

$$R_{mixture} = \frac{R_{double-spike} \times q + R_{sample} \times C \times (1-q)}{q + C \times (1-q)}$$

where C represents the relative isotopic abundance of the denominator isotope in the sample to that in the double-spike, and q quantifies the mole fraction of double spike in the mixture.

Assuming that instrumental isotope fractionation follows the exponential law with a fractionation factor of β:

$$R_{mixture} = r_{mixture} \times \left(\frac{m_j}{m_i}\right)^{\beta}$$

the three equations are combined to the equation below:

$$f(q, \alpha, \beta) = R_{double\ spike} \times q + R_{standard} \times \left(\frac{m_j}{m_i}\right)^{\alpha} \times C \times (1 - q) - r_{mixture} \times \left(\frac{m_j}{m_i}\right)^{\beta} \times [q + C \times (1 - q)]=0$$

The instrumental mass bias (β) can be solved along with the isotope fractionation of a sample relative to a reference standard (α) and the mole fraction of double spike in the mixture (q) by inverting the three mixing equations using three independent isotope ratios.

The double-spike approach has the advantage of providing both high-precision isotope ratios and elemental abundances. In addition, it does not require strict 100% recovery of the target element from chromatographic separation; therefore, it is preferred for elements (especially trace elements) that are difficult to completely isolate from the sample matrix without sacrificing the chemical yields, such as Ni (e.g., Gueguen et al., 2013), Mo (e.g., Siebert et al., 2001; Anbar 2004), Cr (e.g., Schoenberg et al., 2008), Zr (e.g., Inglis et al., 2018), and Ti (e.g., Millet and Dauphas 2014), or for elements susceptible to evaporative loss during sample preparation, such as Sn (e.g., Creech et al., 2017; Wang et al., 2018; She et al., 2023). Accurate and precise isotopic determination with the double-spike approach relies on a well-calibrated double-spike composition and an optimal spike proportion in the spike-sample mixture. Furthermore, it requires the analyte element to have four or more stable isotopes. An exceptional case is that with a critical double-spike composition and an optimal q, the mixing equations are insensitive to β, so that it can be estimated by analyzing a reference standard. This critical mixing double-spike approach can be

applied to elements with three isotopes, such as Mg, Si, and K (Hofmann 1971; Bizzarro et al., 2011; Coath et al., 2017; He et al., 2022). Special attention must be paid to double-spike data reduction for extraterrestrial samples with isotope anomalies because they do not follow mass-dependent fractionation (Hu and Dauphas, 2017).

6.2 Standard-sample bracketing approach

Standard-sample bracketing, in which standards and samples are measured sequentially, is a generally applicable approach for correcting instrumental isotope fractionation in MC-ICP-MS analysis if the analytes are fully recovered from the column with a clean separation (e.g., Halicz et al., 1999; Tomascak et al., 1999; Belshaw et al., 2000; Galy et al., 2001). This approach takes advantage of the fast sample analyses and the relatively stable instrumental isotope fractionation in MC-ICP-MS, as sample solutions are continuously aspirated into the ionization source. The two essential assumptions for using the standard-sample bracketing correction are (1) a linear drift of the instrumental isotope fractionation over a short period and (2) an identical instrumental isotope fractionation for the sample as for the standard. Accordingly, the instrumental fractionation is corrected by normalizing the isotopic ratio of the sample to the average of the two adjacent bracketing standards. The isotopic ratio of an unknown sample is expressed as per mil (‰) deviation from the bracketing standard:

$$\delta_{sample}\ (‰) = \left(\frac{R_{sample}}{0.5R_{standard1} + 0.5R_{standard2}} - 1\right) \times 1000$$

The delta value of each bracketing standard can be calculated from the two neighboring bracketing standards in a similar way:

$$\delta_{standard\_n}(‰) = \left(\frac{R_{standard\_n}}{0.5R_{standard\_n-1} + 0.5R_{standard\_n+1}} - 1\right) \times 1000$$

1481 This calculation describes instrumental stability based on the reproducibility of the delta values
1482 calculated for all bracketing standards measured during an analytical session. Since the number of
1483 measurements on bracketing standards is significantly larger than the number of repeat
1484 measurements on a given sample, the two standard deviation (2SD) of $\delta_{standards}$ provides a more
1485 conservative error estimate than that based on limited numbers of sample analyses (Dauphas et al.,
1486 2009; Teng et al., 2015).

1487 The application of standard-sample bracketing requires neither the choice of a specific law to
1488 describe instrumental mass fractionation nor *a priori* of the true isotopic ratio of the bracketing
1489 standard. Nevertheless, this method does not correct for artifacts due to the presence of matrix
1490 elements or other differences between the samples and the bracketing standards. Therefore,
1491 accurate and precise isotopic determination requires a high degree of elemental purification and
1492 matching of the analyte concentration and acid molarity between samples and bracketing standards
1493 (e.g., Hu and Teng 2019).

1494 The bracketing standard and sample solutions can be doped with an element of similar mass
1495 and a known isotopic ratio to potentially correct for the non-linear drift of instrumental mass
1496 fractionation and to mitigate matrix effects. Many studies have followed the original work of
1497 Longerich et al. (1987) and assume that elements with similar masses have a similar instrumental
1498 isotopic fractionation coefficient (β) in MC-ICP-MS. As an example, Ni-doping can be used in Fe
1499 isotope analysis, assuming that

1500 $$\beta_{Ni} = ln\left[\frac{(^{62}Ni/^{60}Ni)_{measured}}{(^{62}Ni/^{60}Ni)_{reference}}\right] / \ln\left(\frac{M_{62Ni}}{M_{60Ni}}\right)$$

1501 then

1502 $$\left({}^{56}Fe/{}^{54}Fe\right)_{corrected} = \left(\frac{{}^{56}Fe}{{}^{54}Fe}\right)_{measured} \left(\frac{M_{56Fe}}{M_{54Fe}}\right)^{\frac{ln\left[(62Ni/60Ni)_{reference}/(62Ni/60Ni)_{measured}\right]}{\ln\left(M62Ni/M60Ni\right)}}$$

1503 The corrected ratios are used to calculate the delta values of the samples. However, Maréchal
1504 et al. (1999) demonstrated that for Cu and Zn, β_{Cu} and β_{Zn} could differ by 10%, while their ratio
1505 remain constant during an analytical session. Therefore, Maréchal et al. (1999) suggested
1506 calculating the β_{Cu}/β_{Zn} ratio from the slope of the linear regression between drifts in ln(^{65}Cu/^{63}Cu)
1507 and ln(^{68}Zn/^{64}Zn) of an admixed Zn standard solution [slope = β_{Cu}/β_{Zn} ×
1508 ln(M_{65Cu}/M_{63Cu})]/ln(M_{68Zn}/M_{64Zn}), and applying this relationship to calculate the Cu isotopic
1509 difference between the sample and the standard (and vice versa for Zn isotopic analyses).
1510

1511 # 7 Concluding remarks and future directions

1512 Mass spectrometry has progressed to achieve accurate analysis of isotope abundances and
1513 ratios with higher precision using smaller samples, owing to upgraded introduction systems,
1514 interface designs, ion lenses, and vacuum and detection systems. The development of Hf and W
1515 isotopic measurements using MC-ICP-MS has transformed the field of geochronology (e.g.,
1516 Vervoort et al., 1996; Blichert-Toft and Albarède 1997; Albarède et al., 2000; Kleine et al., 2002;
1517 Yin et al., 2002). The instrumental improvements have also led to the ability to resolve isotopic
1518 variations of transition metals and heavy elements that were previously limited by analytical
1519 uncertainties. For example, nucleosynthetic isotope anomalies have been detected in meteorites
1520 for a growing number of elements, revealing the compositional heterogeneity across the Solar
1521 System at various scales (e.g., Trinquier et al., 2009; Zhang et al., 2012; Dauphas 2017; Schiller
1522 et al., 2018; Kleine et al., 2020; Kruijer et al., 2020; Schiller et al., 2020; Hopp et al., 2022; Onyett
1523 et al., 2023). In particular, as initially suggested by Savage et al. (2014), the recent identification

of nucleosynthetic isotope anomalies of moderately volatile Zn provides unequivocal evidence for the contribution of both carbonaceous and non-carbonaceous materials to Earth's volatile inventory (Paquet et al., 2022; Savage et al., 2022; Steller et al., 2022; Martins et al., 2023). The stable isotope fractionations of moderately volatile elements and refractory elements have also contributed significantly to our understanding of the sources and formation processes from chondrules to terrestrial bodies (e.g., Luck et al., 2003; Luck et al., 2005; Luais 2007; Wombacher et al., 2008; Day and Moynier 2014; Kato et al., 2015; Wang and Jacobsen 2016; Kato and Moynier 2017; Pringle et al., 2017; Nie and Dauphas 2019; van Kooten and Moynier 2019; Hellmann et al., 2020; Ku and Jacobsen 2020; Hu et al., 2021; Nie et al., 2021; Tian et al., 2021; Wang et al., 2021; Hu et al., 2022; 2023; Koefoed et al., 2023; Nie et al., 2023; Paquet et al., 2023; Wang et al., 2024).

Metal stable isotopic variations in terrestrial rocks have been used to trace major episodes of geologic activity throughout Earth's history, including variations in oxygen levels in the atmosphere and oceans (e.g., Pogge von Strandmann et al., 2015; Stüeken et al., 2015; Chi Fru et al., 2016; Zhang et al., 2018; Ostrander et al., 2019), the intensity of forward and reverse weathering of silicates and its influence on long-term climate cycle (e.g., Pogge von Strandmann et al., 2021; Cao et al., 2022), the linkage between extreme paleoenvironments and mass extinctions (e.g., Payne et al., 2010; Huang et al., 2016; Liu et al., 2017; Zhang et al., 2021; Shen et al., 2022), the process and timing of subduction initiation, as well as the nature and mechanism of Archean continental crust formation (e.g., André et al., 2019; Deng et al., 2019; Antonelli et al., 2021; Huang et al., 2022; Deng et al., 2023; Tian et al., 2023), the cycling of surface materials (including carbon) to the sub-arc and deep mantle (e.g., Elliott et al., 2006; Beunon et al., 2020; Banerjee et al., 2021; Huang and Jacobsen 2021; Debret et al., 2022; Liu et al., 2022; Zhang et al., 2022). There is also a growing interest in using metal stable isotopes in the fields of environmental

science (e.g., Cloquet et al., 2008; Weiss et al., 2008; Yin et al., 2010; Blum et al., 2014; Wiederhold 2015; Schilling et al., 2021; Balaram et al., 2022; Basu et al., 2022; Johnson et al., 2022; Sullivan et al., 2022; Qu and Han 2023), ecology and bioarchaeology (e.g., Jaouen and Pons 2017; Martin et al., 2017; Hassler et al., 2018; Stephens et al., 2021; Martin et al., 2022), and bio-medical science (e.g., von Blanckenburg et al., 2009; Balter et al., 2013; Moynier et al., 2013; Balter et al., 2015; Albarède et al., 2017; Moynier et al., 2017; Costas-Rodríguez et al., 2019; Mahan et al., 2020; Moynier et al., 2020; Tacail et al., 2020; Schilling et al., 2021; Hill Gallant and Zheng 2022; Morel et al., 2022; Schilling et al., 2022; Sullivan et al., 2023).

More recently, CRC-MC-ICP-MS has shown great promise in removing Ar-related interferences, which enables the measurement of K, Ca, and Fe isotope ratios without resorting to the pseudo-high-resolution mode that leads to a substantial sensitivity loss. Another advantage of the CRC-MC-ICP-MS is that ^{40}Ca is directly measurable, with limited isobaric interference from ^{40}Ar. These improvements provide the opportunity to further investigate the Ca isotopic composition of the bulk Solar System and terrestrial bodies (e.g., Klaver et al., 2021; Eriksen and Jacobsen 2022; Fu et al., 2022; Moynier et al., 2022; Fu et al., 2023), to apply ^{40}K-^{40}Ca dating (Dai et al., 2023), to identify the presence of short-lived ^{41}Ca as ^{41}K excess in chondritic components (Ku et al., 2022), and to explore biological applications of metal isotopes (e.g., Moynier et al., 2021; Higgins et al., 2022; Mahan et al., 2022; Télouk et al., 2022; Cui et al., 2023a; b). In addition, the mass-shift mode of CRC has been successfully applied to in situ Rb-Sr dating (Bevan et al., 2021; Dauphas et al., 2022). The potential of CRC-MC-ICP-MS is far from fully realized. With significantly improved sensitivity, the isotopic ratios of many elements can be analyzed with minimal sample consumption. Future studies could be targeted at detecting small-scale isotopic variations, such as in minerals and their inclusions, experimental products, and mission return

samples (e.g., Moynier et al., 2022; Hu et al., 2024), at coupling a laser ablation system to the CRC-MC-ICP-MS (e.g., Bevan et al., 2021; Dauphas et al., 2022), or at investigating ion-chemistry with various gases and extending the CRC techniques to other isotope systems that are plagued by polyatomic interferences (e.g., Se and Si).

Another direction for future exploration is the development of ICP using an alternative plasma gas to increase the ionization efficiency and to reduce polyatomic interferences. For example, many limitations of argon plasma could be overcome by using helium plasma (Abdallah and Mermet 1982; Robin et al., 1982; Chan and Montaser 1985; Chan et al., 1986; Montaser et al., 1987); because helium consists primarily of ^{4}He (natural abundance 99.9998%), which has an extremely low m/z ratio of 4. Furthermore, helium has a considerably higher ionization energy (24.6 eV) than argon; therefore, helium plasma is expected to enhance the ionization efficiency of elements. The analytical performance of neon plasma has also been investigated using laser ablation (LA)-ICP-MS to analyze solid materials, where Ar-related interferences are reduced (Petibon et al., 2002). It is worth noting that commercial instruments are optimized for argon plasma. Using an alternative plasma gas may require a major adjustment in the RF generator's matching circuits, forward power, torch configuration, and pumping capacity in the interface.

Since W. Wien observed the deflection of positively charged particles in a magnetic field and J. J. Thomson’s discovery of isotopes a century ago, mass spectrometry has evolved from a technique for studying atomic structures into an essential tool for molecular, elemental, and isotopic ratio analyses. The development of self-sustaining, atmospheric ICP with an aqueous sample introduction system has facilitated multi-element analysis with unprecedented flexibility, detection limits, and sample throughput. The coupling of ICP with a quadrupole mass analyzer has made ICP-MS a worldwide popular analytical technique. The integration of double-focusing

magnetic sector MS with a multi-collector detection system (MC-ICP-MS) has further revolutionized the field, enabling accurate and precise isotopic analysis of metals and metalloids across the Periodic Table. The utilization of collision/reaction cell technology on modern MC-ICP-MS has offered a novel approach to removing spectral interferences. Future endeavors to improve interface design and reduce space charge effects will allow the potential of ICP-MS to be better exploited. The constant pursuit of higher mass resolution and analytical precision, accuracy, and sensitivity will continue to push the analytical boundaries of ICP-MS, fueling interdisciplinary research in the broad fields of cosmochemistry, geosciences, environmental sciences, and biological and medical sciences.

Acknowledgments

We are thankful for the detailed and constructive comments from Klaus Mezger that significantly improved the manuscript and for Editor Anat Shahar's efficient handling of the paper. Detailed comments from Ye Zhao and Ronald Sletten are greatly appreciated. We thank Lloyd Nicolas, Daniel Peters, Zhaofeng Zhang, Xin-Yang Chen, Shui-Jiong Wang, Jia-Xin She, Jian-Feng Liu, and Xiao-Quan Qin for providing technical details. F.M. acknowledges funding from the ERC under the European Community's H2020 framework program/ERC grant agreements No. 101001282 (METAL) and No. 101081580 (DAI). This work was partly supported by the IPGP multidisciplinary program PARI, by Region île-de-France SESAME Grants no. 12015908, EX047016, and the IdEx Université de Paris grant, ANR-18-IDEX-0001, and the DIM ACAV+.

Figure captions

Fig. 1. Argon ICP as an efficient ionization source. (A) Ionization energy (eV) of elements as a function of their atomic mass. (B) Degree (%) of ionization of elements as a function of their ionization energy, adapted from the calculated results by Houk (1986) based on Saha Equation at an ionization temperature (T_{ion}) of 7500 K with an electron density (n_e) of $1 \times 10^{15}/cm^3$. Argon efficiently ionizes most elements except for non-metals, metalloids, and certain metals (e.g., Hg), which are indicated by the red circles and labels. While most elements form singly charged positive ions, alkali earth and rare earth elements may form doubly charged ions because their second ionization energies are lower than the first ionization energy of argon.

Fig. 2. Main components of double-focusing ICP-MS equipped with a multi-collector detection system.

Fig. 3. Typical types of nebulizers used for sample introduction into the ICP-MS. (A) Concentric nebulizers; (B) Crossflow nebulizers; (C) Nebulizer transport efficiency as a function of sample uptake rate. Source: (A) and (C) are reproduced with permission from Glass Expansion, and (B) is modified from Olesik (2014) with permission from Elsevier.

Fig. 4. Typical types of spray chambers used for condensing large droplets (> 10 μm) produced by nebulizers. (A) A baffled cyclonic spray chamber; (B) A dual Scott/cyclonic spray chamber. Reused with permission from Glass Expansion.

Fig. 5. Examples of commercially available desolvation systems. (A) CETAC Aridus 3 uses a heated spray chamber with a microporous membrane to remove solvent vapors. (B) Elemental Scientific Inc. (ESI) Apex combines a heated spray chamber with a cold condenser and a heated membrane desolvator to remove solvent vapors. Reused with permission from Teledyne LABS for (A) and ESI for (B).

Fig. 6. Sensitivity enhancement for elements between Li and U using "dry" plasma (Apex desolvating nebulizer system) and direct injection nebulization (d-DIHEN) relative to "wet" plasma using stable introduction system (SIS: dual Scott⁄cyclonic spray chamber). Adapted from Louvat et al. (2011) with permission from John Wiley and Sons.

Fig. 7. (A) Illustration of a glass ICP torch and (B) Torch box configuration.

Fig. 8. Interface design for ICP-MS. (A) Differential pressure levels in ICP-MS across its main components, from the ICP at atmospheric pressure to the high-vacuum mass analyzer region. A high vacuum is required for ions to have a long mean free path to travel through the mass spectrometer and reach the detector. The relationship between mean free path and pressure is

plotted based on data reported on the Pfeiffer Vacuum website for nitrogen at 273.15 K. The horizontal axis of the plot is in reverse order (decreasing pressure). (B) An illustration of ion extraction from the interface region. Modified from Olesik (2014) and Campargue (1984), with permission from Elsevier and the American Chemical Society, respectively. The small gray insert shows an older interface design using a much smaller sampling orifice, which is characterized by a thicker boundary layer and electron-poor sheath. Adapted from Niu and Houk (1996) with permission from Elsevier.

Fig. 9. Schematic illustration of zoom lenses used on *Nu* Instruments MC-ICP-MS for adjusting the mass dispersion of isotopes of interest. (A) Quad lenses increase the dispersion for U isotopes. (B) Sr isotopes separated by the natural dispersion of the magnet. (C) Sr isotopes with the correct spacing produced by the Quad lenses. Reproduced with permission from Nu Instruments Ltd.

Fig. 10. Three commonly used definitions of resolution in mass spectrometry: (A) 10% valley definition; (B) peak width definition; (C) peak edge definition.

Fig. 11. An electrostatic analyzer brings diverging ions of identical kinetic energy into focus and disperses incoming ions according to their kinetic energies. Ions having a higher kinetic energy (E_{K2}) are deflected less relative to those with a lower kinetic energy (E_{K1}).

Fig. 12. Ion deflection in a static magnetic field. (A) Circular trajectory of a moving ion in a magnetic field. (B) Angular focusing of ions with identical kinetic energy in a perpendicular magnetic field (shown in light blue). (C) Mass dispersion of a 180º magnetic field at the focal plane.

Fig. 13. The application of crossed electric and magnetic fields as a velocity selector ("Wien filter") in the mass spectrometer.

Fig. 14. Simplified illustration of the two commonly used configurations for double-focusing: (A) Mattauch-Herzog geometry; (B) Forward Nier-Johnson geometry. Adapted from Jakubowski et al., (2011) with permission from the Royal Society of Chemistry.

Fig. 15. Schematic representation of a quadrupole mass analyzer. One pair of electrodes serve as the low-mass filter and the other pair serve as the high-mass filter. The two electrode pairs result in a narrow bandpass of approximately 1 amu. Adapted from Miller and Denton (1986) and Vanhaecke and Degryse (2012) with permission from the American Chemical Society and John Wiley and Sons, respectively.

Fig. 16. Illustration of Mathieu stability diagram for a quadrupole ICP-MS. At a lower U/V ratio (a shallower slope scan line), the mass resolution is reduced while ion transmission is increased.

Adapted from Clases (2023) with permission from the Royal Society of Chemistry under CC-BY 3.0 license.

Fig. 17. Schematic representation of an orthogonal-acceleration time-of-flight mass spectrometer (TOF MS) coupled to a quadrupole ICP. Adding a reflector improves the mass resolution; different travel distances in the reflector compensate for the kinetic energy distribution of ions with the same m/z ratio. Adapted from Hendriks et al. (2017) with permission from the Royal Society of Chemistry.

Fig. 18. Schematic illustrations of common ion detectors used in ICP-MS, with the Faraday cup on the left and ion multipliers on the right. The illustration(s) for the Faraday cup and electron multiplier are adapted from Wiedenbeck et al., (2012) with permission from John Wiley and Sons, for the Daly detector is adapted from Daly (1960) with permission from AIP Publishing, and for the multi-collector arrangement is reproduced with permission from Nu Instruments Ltd.

Fig. 19. Dynamic range of different detector types. The recommended detector(s) available for a given signal intensity are indicated by the intensity of shading. The counting statistic limit on precision for a 10-minute acquisition is shown at the top, with the typical limit for each detector type on the right. Provided by Thermo Fisher and reused with permission.

Fig. 20. An illustration of using cold plasma to effectively reduce Ar-related interferences for Fe isotopic analysis. Mass scans in (A) and (B) were performed in medium mass resolution ($m/\Delta m = 4500$) using "wet" plasma introduction at different RF powers. Compared with (A) hot plasma conditions (1260 W), the interferences of $^{40}Ar^{16}O^{+}$ (on $^{56}Fe^{+}$) and $^{40}Ar^{14}N^{+}$ (on $^{54}Fe^{+}$) become negligible under (B) cold plasma conditions (600 W), allowing $^{56}Fe/^{54}Fe$ ratios to be measured precisely in low mass resolution mode ($m/\Delta m \sim 300$). However, a small amount of $^{40}Ar^{16}O^{1}H^{+}$ persists, and interferes with the minor isotope of ^{57}Fe. Reproduced from Chernonozhkin et al. (2017) with permission from the Royal Society of Chemistry.

Fig. 21. A comparison of the potential well (upper panel) and ion stability regions (blue field in the lower panel) between a quadrupole, a hexapole, and an octopole. Adapted and modified from Marchante-Gayón et al. (2003) with permission from the Royal Society of Chemistry.

Fig. 22. Principles of kinetic energy discrimination in a collision cell. A narrower ion energy distribution leads to a better separation between the analyte ions and the polyatomic interferences. Reproduced with permission from Thermo Fisher.

Fig. 23. Schematic representation of four different modes of CRC operation. (A) Collision mode: a buffer gas is added to the cell to filter out the slightly more massive polyatomic ions based on kinetic energy discrimination. (B) On-mass reaction mode: charge exchange reactions with H_2

remove $^{40}Ar^+$ and ArH^+ interferences, freeing m/z of 39, 40, and 41 for K isotope measurements. (C) Conventional mass-shift mode: $^{75}As^+$ is oxidized to $^{75}As^{16}O^+$ and measured at m/z = 91, which overlaps with the isobaric interference of $^{91}Zr^+$. (D) Mass-shift mode with pre-cell mass filtering: the first quadrupole admits only ions at m/z = 75 to the cell while those with other m/z values (e.g., $^{91}Zr^+$) are rejected. $^{75}As^+$ is then converted to $^{75}As^{16}O^+$ by O_2 and measured at m/z = 91. Adapted and modified from Balcaen et al. (2015) with permission from Elsevier.

Fig. 24. Chemical reactions to remove isobaric interferences via (A) electron transfer and (B) oxygen atom transfer with various gases. In (A), atomic ions are labeled in black color, and their oxides and chlorides are shown in blue and green color, respectively. If the first ionization energy (indicated on the y-axis) of an interfering species is higher than the reaction gas (indicated by the dashed lines), it is thermodynamically favorable to neutralize the interfering ions by electron transfer from the gas. In (B), atomic ions of analytical interest are shown as solid circles and interferences (argon, argide, oxide, and hydroxide) are shown as open circles. The horizontal dashed lines represent oxygen atom affinities of gases with one less oxygen than their indicated forms. If an ion has an oxygen-atom affinity (shown on the y-axis) above a dashed line, it is thermodynamically favorable to incorporate an oxygen atom from the corresponding gas. Ion oxides with oxygen-atom affinities lower than the dashed line readily give up an oxygen atom to the corresponding neutral, which has one less oxygen atom than the indicated gas. Adapted from Koyanagi et al. (2005) and Tanner et al., (2002), with permissions from John Wiley and Sons and Elsevier, respectively.

Fig 25. Schematic representation of the dual-path design of *Nu* Sapphire CRC-MC-ICP-MS. The application of the Conventional Mode, as illustrated by K isotopic analysis (Hu et al., 2018), is compared with the use of Collision/Reaction Cell (CRC) Mode to remove Ar-based interferences for K and Ca isotopic measurements. Modified from figures provided by Nu Instruments Ltd with permission.

Fig. 26. Schematic representations of CRC-MC-ICP-MS built on Thermo Fisher Scientific platforms with a pre-cell mass filter. (A) Proteus; (B) Vienna; (C) Neoma. Neoma is commercially available, while Proteus and Vienna are prototypes. (A) and (B) are from Craig et al. (2021) with permission from American Chemical Society under CC-BY 4.0 license, and (C) is adapted from Dauphas et al. (2022) with permission from the Royal Society of Chemistry under CC-BY 3.0 license.

Fig. 27. Three types of slits and their respective locations on a *Nu* Instruments MC-ICP-MS for mass resolution adjustment. (A) Source slit (0.03 mm, 0.05 mm, and 0.3 mm); (B) Alpha slits (0-7 mm); (C) Collector slits (0-1 mm); (D) Registered peak shape after two spatially resolved beams (with dispersion D and width b) swept across a Faraday cup (with collector slit width W_C). Modified from figures provided by Nu Instruments Ltd with permission.

Fig. 28. Different mass resolution modes used in MC-ICP-MS. (A) In low-resolution mode, a collision/reaction cell provides interference-free flat-topped peaks for Fe isotopes. (B) Without a collision/reaction cell, the polyatomic interferences overlap with the Fe isotope peaks in low-resolution mode. (C) and (D) In pseudo-high-resolution mode, Fe isotope peaks are partially resolved from the polyatomic interferences, providing an interference-free peak shoulder for isotope ratio analyses. (E) and (F) In true high-resolution mode, Fe isotope peaks are fully separated from the polyatomic interferences. The large-geometry Nu Plasma 1700 provides wider flat-topped peaks than the standard MC-ICP-MS. Modified from figures provided by Nu Instruments Ltd with permission.

Fig. 29. Instrumental mass bias (% per amu) for elements over the mass range from Li to U in MC-ICP-MS. The extent of the bias for an element depends primarily on its mass.

References

Aarons, S. M., J. R. Reimink, N. D. Greber, A. W. Heard, Z. Zhang and N. Dauphas (2020). Titanium isotopes constrain a magmatic transition at the Hadean-Archean boundary in the Acasta Gneiss Complex. *Science Advances* **6**: eabc9959.

Abdallah, M. H. and J. M. Mermet (1982). Comparison of temperature measurements in ICP and MIP with Ar and He as plasma gas. *Spectrochimica Acta Part B: Atomic Spectroscopy* **37**: 391-397.

Aggarwal, J. K., D. Sheppard, K. Mezger and E. Pernicka (2003). Precise and accurate determination of boron isotope ratios by multiple collector ICP-MS: origin of boron in the Ngawha geothermal system, New Zealand. *Chemical Geology* **199**: 331-342.

Albarède, F., E. Albalat and P. Télouk (2015). Instrumental isotope fractionation in multiple-collector icp-ms. *Journal of Analytical Atomic Spectrometry* **30**: 1736-1742.

Albarède, F. and B. Beard (2004). Analytical methods for non-traditional isotopes. *Reviews in mineralogy and geochemistry* **55**: 113-152.

Albarède, F., J. Blichert-Toft, J. D. Vervoort, J. D. Gleason and M. Rosing (2000). Hf–Nd isotope evidence for a transient dynamic regime in the early terrestrial mantle. *Nature* **404**: 488-490.

Albarède, F., P. Télouk and V. Balter (2017). Medical applications of isotope metallomics. *Reviews in Mineralogy and Geochemistry* **82**: 851-885.

Albarède, F., P. Telouk, J. Blichert-Toft, M. Boyet, A. Agranier and B. Nelson (2004). Precise and accurate isotopic measurements using multiple-collector ICPMS1 1Associate editor: Y. Amelin. *Geochimica et Cosmochimica Acta* **68**: 2725-2744.

An, S., J. Chen, S. Boschi and W. Li (2023). Significantly enhanced robustness of K isotope analysis by collision cell MC-ICP-MS and its application to the returned lunar samples by China's Chang'e-5 Project. *Analytical Chemistry* **95**: 2140-2145.

Anbar, A. D. (2004). Molybdenum stable isotopes: observations, interpretations and directions. *Reviews in Mineralogy and Geochemistry* **55**: 429-454.

Anbar, A. D., K. A. Knab and J. Barling (2001). Precise determination of mass-dependent variations in the isotopic composition of molybdenum using MC-ICPMS. *Analytical Chemistry* **73**: 1425-1431.

André, L., K. Abraham, A. Hofmann, L. Monin, I. C. Kleinhanns and S. Foley (2019). Early continental crust generated by reworking of basalts variably silicified by seawater. *Nature Geoscience* **12**: 769-773.

Antonelli, M. A., J. Kendrick, C. Yakymchuk, M. Guitreau, T. Mittal and F. Moynier (2021). Calcium isotope evidence for early Archaean carbonates and subduction of oceanic crust. *Nature Communications* **12**: 2534.

Arnold, T., J. N. Harvey and D. J. Weiss (2008). An experimental and theoretical investigation into the use of H_2 for the simultaneous removal of ArO^+ and $ArOH^+$ isobaric interferences during Fe isotope ratio analysis with collision cell based Multi-Collector Inductively Coupled Plasma Mass Spectrometry. *Spectrochimica Acta Part B: Atomic Spectroscopy* **63**: 666-672.

Aston, F. W. (1919). LXXIV. A positive ray spectrograph. *The London, Edinburgh, and Dublin Philosophical Magazine and Journal of Science* **38**: 707-714.

Aston, F. W. (1927). Bakerian Lecture — A new mass-spectrograph and the whole number rule. *Proceedings of the Royal Society of London. Series A, Containing Papers of a Mathematical and Physical Character* **115**: 487-514.

Aston, F. W. (1937). A second-order focusing mass spectrograph and isotopic weights by the doublet method. *Proceedings of the Royal Society of London. Series A - Mathematical and Physical Sciences* **163**: 391-404.

Babat, G. I. (1947). Electrodeless discharges and some allied problems. *Journal of the Institution of Electrical Engineers-Part III: Radio and Communication Engineering* **94**: 27-37.

Bainbridge, K. T. (1932). A mass-spectrograph. Minutes of Cambridge Meeting February 25-27, 1932, Physical Review. **40:** 130.

Bainbridge, K. T. (1933). The Equivalence of Mass and Energy. *Physical Review* **44**: 123-123.

Bainbridge, K. T. (1933). The Masses of the Lithium Isotopes. *Physical Review* **44**: 56-57.

Balaram, V., W. Rahaman and P. Roy (2022). Recent advances in MC-ICP-MS applications in Earth and environmental sciences: challenges and solutions. *Geosystems and Geoenvironment* **1**: 100019.

Balcaen, L., E. Bolea-Fernandez, M. Resano and F. Vanhaecke (2015). Inductively coupled plasma – Tandem mass spectrometry (ICP-MS/MS): a powerful and universal tool for the interference-free determination of (ultra)trace elements – A tutorial review. *Analytica Chimica Acta* **894**: 7-19.

Balliana, E., M. Aramendía, M. Resano, C. Barbante and F. Vanhaecke (2013). Copper and tin isotopic analysis of ancient bronzes for archaeological investigation: development and validation of a suitable analytical methodology. *Analytical and Bioanalytical Chemistry* **405**: 2973-2986.

Balter, V., A. Lamboux, A. Zazzo, P. Télouk, Y. Leverrier, J. Marvel, A. P. Moloney, F. J. Monahan, O. Schmidt and F. Albarède (2013). Contrasting Cu, Fe, and Zn isotopic patterns in organs and body fluids of mice and sheep, with emphasis on cellular fractionation. *Metallomics* **5**: 1470-1482.

Balter, V., A. Nogueira da Costa, V. P. Bondanese, K. Jaouen, A. Lamboux, S. Sangrajrang, N. Vincent, F. Fourel, P. Télouk, M. Gigou, C. Lécuyer, P. Srivatanakul, C. Bréchot, F. Albarède and P. Hainaut (2015). Natural variations of copper and sulfur stable isotopes in blood of hepatocellular carcinoma patients. *Proceedings of the National Academy of Sciences* **112**: 982-985.

Bandura, D. R., V. I. Baranov and S. D. Tanner (2002). Detection of Ultratrace Phosphorus and Sulfur by Quadrupole ICPMS with Dynamic Reaction Cell. *Analytical Chemistry* **74**: 1497-1502.

Banerjee, A., R. Chakrabarti and A. Simonetti (2021). Temporal evolution of $\delta^{44/40}$Ca and ^{87}Sr/^{86}Sr of carbonatites: Implications for crustal recycling through time. *Geochimica et Cosmochimica Acta* **307**: 168-191.

Bao, Z., C. Zong, K. Huang, K. Chen, N. Lv and H. Yuan (2019). Determination of Mg isotope ratios without column chromatography for carbonates using sulphuric acid and MC-ICP-MS. *Journal of Analytical Atomic Spectrometry* **34**: 2469-2475.

Barinaga, C. J., D. W. Koppenaal and S. A. McLuckey (1994). Ion-trap mass spectrometry with an inductively coupled plasma source. *Rapid Communications in Mass Spectrometry* **8**: 71-76.

Bartky, W. and A. J. Dempster (1929). Paths of charged particles in electric and magnetic fields. *Physical Review* **33**: 1019-1022.

Basu, A., K. Schilling, A. N. Halliday, N. Wasserman and T. M. Johnson (2022). Te(IV) immobilization by siderite: Reaction kinetics, mechanism, and Te isotopic fractionation. *Chemical Geology* **612**: 121123.

Beauchemin, D. (2020). Sample introduction systems in ICPMS and ICPOES, Newnes.

Becker, E. W. and K. Bier (1954). Die Erzeugung eines intensiven, teilweise monochromatisierten Wasserstoff-Molekularstrahles mit einer Laval-Düse. *Zeitschrift für Naturforschung A* **9**: 975-986.

Becker, H., C. Dalpe and R. J. Walker (2002). High-precision Ru isotopic measurements by multi-collector ICP-MS. *Analyst* **127**: 775-780.

Becker, J. S. (2002). State-of-the-art and progress in precise and accurate isotope ratio measurements by ICP-MS and LA-ICP-MS Plenary Lecture. *Journal of Analytical Atomic Spectrometry* **17**: 1172-1185.

Becker, S. (2008). Inorganic mass spectrometry: principles and applications, John Wiley & Sons.

Belshaw, N. S., P. A. Freedman, R. K. O'Nions, M. Frank and Y. Guo (1998). A new variable dispersion double-focusing plasma mass spectrometer with performance illustrated for Pb isotopes. *International Journal of Mass Spectrometry* **181**: 51-58.

Belshaw, N. S., X. K. Zhu, Y. Guo and R. K. O'Nions (2000). High precision measurement of iron isotopes by plasma source mass spectrometry. *International Journal of Mass Spectrometry* **197**: 191-195.

Beunon, H., N. Mattielli, L. S. Doucet, B. Moine and B. Debret (2020). Mantle heterogeneity through Zn systematics in oceanic basalts: Evidence for a deep carbon cycling. *Earth-Science Reviews* **205**: 103174.

Bevan, D., C. D. Coath, J. Lewis, J. Schwieters, N. Lloyd, G. Craig, H. Wehrs and T. Elliott (2021). In situ Rb–Sr dating by collision cell, multicollection inductively-coupled plasma mass-spectrometry with pre-cell mass-filter, (CC-MC-ICPMS/MS). *Journal of Analytical Atomic Spectrometry* **36**: 917-931.

Bizzarro, M., C. Paton, K. Larsen, M. Schiller, A. Trinquier and D. Ulfbeck (2011). High-precision Mg-isotope measurements of terrestrial and extraterrestrial material by HR-MC-ICPMS—implications for the relative and absolute Mg-isotope composition of the bulk silicate Earth. *Journal of Analytical Atomic Spectrometry* **26**: 565-577.

Blichert-Toft, J. and F. Albarède (1997). The Lu-Hf isotope geochemistry of chondrites and the evolution of the mantle-crust system. *Earth and Planetary Science Letters* **148**: 243-258.

Blichert-Toft, J., C. Chauvel and F. Albarède (1997). Separation of Hf and Lu for high-precision isotope analysis of rock samples by magnetic sector-multiple collector ICP-MS. *Contributions to Mineralogy and Petrology* **127**: 248-260.

Blum, J. D., L. S. Sherman and M. W. Johnson (2014). Mercury Isotopes in Earth and Environmental Sciences. *Annual Review of Earth and Planetary Sciences* **42**: 249-269.

Boulyga, S. F. and J. S. Becker (2001). Determination of uranium isotopic composition and 236U content of soil samples and hot particles using inductively coupled plasma mass spectrometry. *Analytical and Bioanalytical Chemistry* **370**: 612-617.

Boumans, P. W. J. M. and F. J. De Boer (1977). An experimental study of a 1-kW, 50-MHz RF inductively coupled plasma with pneumatic nebulizer, and a discussion of experimental evidence for a non-thermal mechanism. *Spectrochimica Acta Part B: Atomic Spectroscopy* **32**: 365-395.

Bradshaw, N., E. F. H. Hall and N. E. Sanderson (1989). Communication. Inductively coupled plasma as an ion source for high-resolution mass spectrometry. *Journal of Analytical Atomic Spectrometry* **4**: 801-803.

Brennecka, G. A., L. E. Borg, S. J. Romaniello, A. K. Souders, Q. R. Shollenberger, N. E. Marks and M. Wadhwa (2017). A renewed search for short-lived ^{126}Sn in the early Solar System: Hydride generation MC-ICPMS for high sensitivity Te isotopic analysis. *Geochimica et Cosmochimica Acta* **201**: 331-344.

Brennecka, G. A., S. Weyer, M. Wadhwa, P. E. Janney, J. Zipfel and A. D. Anbar (2010). ^{238}U/^{235}U variations in meteorites: extant ^{247}Cm and implications for Pb-Pb dating. *Science* **327**: 449-451.

Breton, T., N. S. Lloyd, A. Trinquier, C. Bouman and J. B. Schwieters (2015). Improving Precision and Signal/Noise Ratios for MC-ICP-MS. *Procedia Earth and Planetary Science* **13**: 240-243.

Browner, R. F. and A. W. Boorn (1984). Sample introduction: the Achilles' Heel of atomic spectroscopy? *Analytical Chemistry* **56**: 786A-798A.

Bryant, C. J., M. T. McCulloch and V. C. Bennett (2003). Impact of matrix effects on the accurate measurement of Li isotope ratios by inductively coupled plasma mass spectrometry (MC-ICP-MS) under "cold" plasma conditions. *Journal of Analytical Atomic Spectrometry* **18**: 734-737.

Buckley, W. T., J. J. Budac, D. V. Godfrey and K. M. Koenig (1992). Determination of selenium by inductively coupled plasma mass spectrometry utilizing a new hydride generation sample introduction system. *Analytical Chemistry* **64**: 724-729.

Cameron, A. E. and D. F. Eggers Jr. (1948). An ion "velocitron". *Review of Scientific Instruments* **19**: 605-607.

Campargue, R. (1964). High intensity supersonic molecular beam apparatus. *Review of Scientific Instruments* **35**: 111-112.

Campargue, R. (1984). Progress in overexpanded supersonic jets and skimmed molecular beams in free-jet zones of silence. *The Journal of Physical Chemistry* **88**: 4466-4474.

Cao, C., C. P. Bataille, H. Song, M. R. Saltzman, K. Tierney Cramer, H. Wu, C. Korte, Z. Zhang and X.-M. Liu (2022). Persistent late Permian to Early Triassic warmth linked to enhanced reverse weathering. *Nature Geoscience* **15**: 832-838.

Cardinal, D., L. Y. Alleman, J. de Jong, K. Ziegler and L. André (2003). Isotopic composition of silicon measured by multicollector plasma source mass spectrometry in dry plasma mode. *Journal of Analytical Atomic Spectrometry* **18**: 213-218.

Carlson, R. W. (2014). 15.18 - Thermal Ionization Mass Spectrometry. Treatise on Geochemistry (Second Edition). H. D. Holland and K. K. Turekian. Oxford, Elsevier**:** 337-354.

Chakrabarti, R. and S. B. Jacobsen (2010). Silicon isotopes in the inner Solar System: implications for core formation, solar nebular processes and partial melting. *Geochimica et Cosmochimica Acta* **74**: 6921-6933.

Chambers, D. M., J. Poehlman, P. Yang and G. M. Hieftje (1991). Fundamental studies of the sampling process in an inductively coupled plasma mass spectrometer-I: Langmuir probe measurements. *Spectrochimica Acta Part B: Atomic Spectroscopy* **46**: 741-760.

Chan, S.-K. and A. Montaser (1985). A helium inductively coupled plasma for atomic emission spectrometry. *Spectrochimica Acta Part B: Atomic Spectroscopy* **40**: 1467-1472.

Chan, S. K., R. L. Van Hoven and A. Montaser (1986). Generation of a helium inductively coupled plasma in a low-gas-flow torch. *Analytical Chemistry* **58**: 2342-2343.

Chen, H., N. J. Saunders, M. Jerram and A. N. Halliday (2021). High-precision potassium isotopic measurements by collision cell equipped MC-ICPMS. *Chemical Geology* **578**: 120281.

Chen, J., H. Hintelmann and B. Dimock (2010). Chromatographic pre-concentration of Hg from dilute aqueous solutions for isotopic measurement by MC-ICP-MS. *Journal of Analytical Atomic Spectrometry* **25**: 1402-1409.

Chen, X.-Y., F.-Z. Teng and D. C. Catling (2019). Fast and precise boron isotopic analysis of carbonates and seawater using Nu Plasma II multi-collector inductively coupled plasma mass spectrometry and a simple sample introduction system. *Rapid Communications in Mass Spectrometry* **33**: 1169-1178.

Cheng, H., R. Lawrence Edwards, C.-C. Shen, V. J. Polyak, Y. Asmerom, J. Woodhead, J. Hellstrom, Y. Wang, X. Kong, C. Spötl, X. Wang and E. Calvin Alexander (2013). Improvements in ^{230}Th dating, ^{230}Th and ^{234}U half-life values, and U–Th isotopic measurements by multi-collector inductively coupled plasma mass spectrometry. *Earth and Planetary Science Letters* **371-372**: 82-91.

Cheng, P., G. K. Koyanagi and D. K. Bohme (2008). On the chemical resolution of the $^{87}Rb^{+}$ (s0)/$^{87}Sr^{+}$ (s1) isobaric interference: a kinetic search for an optimum reagent. *Analytica Chimica Acta* **627**: 148-153.

Chernonozhkin, S. M., M. Costas-Rodríguez, P. Claeys and F. Vanhaecke (2017). Evaluation of the use of cold plasma conditions for Fe isotopic analysis via multi-collector ICP-mass spectrometry: effect on spectral interferences and instrumental mass discrimination. *Journal of Analytical Atomic Spectrometry* **32**: 538-547.

Chi Fru, E., N. P. Rodríguez, C. A. Partin, S. V. Lalonde, P. Andersson, D. J. Weiss, A. El Albani, I. Rodushkin and K. O. Konhauser (2016). Cu isotopes in marine black shales record the Great Oxidation Event. *Proceedings of the National Academy of Sciences* **113**: 4941-4946.

Choi, M. S., J.-S. Ryu, S.-W. Lee, H. S. Shin and K.-S. Lee (2012). A revisited method for Mg purification and isotope analysis using cool-plasma MC-ICP-MS. *Journal of Analytical Atomic Spectrometry* **27**: 1955-1959.

Choi, M. S., J.-S. Ryu, H. Y. Park, K.-S. Lee, Y. Kil and H. S. Shin (2013). Precise determination of the lithium isotope ratio in geological samples using MC-ICP-MS with cool plasma. *Journal of Analytical Atomic Spectrometry* **28**: 505-509.

Choot, E. H. and G. Horlic (1986). Vertical spatial emission profiles in Ar-N_2 mixed gas inductively coupled plasmas—I. *Spectrochimica Acta Part B: Atomic Spectroscopy* **41**: 889-906.

Clases, D. (2023). Swimming against the current – sacrificing unit mass resolution in ICP-MS to improve figures of merit. *Journal of Analytical Atomic Spectrometry* **38**: 2518-2527.

Clayton, R., P. Andersson, N. H. Gale, C. Gillis and M. J. Whitehouse (2002). Precise determination of the isotopic composition of Sn using MC-ICP-MS. *Journal of Analytical Atomic Spectrometry* **17**: 1248-1256.

Cloquet, C., J. Carignan, M. F. Lehmann and F. Vanhaecke (2008). Variation in the isotopic composition of zinc in the natural environment and the use of zinc isotopes in biogeosciences: a review. *Analytical and Bioanalytical Chemistry* **390**: 451-463.

Cloquet, C., O. Rouxel, J. Carignan and G. Libourel (2005). Natural Cadmium Isotopic Variations in Eight Geological Reference Materials (NIST SRM 2711, BCR 176, GSS-1, GXR-1, GXR-2, GSD-12, Nod-P-1, Nod-A-1) and Anthropogenic Samples, Measured by MC-ICP-MS. *Geostandards and Geoanalytical Research* **29**: 95-106.

Coath, C. D., T. Elliott and R. C. Hin (2017). Double-spike inversion for three-isotope systems. *Chemical Geology* **451**: 78-89.

Costas-Rodríguez, M., S. Van Campenhout, A. A. M. B. Hastuti, L. Devisscher, H. Van Vlierberghe and F. Vanhaecke (2019). Body distribution of stable copper isotopes during the progression of cholestatic liver disease induced by common bile duct ligation in mice†. *Metallomics* **11**: 1093-1103.

Craig, G., H. Wehrs, D. G. Bevan, M. Pfeifer, J. Lewis, C. D. Coath, T. Elliott, C. Huang, N. S. Lloyd and J. B. Schwieters (2021). Project Vienna: A Novel Precell Mass Filter for Collision/Reaction Cell MC-ICPMS/MS. *Analytical Chemistry* **93**: 10519-10527.

Creech, J. B., F. Moynier and N. Badullovich (2017). Tin stable isotope analysis of geological materials by double-spike MC-ICPMS. *Chemical Geology* **457**: 61-67.

Cui, M.-M., F. Moynier, B.-X. Su, W. Dai, Y. Hu, D. Rigoussen, B. Mahan and M. Le Borgne (2023). Stable potassium isotope distribution in mouse organs and red blood cells: implication for biomarker development. *Metallomics* **15**.

Cui, M.-M., F. Moynier, B.-X. Su, W. Dai, B. Mahan and M. Le Borgne (2023). Distinctive calcium isotopic composition of mice organs and fluids: implications for biological research. *Analytical and Bioanalytical Chemistry* **415**: 6839-6850.

Dai, W., F. Moynier, L. Fang and J. Siebert (2023). K-Ca dating and Ca isotope composition of the oldest Solar System lava, Erg Chech 002. *Geochemical Perspectives Letters* **24**: 33-37.

Dai, W., F. Moynier, M. Paquet, J. Moureau, B. Debret, J. Siebert, Y. Gerard and Y. Zhao (2022). Calcium isotope measurements using a collision cell (CC)-MC-ICP-MS. *Chemical Geology* **590**: 120688.

Daly, N. R. (1960). Scintillation Type Mass Spectrometer Ion Detector. *Review of Scientific Instruments* **31**: 264-267.

Date, A. R. and A. L. Gray (1981). Plasma source mass spectrometry using an inductively coupled plasma and a high resolution quadrupole mass filter. *Analyst* **106**: 1255-1267.

Date, A. R. and A. L. Gray (1983). Development progress in plasma source mass spectrometry. *Analyst* **108**: 159-165.

Date, A. R. and A. L. Gray (1983). Progress in plasma source mass spectrometry. *Spectrochimica Acta Part B: Atomic Spectroscopy* **38**: 29-37.

Date, A. R. and D. Hutchison (1986). The determination of trace elements in geochemical exploration samples by ICP-MS. *Spectrochimica Acta Part B: Atomic Spectroscopy* **41**: 175-181.

Dauphas, N. (2017). The isotopic nature of the Earth's accreting material through time. *Nature* **541**: 521-524.

Dauphas, N., T. Hopp, G. Craig, Z. J. Zhang, M. C. Valdes, P. R. Heck, B. L. A. Charlier, E. A. Bell, T. M. Harrison, A. M. Davis, L. Dussubieux, P. R. Williams, M. J. Krawczynski, C. Bouman, N. S. Lloyd, D. Tollstrup and J. B. Schwieters (2022). In situ ^{87}Rb–^{87}Sr analyses of terrestrial and extraterrestrial samples by LA-MC-ICP-MS/MS with double Wien filter and collision cell technologies. *Journal of Analytical Atomic Spectrometry* **37**: 2420-2441.

Dauphas, N., P. E. Janney, R. A. Mendybaev, M. Wadhwa, F. M. Richter, A. M. Davis, M. van Zuilen, R. Hines and C. N. Foley (2004). Chromatographic Separation and Multicollection-ICPMS Analysis of Iron. Investigating Mass-Dependent and -Independent Isotope Effects. *Analytical Chemistry* **76**: 5855-5863.

Dauphas, N., A. Pourmand and F.-Z. Teng (2009). Routine isotopic analysis of iron by HR-MC-ICPMS: How precise and how accurate? *Chemical Geology* **267**: 175-184.

Day, J. M. D. and F. Moynier (2014). Evaporative fractionation of volatile stable isotopes and their bearing on the origin of the Moon. *Philosophical Transactions of the Royal Society A: Mathematical, Physical and Engineering Sciences* **372**: 20130259.

De Groot, P. A. (2004). Handbook of stable isotope analytical techniques, Elsevier.

De La Rocha, C. L. (2002). Measurement of silicon stable isotope natural abundances via multicollector inductively coupled plasma mass spectrometry (MC-ICP-MS). *Geochemistry, Geophysics, Geosystems* **3**: 1-8.

Dean, J. R., H. G. M. Parry, R. C. Massey and L. Ebdon (1990). Continuous and flow injection hydride generation coupled with inductively coupled plasma - mass spectrometry. *ICP Information Newsletter* **15**: 569-572.

Debret, B., B. Ménez, B. Walter, H. Bouquerel, P. Bouilhol, N. Mattielli, C. Pisapia, T. Rigaudier and H. M. Williams (2022). High-pressure synthesis and storage of solid organic compounds in active subduction zones. *Science Advances* **8**: eabo2397.

Dellinger, M., R. G. Hilton and G. M. Nowell (2020). Measurements of rhenium isotopic composition in low-abundance samples. *Journal of Analytical Atomic Spectrometry* **35**: 377-387.

Dempster, A. J. (1918). A new Method of Positive Ray Analysis. *Physical Review* **11**: 316-325.

Dempster, A. J. (1935). New Ion Sources for Mass Spectroscopy. *Nature* **135**: 542-542.

Deng, Z., M. Chaussidon, M. Guitreau, I. S. Puchtel, N. Dauphas and F. Moynier (2019). An oceanic subduction origin for Archaean granitoids revealed by silicon isotopes. *Nature Geoscience* **12**: 774-778.

Deng, Z., M. Chaussidon, P. Savage, F. Robert, R. Pik and F. Moynier (2019). Titanium isotopes as a tracer for the plume or island arc affinity of felsic rocks. *Proceedings of the National Academy of Sciences* **116**: 1132-1135.

Deng, Z., M. Schiller, M. G. Jackson, M.-A. Millet, L. Pan, K. Nikolajsen, N. S. Saji, D. Huang and M. Bizzarro (2023). Earth's evolving geodynamic regime recorded by titanium isotopes. *Nature* **621**: 100-104.

Dodson, M. H. (1963). A theoretical study of the use of internal standards for precise isotopic analysis by the surface ionization technique: Part I - General first-order algebraic solutions. *Journal of Scientific Instruments* **40**: 289.

Douglas, D. (1989). Some current perspectives on ICP-MS. *Canadian journal of spectroscopy* **34**: 38-49.

Douglas, D. J. and J. B. French (1981). Elemental analysis with a microwave-induced plasma/quadrupole mass spectrometer system. *Analytical Chemistry* **53**: 37-41.

Douglas, D. J. and J. B. French (1986). An improved interface for inductively coupled plasma-mass spectrometry (ICP-MS). *Spectrochimica Acta Part B: Atomic Spectroscopy* **41**: 197-204.

Douglas, D. J. and J. B. French (1988). Gas dynamics of the inductively coupled plasma mass spectrometry interface. *Journal of Analytical Atomic Spectrometry* **3**: 743-747.

Douglas, D. J. and J. B. French (1992). Collisional focusing effects in radio frequency quadrupoles. *Journal of the American Society for Mass Spectrometry* **3**: 398-408.

Douglas, D. J. and R. S. Houk (1985). Inductively-coupled plasma mass spectrometry (ICP-MS). *Progress in analytical atomic spectroscopy* **8**: 1-18.

Douglas, D. J., E. S. K. Quan and R. G. Smith (1983). Elemental analysis with an atmospheric pressure plasma (MIP, ICP)/quadrupole mass spectrometer system. *Spectrochimica Acta Part B: Atomic Spectroscopy* **38**: 39-48.

Douglas, D. J. and S. D. Tanner (1998). Fundamental considerations in ICPMS. Inductively coupled plasma mass spectrometry. A. Montaser, Wiley-VCH**:** 616-671.

Eiden, G. C., C. J. Barinaga and D. W. Koppenaal (1996). Communication. Selective removal of plasma matrix ions in plasma source mass spectrometry. *Journal of Analytical Atomic Spectrometry* **11**: 317-322.

Eiden, G. C., C. J. Barinaga and D. W. Koppenaal (1997). Beneficial ion/molecule reactions in elemental mass spectrometry. *Rapid Communications in Mass Spectrometry* **11**: 37-42.

Eiden, G. C., C. J. Barinaga and D. W. Koppenaal (1999). Analytical performance of the plasma source RF quadrupole ion trap in elemental and isotopic MS. *Journal of Analytical Atomic Spectrometry* **14**: 1129-1132.

Elliott, T., A. Thomas, A. Jeffcoate and Y. Niu (2006). Lithium isotope evidence for subduction-enriched mantle in the source of mid-ocean-ridge basalts. *Nature* **443**: 565-568.

Ellis, A. S., T. M. Johnson, M. J. Herbel and T. D. Bullen (2003). Stable isotope fractionation of selenium by natural microbial consortia. *Chemical Geology* **195**: 119-129.

Elwaer, N. and H. Hintelmann (2008). Precise selenium isotope ratios measurement using a multimode sample introduction system (MSIS) coupled with multicollector inductively coupled plasma mass spectrometry (MC-ICP-MS). *Journal of Analytical Atomic Spectrometry* **23**: 1392-1396.

Eriksen, Z. T. and S. B. Jacobsen (2022). Calcium isotope constraints on OIB and MORB petrogenesis: The importance of melt mixing. *Earth and Planetary Science Letters* **593**: 117665.

Escoube, R., O. J. Rouxel, B. Luais, E. Ponzevera and O. F. X. Donard (2012). An intercomparison study of the germanium isotope composition of geological reference materials. *Geostandards and Geoanalytical Research* **36**: 149-159.

Evans, E. H. and L. Ebdon (1989). Simple approach to reducing polyatomic ion interferences on arsenic and selenium in inductively coupled plasma mass spectrometry. *Journal of Analytical Atomic Spectrometry* **4**: 299-300.

Evans, E. H. and L. Ebdon (1990). Effect of organic solvents and molecular gases on polyatomic ion interferences in inductively coupled plasma mass spectrometry. *Journal of Analytical Atomic Spectrometry* **5**: 425-430.

Evans, E. H. and J. J. Giglio (1993). Interferences in inductively coupled plasma mass spectrometry. A review. *Journal of Analytical Atomic Spectrometry* **8**: 1-18.

Evans, R. D., H. Hintelmann and P. J. Dillon (2001). Measurement of high precision isotope ratios for mercury from coals using transient signals. *Journal of Analytical Atomic Spectrometry* **16**: 1064-1069.

Fassel, V. A. (1978). Quantitative elemental analyses by plasma emission spectroscopy. *Science* **202**: 183-191.

Fassel, V. A. and R. N. Kniseley (1974). Inductively coupled plasma. Optical emission spectroscopy. *Analytical Chemistry* **46**: 1110A-1120a.

Fassel, V. A. and R. N. Kniseley (1974). Inductively Coupled Plasmas. *Analytical Chemistry* **46**: 1155A-1162A.

Fehr, M. A., M. Rehkämper and A. N. Halliday (2004). Application of MC-ICPMS to the precise determination of tellurium isotope compositions in chondrites, iron meteorites and sulfides. *International Journal of Mass Spectrometry* **232**: 83-94.

Feldmann, I., N. Jakubowski and D. Stuewer (1999). Application of a hexapole collision and reaction cell in ICP-MS Part I: Instrumental aspects and operational optimization. *Fresenius' Journal of Analytical Chemistry* **365**: 415-421.

Fenn, J. B. (2000). Mass spectrometric implications of high-pressure ion sources. *International Journal of Mass Spectrometry* **200**: 459-478.

Fietzke, J. and A. Eisenhauer (2006). Determination of temperature-dependent stable strontium isotope ($^{88}Sr/^{86}Sr$) fractionation via bracketing standard MC-ICP-MS. *Geochemistry, Geophysics, Geosystems* **7**.

Fietzke, J., A. Eisenhauer, N. Gussone, B. Bock, V. Liebetrau, T. F. Nägler, H. J. Spero, J. Bijma and C. Dullo (2004). Direct measurement of $^{44}Ca/^{40}Ca$ ratios by MC–ICP–MS using the cool plasma technique. *Chemical Geology* **206**: 11-20.

Finnigan, R. E. (1994). Quadrupole mass spectrometers. *Analytical Chemistry* **66**: 969A-975A.

Fornadel, A. P., P. G. Spry, S. E. Jackson, R. D. Mathur, J. B. Chapman and I. Girard (2014). Methods for the determination of stable Te isotopes of minerals in the system Au–Ag–Te by MC-ICP-MS. *Journal of Analytical Atomic Spectrometry* **29**: 623-637.

Foster, G. L. (2008). Seawater pH, pCO_2 and $[CO^{2-}_3]$ variations in the Caribbean Sea over the last 130 kyr: A boron isotope and B/Ca study of planktic foraminifera. *Earth and Planetary Science Letters* **271**: 254-266.

Fu, H., S. B. Jacobsen, B. T. Larsen and Z. T. Eriksen (2022). Ca-isotopes as a robust tracer of magmatic differentiation. *Earth and Planetary Science Letters* **594**: 117743.

Fu, H., S. B. Jacobsen and F. Sedaghatpour (2023). Moon's high-energy giant-impact origin and differentiation timeline inferred from Ca and Mg stable isotopes. *Communications Earth & Environment* **4**: 307.

Futrell, J. H. and C. D. Miller (1966). Tandem mass spectrometer for study of ion ‐ molecule reactions. *Review of Scientific Instruments* **37**: 1521-1526.

Galy, A., N. S. Belshaw, L. Halicz and R. K. O'Nions (2001). High-precision measurement of magnesium isotopes by multiple-collector inductively coupled plasma mass spectrometry. *International Journal of Mass Spectrometry* **208**: 89-98.

Gao, B.-Y., B.-X. Su, W.-J. Li, M. Yuan, J. Sun, Y. Zhao and X. Liu (2022). High-precision analysis of calcium isotopes using a Nu Sapphire collision cell (CC)-MC-ICP-MS. *Journal of Analytical Atomic Spectrometry* **37**: 2111-2121.

Geng, H., R. Yin and X. Li (2018). An optimized protocol for high precision measurement of Hg isotopic compositions in samples with low concentrations of Hg using MC-ICP-MS. *Journal of Analytical Atomic Spectrometry* **33**: 1932-1940.

Georg, R. B., B. C. Reynolds, M. Frank and A. N. Halliday (2006). New sample preparation techniques for the determination of Si isotopic compositions using MC-ICPMS. *Chemical Geology* **235**: 95-104.

Gillson, G. R., D. J. Douglas, J. E. Fulford, K. W. Halligan and S. D. Tanner (1988). Nonspectroscopic interelement interferences in inductively coupled plasma mass spectrometry. *Analytical Chemistry* **60**: 1472-1474.

Godden, R. G. and D. R. Thomerson (1980). Generation of covalent hydrides in atomic-absorption spectroscopy. A review. *Analyst* **105**: 1137-1156.

Gray, A. and A. Date (1981). The use of an inductively coupled plasma as an ion source for aqueous solution samples. *Dyn. Mass Spectrom.* **6**: 252.

Gray, A. L. (1974). It all depends on the source. *Proceedings of the Society for Analytical Chemistry* **11**: 182-183.

Gray, A. L. (1975). Mass-spectrometric analysis of solutions using an atmospheric pressure ion source. *Analyst* **100**: 289-299.

Gray, A. L. (1975). Plasma sampling mass spectrometry for trace analysis of solutions. *Analytical Chemistry* **47**: 600-601.

Gray, A. L. and A. R. Date (1983). Inductively coupled plasma source mass spectrometry using continuum flow ion extraction. *Analyst* **108**: 1033-1050.

Greber, N. D., N. Dauphas, A. Bekker, M. P. Ptáček, I. N. Bindeman and A. Hofmann (2017). Titanium isotopic evidence for felsic crust and plate tectonics 3.5 billion years ago. *Science* **357**: 1271-1274.

Greenfield, S. (2000). Invention of the Annular Inductively Coupled Plasma as a Spectroscopic Source. *Journal of Chemical Education* **77**: 584.

Greenfield, S., I. L. Jones and C. T. Berry (1964). High-pressure plasmas as spectroscopic emission sources. *Analyst* **89**: 713-720.

Greenfield, S., I. L. Jones, H. M. McGeachin and P. B. Smith (1975). Automatic multi-sample simultaneous multi-element analysis with a h.f. plasma torch and direct reading spectrometer. *Analytica Chimica Acta* **74**: 225-245.

Greenfield, S. and H. M. McGeachin (1978). Calorimetric and dimensional studies on inductively coupled plasmas. *Analytica Chimica Acta* **100**: 101-119.

Grigoryan, R., M. Costas-Rodríguez, P. Santens and F. Vanhaecke (2020). Multicollector Inductively Coupled Plasma–Mass Spectrometry with 1013 Ω Faraday Cup Amplifiers for Ultrasensitive Mg Isotopic Analysis of Cerebrospinal Fluid Microsamples. *Analytical Chemistry* **92**: 15975-15981.

Gueguen, B., O. Rouxel, E. Ponzevera, A. Bekker and Y. Fouquet (2013). Nickel isotope variations in terrestrial silicate rocks and geological reference materials measured by MC-ICP-MS. *Geostandards and Geoanalytical Research* **37**: 297-317.

Guilbaud, R., R. M. Ellam, I. B. Butler, V. Gallagher and K. Keefe (2010). A procedural development for the analysis of $^{56/54}$Fe and $^{57/54}$Fe isotope ratios with new generation IsoProbe MC-ICP-MS. *Journal of Analytical Atomic Spectrometry* **25**: 1598-1604.

Gustavsson, A. and P. Hietala (1990). A membrane interface for aqueous sample introduction into inductively coupled plasmas. *Spectrochimica Acta Part B: Atomic Spectroscopy* **45**: 1103-1108.

Halicz, L., A. Galy, N. S. Belshaw and R. Keith O'Nions (1999). High-precision measurement of calcium isotopes in carbonates and related materials by multiple collector inductively coupled plasma mass spectrometry (MC-ICP-MS). *Journal of Analytical Atomic Spectrometry* **14**: 1835-1838.

Halliday, A. N., D.-C. Lee, J. N. Christensen, M. Rehkämper, W. Yi, X. Luo, C. M. Hall, C. J. Ballentine, T. Pettke and C. Stirling (1998). Applications of multiple collector-ICPMS to cosmochemistry, geochemistry, and paleoceanography. *Geochimica et Cosmochimica Acta* **62**: 919-940.

Halliday, A. N., D.-C. Lee, J. N. Christensen, A. J. Walder, P. A. Freedman, C. E. Jones, C. M. Hall, W. Yi and D. Teagle (1995). Recent developments in inductively coupled plasma magnetic sector multiple collector mass spectrometry. *International Journal of Mass Spectrometry and Ion Processes* **146-147**: 21-33.

Hassler, A., J. E. Martin, R. Amiot, T. Tacail, F. A. Godet, R. Allain and V. Balter (2018). Calcium isotopes offer clues on resource partitioning among Cretaceous predatory dinosaurs. *Proceedings of the Royal Society B: Biological Sciences* **285**: 20180197.

Hayhurst, A. N. and D. B. Kittelson (1977). Mass spectrometric sampling of ions from atmospheric pressure flames—III: Boundary layer and other cooling of the sample. *Combustion and Flame* **28**: 137-143.

Hayhurst, A. N., N. R. Telford and T. M. Sugden (1971). The occurrence of chemical reactions in supersonic expansions of a gas into a vacuum and its relation to mass spectrometric sampling. *Proceedings of the Royal Society of London. A. Mathematical and Physical Sciences* **322**: 483-507.

He, J., J. Meija and L. Yang (2021). Determination of the isotopic composition of zirconium using MC-ICPMS and a regression model for mass bias correction. *Analytical Chemistry* **93**: 5107-5113.

He, M., Z. Jin, H. Lu, L. Deng and C. Luo (2016). The different cones combination enhanced sensitivity on MC-ICP-MS: The results from boron isotope analysis. *International Journal of Mass Spectrometry* **408**: 33-37.

He, Y., A.-Y. Sun, Y.-C. Zhang, R.-Y. Yang, S. Ke, Y. Wang and F.-Z. Teng (2022). High-precision and high-accuracy magnesium isotope analysis on multiple-collector inductively coupled plasma mass spectrometry using a critical mixture double spike technique. *Solid Earth Sciences* **7**: 188-199.

Heitkemper, D. T. and J. A. Caruso (1990). Continuous Hydride Generation for Simultaneous Multielement Detection with Inductively Coupled Plasma Mass Spectrometry. *Applied Spectroscopy* **44**: 228-234.

Hellmann, J. L., T. Hopp, C. Burkhardt and T. Kleine (2020). Origin of volatile element depletion among carbonaceous chondrites. *Earth and Planetary Science Letters* **549**: 116508.

Hendriks, L., A. Gundlach-Graham, B. Hattendorf and D. Günther (2017). Characterization of a new ICP-TOFMS instrument with continuous and discrete introduction of solutions. *Journal of Analytical Atomic Spectrometry* **32**: 548-561.

Hiess, J., D. J. Condon, N. McLean and S. R. Noble (2012). $^{238}U/^{235}U$ systematics in terrestrial uranium-bearing minerals. *Science* **335**: 1610-1614.

Higgins, J. A., D. S. Ramos, S. Gili, C. Spetea, S. Kanoski, D. Ha, A. A. McDonough and J. H. Youn (2022). Stable potassium isotopes ($^{41}K/^{39}K$) track transcellular and paracellular potassium transport in biological systems. *Frontiers in Physiology* **13**.

Hill Gallant, K. M. and X.-Y. Zheng (2022). Natural stable calcium isotope ratios: a new gold standard for bone balance? *Kidney International* **102**: 473-476.

Hill, S. J. (2008). Inductively coupled plasma spectrometry and its applications, John Wiley & Sons.

Hirata, T. (1996). Lead isotopic analyses of NIST Standard Reference Materials using multiple collector inductively coupled plasma mass spectrometry coupled with a modified external correction method for mass discrimination effect. *Analyst* **121**: 1407-1411.

Hirata, T. (1997). Isotopic variations of germanium in iron and stony iron meteorites. *Geochimica et Cosmochimica Acta* **61**: 4439-4448.

Hobin, K., M. Costas Rodríguez and F. Vanhaecke (2021). Robust potassium isotopic analysis of geological and biological samples via multicollector ICP-mass spectrometry using the "Extra-High Resolution Mode". *Analytical Chemistry* **93**: 8881-8888.

Hofmann, A. (1971). Fractionation corrections for mixed-isotope spikes of Sr, K, and Pb. *Earth and Planetary Science Letters* **10**: 397-402.

Holliday, A. and D. Beauchemin (2002). Radial profiles of ion abundance in cold plasmas and mixed-gas plasmas in inductively coupled plasma mass spectrometry. *Canadian journal of analytical sciences and spectroscopy* **47**: 91-97.

Holliday, A. E. and D. Beauchemin (2003). Spatial profiling of ion distributions in a nitrogen–argon plasma in inductively coupled plasma mass spectrometry. *Journal of Analytical Atomic Spectrometry* **18**: 289-295.

Hopp, T., N. Dauphas, F. Spitzer, C. Burkhardt and T. Kleine (2022). Earth's accretion inferred from iron isotopic anomalies of supernova nuclear statistical equilibrium origin. *Earth and Planetary Science Letters* **577**: 117245.

Hopp, T., M. Fischer-Gödde and T. Kleine (2016). Ruthenium stable isotope measurements by double spike MC-ICPMS. *Journal of Analytical Atomic Spectrometry* **31**: 1515-1526.

Houk, R. S. (1986). Mass Spectrometry of Inductively Coupled Plasmas. *Analytical Chemistry* **58**: 97A-105A.

Houk, R. S., V. A. Fassel, G. D. Flesch, H. J. Svec, A. L. Gray and C. E. Taylor (1980). Inductively coupled argon plasma as an ion source for mass spectrometric determination of trace elements. *Analytical Chemistry* **52**: 2283-2289.

Houk, R. S., V. A. Fassel and H. J. Svec (1981). Inductively coupled plasma-mass spectrometry: sample introduction, ionizaiton, ion extraction, and analytical results. Dynamic Mass Spectrometry. D. Price and J. F. J. Todd. London, Heyden. **6:** 234-251.

Houk, R. S., A. Montaser and V. A. Fassel (1983). Mass spectra and ionization temperatures in an argon-nitrogen inductively coupled plasma. *Applied Spectroscopy* **37**: 425-428.

Hu, J. Y., N. Dauphas, F. L. H. Tissot, R. Yokochi, T. J. Ireland, Z. Zhang, A. M. Davis, F. J. Ciesla, L. Grossman, B. L. A. Charlier, M. Roskosz, E. E. Alp, M. Y. Hu and J. Zhao (2021). Heating events in the nascent solar system recorded by rare earth element isotopic fractionation in refractory inclusions. *Science Advances* **7**: eabc2962.

Hu, Y., X.-Y. Chen, Y.-K. Xu and F.-Z. Teng (2018). High-precision analysis of potassium isotopes by HR-MC-ICPMS. *Chemical Geology* **493**: 100-108.

Hu, Y., F. Moynier and M. Bizzarro (2022). Potassium isotope heterogeneity in the early Solar System controlled by extensive evaporation and partial recondensation. *Nature Communications* **13**: 7669.

Hu, Y., F. Moynier, W. Dai, M. Paquet, T. Yokoyama, Y. Abe, J. Aléon, C. M. O. D. Alexander, S. Amari, Y. Amelin, K.-i. Bajo, M. Bizzarro, A. Bouvier, R. W. Carlson, M. Chaussidon, B.-G. Choi, N. Dauphas, A. M. Davis, T. Di Rocco, W. Fujiya, R. Fukai, I. Gautam, M. K. Haba, Y. Hibiya, H. Hidaka, H. Homma, P. Hoppe, G. R. Huss, K. Ichida, T. Iizuka, T. R. Ireland, A. Ishikawa, S. Itoh, N. Kawasaki, N. T. Kita, K. Kitajima, T. Kleine, S. Komatani, A. N. Krot, M.-C. Liu, Y. Masuda, M. Morita, K. Motomura, I. Nakai, K. Nagashima, D. Nesvorný, A. Nguyen, L. Nittler, M. Onose, A. Pack, C. Park, L. Piani, L. Qin, S. S. Russell, N. Sakamoto, M. Schönbächler, L. Tafla, H. Tang, K. Terada, Y. Terada, T. Usui, S. Wada, M. Wadhwa, R. J. Walker, K. Yamashita, Q.-Z. Yin, S. Yoneda, E. D. Young, H. Yui, A.-C. Zhang, T. Nakamura, H. Naraoka, T. Noguchi, R. Okazaki, K. Sakamoto, H. Yabuta, M. Abe, A. Miyazaki, A. Nakato, M. Nishimura, T. Okada, T. Yada, K. Yogata, S. Nakazawa, T. Saiki, S. Tanaka, F. Terui, Y. Tsuda, S.-i. Watanabe, M. Yoshikawa, S. Tachibana and H. Yurimoto (2024). Pervasive aqueous alteration in the early Solar System revealed by potassium isotopic variations in Ryugu samples and carbonaceous chondrites. *Icarus* **409**: 115884.

Hu, Y., F. Moynier and X. Yang (2023). Volatile-depletion processing of the building blocks of Earth and Mars as recorded by potassium isotopes. *Earth and Planetary Science Letters* **620**: 118319.

Hu, Y. and F.-Z. Teng (2019). Optimization of analytical conditions for precise and accurate isotope analyses of Li, Mg, Fe, Cu, and Zn by MC-ICPMS. *Journal of Analytical Atomic Spectrometry* **34**: 338-346.

Hu, Z., S. Gao, Y. Liu, S. Hu, H. Chen and H. Yuan (2008). Signal enhancement in laser ablation ICP-MS by addition of nitrogen in the central channel gas. *Journal of Analytical Atomic Spectrometry* **23**: 1093-1101.

Huang, B., X. Zeng, Z. Zhang and J. Liu (1988). Recent studies on inductively coupled plasma sample introduction-1: Hydride generation. *Spectrochimica Acta Part B: Atomic Spectroscopy* **43**: 381-389.

Huang, B., Z. Zhang and X. Zeng (1987). A new nebulizer-hydride generator system for simultaneous multielement inductively coupled plasma-atomic emission spectrometry. *Spectrochimica Acta Part B: Atomic Spectroscopy* **42**: 129-137.

Huang, G., R. N. Mitchell, R. M. Palin, C. J. Spencer and J. Guo (2022). Barium content of Archaean continental crust reveals the onset of subduction was not global. *Nature Communications* **13**: 6553.

Huang, K.-J., F.-Z. Teng, B. Shen, S. Xiao, X. Lang, H.-R. Ma, Y. Fu and Y. Peng (2016). Episode of intense chemical weathering during the termination of the 635 Ma Marinoan glaciation. *Proceedings of the National Academy of Sciences* **113**: 14904-14909.

Huang, S., J. Farkaš and S. B. Jacobsen (2010). Calcium isotopic fractionation between clinopyroxene and orthopyroxene from mantle peridotites. *Earth and Planetary Science Letters* **292**: 337-344.

Huang, S. and S. B. Jacobsen (2021). Calcium isotope compositions as a means to trace carbonate recycling. *National Science Review* **9**.

Iden, C. R., R. Liardon and W. S. Koski (1972). Kinematics of the C+(D_2, D)CD+ Reaction. *The Journal of Chemical Physics* **56**: 851-854.

Inglis, E. C., J. B. Creech, Z. Deng and F. Moynier (2018). High-precision zirconium stable isotope measurements of geological reference materials as measured by double-spike MC-ICPMS. *Chemical Geology* **493**: 544-552.

Jakubowski, N., T. Prohaska, L. Rottmann and F. Vanhaecke (2011). Inductively coupled plasma- and glow discharge plasma-sector field mass spectrometry Part I. Tutorial: Fundamentals and instrumentation. *Journal of Analytical Atomic Spectrometry* **26**: 693-726.

Jaouen, K. and M.-L. Pons (2017). Potential of non-traditional isotope studies for bioarchaeology. *Archaeological and Anthropological Sciences* **9**: 1389-1404.

Jarvis, K. E., A. L. Gray, R. S. Houk, I. Jarvis, J. MacLaren and J. G. Williams (1992). Handbook of inductively coupled plasma mass spectrometry.

Jiang, S. J., R. S. Houk and M. A. Stevens (1988). Alleviation of overlap interferences for determination of potassium isotope ratios by inductively coupled plasma mass spectrometry. *Analytical Chemistry* **60**: 1217-1221.

Johnson, C. M., B. L. Beard and F. Albarède (2004). Geochemistry of Non-Traditional Stable Isotopes. Berlin, Boston, De Gruyter.

Johnson, E. G. and A. O. Nier (1953). Angular aberrations in sector shaped electromagnetic lenses for focusing beams of charged particles. *Physical Review* **91**: 10-17.

Johnson, T. H. (1927). Intensities of Molecular Beams. *Nature* **119**: 745-746.

Johnson, T. H. (1928). The Production and Measurement of Molecular Beams. *Physical Review* **31**: 103-114.

Johnson, T. M., J. L. Druhan, A. Basu, N. E. Jemison, X. Wang, K. Schilling and N. L. Wasserman (2022). A review of the development of Cr, Se, U, Sb, and Te isotopes as indicators of redox reactions, contaminant fate, and contaminant transport in aqueous systems. Isotopic Constraints on Earth System Processes**:** 237-269.

Kantrowitz, A. and J. Grey (1951). A high intensity source for the molecular beam. Part I. Theoretical. *Review of Scientific Instruments* **22**: 328-332.

Karasiński, J., A. Tupys, L. Halicz and E. Bulska (2021). A novel approach for the determination of the Ge isotope ratio using liquid–liquid extraction and hydride generation by multicollector inductively coupled plasma mass spectrometry. *Analytical Chemistry* **93**: 13548-13554.

Kato, C. and F. Moynier (2017). Gallium isotopic evidence for extensive volatile loss from the Moon during its formation. *Science Advances* **3**: e1700571.

Kato, C., F. Moynier, J. Foriel, F.-Z. Teng and I. S. Puchtel (2017). The gallium isotopic composition of the bulk silicate Earth. *Chemical Geology* **448**: 164-172.

Kato, C., F. Moynier, M. C. Valdes, J. K. Dhaliwal and J. M. D. Day (2015). Extensive volatile loss during formation and differentiation of the Moon. *Nature Communications* **6**: 7617.

King, F. L. and W. W. Harrison (1989). Collision-induced dissociation of polyatomic ions in glow discharge mass spectrometry. *International Journal of Mass Spectrometry and Ion Processes* **89**: 171-185.

Kistiakowsky, G. B. and W. P. Slichter (1951). A High Intensity Source for the Molecular Beam. Part II. Experimental. *Review of Scientific Instruments* **22**: 333-337.

Klaver, M. and C. D. Coath (2019). Obtaining Accurate Isotopic Compositions with the Double Spike Technique: Practical Considerations. *Geostandards and Geoanalytical Research* **43**: 5-22.

Klaver, M., T.-H. Luu, J. Lewis, M. N. Jansen, M. Anand, J. Schwieters and T. Elliott (2021). The Ca isotope composition of mare basalts as a probe into the heterogeneous lunar mantle. *Earth and Planetary Science Letters* **570**: 117079.

Kleine, T., G. Budde, C. Burkhardt, T. S. Kruijer, E. A. Worsham, A. Morbidelli and F. Nimmo (2020). The non-carbonaceous–carbonaceous meteorite dichotomy. *Space Science Reviews* **216**: 55.

Kleine, T., C. Münker, K. Mezger and H. Palme (2002). Rapid accretion and early core formation on asteroids and the terrestrial planets from Hf–W chronometry. *Nature* **418**: 952-955.

Kleine, T. and R. J. Walker (2017). Tungsten isotopes in planets. *Annual Review of Earth and Planetary Sciences* **45**: 389-417.

Kniseley, R. N., H. Amenson, C. C. Butler and V. A. Fassel (1974). An Improved Pneumatic Nebulizer for Use at Low Nebulizing Gas Flows. *Applied Spectroscopy* **28**: 285-286.

Koefoed, P., J.-A. Barrat, O. Pravdivtseva, C. M. O'D. Alexander, K. Lodders, R. Ogliore and K. Wang (2023). The potassium isotopic composition of CI chondrites and the origin of isotopic variations among primitive planetary bodies. *Geochimica et Cosmochimica Acta*.

Koornneef, J. M., C. Bouman, J. B. Schwieters and G. R. Davies (2014). Measurement of small ion beams by thermal ionisation mass spectrometry using new 1013Ohm resistors. *Analytica Chimica Acta* **819**: 49-55.

Koppenaal, D. W., C. J. Barinaga and M. R. Smith (1994). Performance of an inductively coupled plasma source ion trap mass spectrometer. *Journal of Analytical Atomic Spectrometry* **9**: 1053-1058.

Koppenaal, D. W., G. C. Eiden and C. J. Barinaga (2004). Collision and reaction cells in atomic mass spectrometry: development, status, and applications. *Journal of Analytical Atomic Spectrometry* **19**: 561-570.

Kruijer, T. S., T. Kleine and L. E. Borg (2020). The great isotopic dichotomy of the early Solar System. *Nature Astronomy* **4**: 32-40.

Ku, Y. and S. B. Jacobsen (2020). Potassium isotope anomalies in meteorites inherited from the protosolar molecular cloud. *Science Advances* **6**: eabd0511.

Ku, Y., M. I. Petaev and S. B. Jacobsen (2022). The timing of potential last nucleosynthetic injections into the protosolar molecular cloud inferred from ^{41}Ca–^{26}Al systematics of bulk CAIs. *The Astrophysical Journal Letters* **931**: L13.

Kurzawa, T., S. König, J. Labidi, A. Yierpan and R. Schoenberg (2017). A method for Se isotope analysis of low ng-level geological samples via double spike and hydride generation MC-ICP-MS. *Chemical Geology* **466**: 219-228.

LaFreniere, K. E., V. A. Fassel and D. E. Eckels (1987). Elemental speciation via high-performance liquid chromatography combined with inductively coupled plasma atomic emission spectroscopic detection: application of a direct injection nebulizer. *Analytical Chemistry* **59**: 879-887.

LaFreniere, K. E., G. W. Rice and V. A. Fassel (1985). Flow injection analysis with inductively coupled plasma-atomic emission spectroscopy: critical comparison of conventional pneumatic, ultrasonic and direct injection nebulization. *Spectrochimica Acta Part B: Atomic Spectroscopy* **40**: 1495-1504.

Lam, J. W. and J. W. McLaren (1990). Use of aerosol processing and nitrogen-argon plasmas for reduction of oxide interference in inductively coupled plasma mass spectrometry. *Journal of Analytical Atomic Spectrometry* **5**: 419-424.

Lam, J. W. H. and G. Horlick (1990). A comparison of argon and mixed gas plasmas for inductively coupled plasma-mass spectrometry. *Spectrochimica Acta Part B: Atomic Spectroscopy* **45**: 1313-1325.

Langmuir, I. (1928). Oscillations in Ionized Gases. *Proceedings of the National Academy of Sciences* **14**: 627-637.

Lauretta, D. S., B. Klaue, J. D. Blum and P. R. Buseck (2001). Mercury abundances and isotopic compositions in the Murchison (CM) and Allende (CV) carbonaceous chondrites. *Geochimica et Cosmochimica Acta* **65**: 2807-2818.

Lécuyer, C., P. Grandjean, B. Reynard, F. Albarède and P. Telouk (2002). ^{11}B/^{10}B analysis of geological materials by ICP–MS Plasma 54: Application to the boron fractionation between brachiopod calcite and seawater. *Chemical Geology* **186**: 45-55.

Lee, D.-C. and A. N. Halliday (1995). Hafnium–tungsten chronometry and the timing of terrestrial core formation. *Nature* **378**: 771-774.

Lee, D.-C. and A. N. Halliday (1995). Precise determinations of the isotopic compositions and atomic weights of molybdenum, tellurium, tin and tungsten using ICP magnetic sector multiple collector mass spectrometry. *International Journal of Mass Spectrometry and Ion Processes* **146-147**: 35-46.

Lewis, J., T.-H. Luu, C. D. Coath, H. Wehrs, J. B. Schwieters and T. Elliott (2022). Collision course; high-precision mass-independent and mass-dependent calcium isotope

measurements using the prototype collision cell MC-ICPMS/MS, Proteus. *Chemical Geology* **614**: 121185.
Li, W., B. L. Beard and S. Li (2016). Precise measurement of stable potassium isotope ratios using a single focusing collision cell multi-collector ICP-MS. *Journal of Analytical Atomic Spectrometry* **31**: 1023-1029.
Li, W., M. Cui, Q. Pan, J. Wang, B. Gao, S. Liu, M. Yuan, B. Su, Y. Zhao, F.-Z. Teng and G. Han (2022). High-precision potassium isotope analysis using the Nu Sapphire collision cell (CC)-MC-ICP-MS. *Science China Earth Sciences* **65**: 1510-1521.
Liu, D., F. Moynier, P. A. Sossi, R. Pik, S. A. Halldórsson, E. Inglis, J. M. D. Day and J. Siebert (2023). The indium isotopic composition of the bulk silicate Earth. *Geochimica et Cosmochimica Acta* **352**: 24-35.
Liu, S., W. Li, B. Su, B. Gao, J. Wang, C. Wang, Y. Luo, L. Yan and Y. Zhao (2023). High-precision lithium isotopic analysis using the Nu Sapphire MC-ICP-MS. *Journal of Analytical Atomic Spectrometry* **38**: 656-666.
Liu, S.-A., D. Li, S. Li, F.-Z. Teng, S. Ke, Y. He and Y. Lu (2014). High-precision copper and iron isotope analysis of igneous rock standards by MC-ICP-MS. *Journal of Analytical Atomic Spectrometry* **29**: 122-133.
Liu, S.-A., Y.-R. Qu, Z.-Z. Wang, M.-L. Li, C. Yang and S.-G. Li (2022). The fate of subducting carbon tracked by Mg and Zn isotopes: A review and new perspectives. *Earth-Science Reviews* **228**: 104010.
Liu, S.-A., H. Wu, S.-z. Shen, G. Jiang, S. Zhang, Y. Lv, H. Zhang and S. Li (2017). Zinc isotope evidence for intensive magmatism immediately before the end-Permian mass extinction. *Geology* **45**: 343-346.
Liu, X.-M. and W. Li (2019). Optimization of lithium isotope analysis in geological materials by quadrupole ICP-MS. *Journal of Analytical Atomic Spectrometry* **34**: 1708-1717.
Longerich, H. P. (1989). Effect of nitric acid, acetic acid and ethanol on inductively coupled plasma mass spectrometric ion signals as a function of nebuliser gas flow, with implications on matrix suppression and enhancements. *Journal of Analytical Atomic Spectrometry* **4**: 665-667.
Longerich, H. P., B. J. Fryer and D. F. Strong (1987). Determination of lead isotope ratios by inductively coupled plasma-mass spectrometry (ICP-MS). *Spectrochimica Acta Part B: Atomic Spectroscopy* **42**: 39-48.
Louvat, P., J. Bouchez and G. Paris (2011). MC-ICP-MS isotope measurements with direct injection nebulisation (d-DIHEN): Optimisation and application to boron in seawater and carbonate samples. *Geostandards and Geoanalytical Research* **35**: 75-88.
Luais, B. (2007). Isotopic fractionation of germanium in iron meteorites: Significance for nebular condensation, core formation and impact processes. *Earth and Planetary Science Letters* **262**: 21-36.
Luais, B., X. Framboisier, J. Carignan and J. Ludden (2000). Analytical development of Ge isotopic analyses using multi-collection plasma source mass spectrometry: Isoprobe MC-Hex-ICP-MS (Micromass). Geoanalysis 2000, Symposium B.
Luck, J.-M., D. B. Othman and F. Albarède (2005). Zn and Cu isotopic variations in chondrites and iron meteorites: Early solar nebula reservoirs and parent-body processes. *Geochimica et Cosmochimica Acta* **69**: 5351-5363.
Luck, J. M., D. B. Othman, J. A. Barrat and F. Albarède (2003). Coupled 63Cu and 16O excesses in chondrites. *Geochimica et Cosmochimica Acta* **67**: 143-151.

Lum, T.-S. and K. S.-Y. Leung (2016). Strategies to overcome spectral interference in ICP-MS detection. *Journal of Analytical Atomic Spectrometry* **31**: 1078-1088.

Luu, T.-H., D. Peters, E. Lahoud, Y. Gérard and F. Moynier (2024). Copper Isotope Compositions Measured Using a Sapphire Dual Path MC-ICPMS with a Collision/Reaction Cell. *Analytical Chemistry* **96**: 2199-2205.

Lyon, T. D. B., G. S. Fell, R. C. Hutton and A. N. Eaton (1988). Evaluation of inductively coupled argon plasma mass spectrometry (ICP-MS) for simultaneous multi-element trace analysis in clinical chemistry. *Journal of Analytical Atomic Spectrometry* **3**: 265-271.

Ma, J., G. Wei, Y. Liu, Z. Ren, Y. Xu and Y. Yang (2013). Precise measurement of stable ($\delta^{88/86}$Sr) and radiogenic (^{87}Sr/^{86}Sr) strontium isotope ratios in geological standard reference materials using MC-ICP-MS. *Chinese Science Bulletin* **58**: 3111-3118.

Ma, J., G. Wei, Y. Liu, Z. Ren, Y. Xu and Y. Yang (2013). Precise measurement of stable neodymium isotopes of geological materials by using MC-ICP-MS. *Journal of Analytical Atomic Spectrometry* **28**: 1926-1931.

Mahan, B., R. S. Chung, D. L. Pountney, F. Moynier and S. Turner (2020). Isotope metallomics approaches for medical research. *Cellular and Molecular Life Sciences* **77**: 3293-3309.

Mahan, B., T. Tacail, J. Lewis, T. Elliott, M. Habekost, S. Turner, R. Chung and F. Moynier (2022). Exploring the K isotope composition of Göttingen minipig brain regions, and implications for Alzheimer's disease. *Metallomics* **14**.

Mamyrin, B. A., V. I. Karataev, D. V. Shmikk and V. A. Zagulin (1973). The mass-reflectron, a new nonmagnetic time-of-flight mass spectrometer with high resolution. *Zh. Eksp. Teor. Fiz* **64**: 82-89.

Marchante-Gayón, J., L. H. Reyes, J. Alonso and A. Sanz-Medel (2003). Determination of selenium in biological samples by isotope dilution analysis octapole reaction system ICP-MS. Plasma Source Mass Spectrometry: Applications and Emerging Technologies. J. G. Holland and S. D. Tanner, Royal Society of Chemistry**:** 271-281.

Maréchal, C. N., P. Télouk and F. Albarède (1999). Precise analysis of copper and zinc isotopic compositions by plasma-source mass spectrometry. *Chemical Geology* **156**: 251-273.

Martin, J. E., A. Hassler, G. Montagnac, F. Therrien and V. Balter (2022). The stability of dinosaur communities before the Cretaceous–Paleogene (K–Pg) boundary: A perspective from southern Alberta using calcium isotopes as a dietary proxy. *GSA Bulletin* **134**: 2548-2560.

Martin, J. E., T. Tacail and V. Balter (2017). Non-traditional isotope perspectives in vertebrate palaeobiology. *Palaeontology* **60**: 485-502.

Martins, R., S. Kuthning, B. J. Coles, K. Kreissig and M. Rehkämper (2023). Nucleosynthetic isotope anomalies of zinc in meteorites constrain the origin of Earth's volatiles. *Science* **379**: 369-372.

Mattauch, J. and R. Herzog (1934). Über einen neuen Massenspektrographen. *Zeitschrift für Physik* **89**: 786-795.

McGilvery, D. C. and J. D. Morrison (1978). A mass spectrometer for the study of laser-induced photodissociation of ions. *International Journal of Mass Spectrometry and Ion Physics* **28**: 81-92.

Meinhard, J. E. (1976). The concentric glass nebulizer. *ICP Information Newsletter* **2**: 163-165.

Meinhard, J. E. (1979). Pneumatic nebulizers, present and future. *Applications of Plasma Emission Spectroscopy, Heyden, London*: 1-14.

Miller, P. E. and M. B. Denton (1986). The quadrupole mass filter: Basic operating concepts. *Journal of Chemical Education* **63**: 617.

Millet, M.-A. and N. Dauphas (2014). Ultra-precise titanium stable isotope measurements by double-spike high resolution MC-ICP-MS. *Journal of Analytical Atomic Spectrometry* **29**: 1444-1458.

Millet, M.-A., N. Dauphas, N. D. Greber, K. W. Burton, C. W. Dale, B. Debret, C. G. Macpherson, G. M. Nowell and H. M. Williams (2016). Titanium stable isotope investigation of magmatic processes on the Earth and Moon. *Earth and Planetary Science Letters* **449**: 197-205.

Misra, S. and P. N. Froelich (2009). Measurement of lithium isotope ratios by quadrupole-ICP-MS: application to seawater and natural carbonates. *Journal of Analytical Atomic Spectrometry* **24**: 1524-1533.

Moens, L. J., F. F. Vanhaecke, D. R. Bandura, V. I. Baranov and S. D. Tanner (2001). Elimination of isobaric interferences in ICP-MS, using ion–molecule reaction chemistry: Rb/Sr age determination of magmatic rocks, a case study. *Journal of Analytical Atomic Spectrometry* **16**: 991-994.

Montaser, A. (1998). Inductively coupled plasma mass spectrometry, John Wiley & Sons.

Montaser, A., S. K. Chan and D. W. Koppenaal (1987). Inductively coupled helium plasma as an ion source for mass spectrometry. *Analytical Chemistry* **59**: 1240-1242.

Morel, J.-D., L. Sauzéat, L. J. E. Goeminne, P. Jha, E. Williams, R. H. Houtkooper, R. Aebersold, J. Auwerx and V. Balter (2022). The mouse metallomic landscape of aging and metabolism. *Nature Communications* **13**: 607.

Morgan, L. E., D. P. Santiago Ramos, B. Davidheiser-Kroll, J. Faithfull, N. S. Lloyd, R. M. Ellam and J. A. Higgins (2018). High-precision 41K/39K measurements by MC-ICP-MS indicate terrestrial variability of δ41K. *Journal of Analytical Atomic Spectrometry* **33**: 175-186.

Moynier, F., A. Agranier, D. C. Hezel and A. Bouvier (2010). Sr stable isotope composition of Earth, the Moon, Mars, Vesta and meteorites. *Earth and Planetary Science Letters* **300**: 359-366.

Moynier, F., J. Blichert-Toft, P. Telouk, J.-M. Luck and F. Albarède (2007). Comparative stable isotope geochemistry of Ni, Cu, Zn, and Fe in chondrites and iron meteorites. *Geochimica et Cosmochimica Acta* **71**: 4365-4379.

Moynier, F., M. L. Borgne, E. Lahoud, B. Mahan, F. Mouton-Liger, J. Hugon and C. Paquet (2020). Copper and zinc isotopic excursions in the human brain affected by Alzheimer's disease. *Alzheimer's & Dementia: Diagnosis, Assessment & Disease Monitoring* **12**: e12112.

Moynier, F., J. Chen, K. Zhang, H. Cai, Z. Wang, M. G. Jackson and J. M. D. Day (2020). Chondritic mercury isotopic composition of Earth and evidence for evaporative equilibrium degassing during the formation of eucrites. *Earth and Planetary Science Letters* **551**: 116544.

Moynier, F., W. Dai, T. Yokoyama, Y. Hu, M. Paquet, Y. Abe, J. Aléon, C. M. O. D. Alexander, S. Amari, Y. Amelin, K. I. Bajo and et al. (2022). The Solar System calcium isotopic composition inferred from Ryugu samples. *Geochemical Perspectives Letters* **24**: 1-6.

Moynier, F., J. Foriel, A. S. Shaw and M. L. Borgne (2017). Distribution of Zn isotopes during Alzheimer's disease. *Geochemical Perspectives Letters* **3**: 142-150.

Moynier, F., T. Fujii, A. S. Shaw and M. Le Borgne (2013). Heterogeneous distribution of natural zinc isotopes in mice†. *Metallomics* **5**: 693-699.

Moynier, F., T. Fujii and P. Telouk (2009). Mass-independent isotopic fractionation of tin in chemical exchange reaction using a crown ether. *Analytica Chimica Acta* **632**: 234-239.

Moynier, F., Y. Hu, W. Dai, E. Kubik, B. Mahan and J. Moureau (2021). Potassium isotopic composition of seven widely available biological standards using collision cell (CC)-MC-ICP-MS. *Journal of Analytical Atomic Spectrometry* **36**: 2444-2448.

Moynier, F., Y. Hu, K. Wang, Y. Zhao, Y. Gérard, Z. Deng, J. Moureau, W. Li, J. I. Simon and F.-Z. Teng (2021). Potassium isotopic composition of various samples using a dual-path collision cell-capable multiple-collector inductively coupled plasma mass spectrometer, Nu instruments Sapphire. *Chemical Geology* **571**: 120144.

Murphy, K. E., S. E. Long, M. S. Rearick and Ö. S. Ertas (2002). The accurate determination of potassium and calcium using isotope dilution inductively coupled "cold" plasma mass spectrometry. *Journal of Analytical Atomic Spectrometry* **17**: 469-477.

Nebel, O., K. Mezger, E. E. Scherer and C. Münker (2005). High precision determinations of $^{87}Rb/^{85}Rb$ in geologic materials by MC-ICP-MS. *International Journal of Mass Spectrometry* **246**: 10-18.

Nebel, O., K. Mezger and W. van Westrenen (2011). Rubidium isotopes in primitive chondrites: Constraints on Earth's volatile element depletion and lead isotope evolution. *Earth and Planetary Science Letters* **305**: 309-316.

Nelms, S. M. (2005). Inductively coupled plasma mass spectrometry handbook, CRC press.

Newman, K. (2012). Effects of the sampling interface in MC-ICP-MS: Relative elemental sensitivities and non-linear mass dependent fractionation of Nd isotopes. *Journal of Analytical Atomic Spectrometry* **27**: 63-70.

Newman, K., P. A. Freedman, J. Williams, N. S. Belshaw and A. N. Halliday (2009). High sensitivity skimmers and non-linear mass dependent fractionation in ICP-MS. *Journal of Analytical Atomic Spectrometry* **24**: 742-751.

Nie, N. X., X.-Y. Chen, T. Hopp, J. Y. Hu, Z. J. Zhang, F.-Z. Teng, A. Shahar and N. Dauphas (2021). Imprint of chondrule formation on the K and Rb isotopic compositions of carbonaceous meteorites. *Science Advances* **7**: eabl3929.

Nie, N. X., X.-Y. Chen, Z. J. Zhang, J. Y. Hu, W. Liu, F. L. H. Tissot, F.-Z. Teng, A. Shahar and N. Dauphas (2023). Rubidium and potassium isotopic variations in chondrites and Mars: Accretion signatures and planetary overprints. *Geochimica et Cosmochimica Acta* **344**: 207-229.

Nie, N. X. and N. Dauphas (2019). Vapor drainage in the protolunar disk as the cause for the depletion in volatile elements of the Moon. *The Astrophysical Journal Letters* **884**: L48.

Nielsen, S. G., J. D. Owens and T. J. Horner (2016). Analysis of high-precision vanadium isotope ratios by medium resolution MC-ICP-MS. *Journal of Analytical Atomic Spectrometry* **31**: 531-536.

Nielsen, S. G., J. Prytulak and A. N. Halliday (2011). Determination of precise and accurate $^{51}V/^{50}V$ isotope ratios by MC-ICP-MS, Part 1: Chemical separation of vanadium and mass spectrometric protocols. *Geostandards and Geoanalytical Research* **35**: 293-306.

Nielsen, S. G., M. Rehkämper, J. Baker and A. N. Halliday (2004). The precise and accurate determination of thallium isotope compositions and concentrations for water samples by MC-ICPMS. *Chemical Geology* **204**: 109-124.

Nier, A. O. (1950). A Redetermination of the Relative Abundances of the Isotopes of Carbon, Nitrogen, Oxygen, Argon, and Potassium. *Physical Review* **77**: 789-793.

Niu, H. and R. S. Houk (1994). Langmuir probe measurements of the ion extraction process in inductively coupled plasma mass spectrometry-I. spatially resolved determination of

electron density and electron temperature. *Spectrochimica Acta Part B: Atomic Spectroscopy* **49**: 1283-1303.

Niu, H. and R. S. Houk (1996). Fundamental aspects of ion extraction in inductively coupled plasma mass spectrometry. *Spectrochimica Acta Part B: Atomic Spectroscopy* **51**: 779-815.

Norman, M., V. Bennett, M. McCulloch and L. Kinsley (2002). Osmium isotopic compositions by vapor phase sample introduction using a multi-collector ICP-MS. *Journal of Analytical Atomic Spectrometry* **17**: 1394-1397.

Nozaki, T., K. Suzuki, G. Ravizza, J.-I. Kimura and Q. Chang (2012). A method for rapid determination of Re and Os isotope compositions using ID-MC-ICP-MS combined with the sparging method. *Geostandards and Geoanalytical Research* **36**: 131-148.

Nyquist, H. (1928). Thermal Agitation of Electric Charge in Conductors. *Physical Review* **32**: 110-113.

Ohls, K. and B. Bogdain (2016). History of inductively coupled plasma atomic emission spectral analysis: from the beginning up to its coupling with mass spectrometry. *Journal of Analytical Atomic Spectrometry* **31**: 22-31.

Ohno, T. and T. Hirata (2007). Simultaneous determination of mass-dependent isotopic fractionation and radiogenic isotope variation of strontium in geochemical samples by multiple collector-ICP-mass spectrometry. *Analytical Sciences* **23**: 1275-1280.

Ohno, T. and T. Hirata (2013). Determination of mass-dependent isotopic fractionation of cerium and neodymium in geochemical samples by MC-ICPMS. *Analytical Sciences* **29**: 47-53.

Ohta, J., T. Nozaki, H. Sato, K. Ashida and Y. Kato (2022). A precise and accurate analytical method for determination of osmium isotope ratios at the 1–15 pg level by using a MC-ICP-MS equipped with sparging introduction and high-sensitivity discrete dynode-type ion-counting detectors. *Journal of Analytical Atomic Spectrometry* **37**: 1600-1610.

Olesik, J. W. (2014). 15.17 - Inductively Coupled Plasma Mass Spectrometers. Treatise on Geochemistry (Second Edition). H. D. Holland and K. K. Turekian. Oxford, Elsevier**:** 309-336.

Olesik, J. W., J. A. Hartshorne, N. Casey, E. Linard and J. R. Dettman (2021). Further insight into analyte transport processes and water vapor, aerosol loading in ICP-OES and ICP-MS. *Spectrochimica Acta Part B: Atomic Spectroscopy* **176**: 106038.

Olesik, J. W., J. A. Kinzer and B. Harkleroad (1994). Inductively Coupled Plasma Optical Emission Spectrometry Using Nebulizers with Widely Different Sample Consumption Rates. *Analytical Chemistry* **66**: 2022-2030.

Onyett, I. J., M. Schiller, G. V. Makhatadze, Z. Deng, A. Johansen and M. Bizzarro (2023). Silicon isotope constraints on terrestrial planet accretion. *Nature* **619**: 539-544.

Ostrander, C. M., S. G. Nielsen, J. D. Owens, B. Kendall, G. W. Gordon, S. J. Romaniello and A. D. Anbar (2019). Fully oxygenated water columns over continental shelves before the Great Oxidation Event. *Nature Geoscience* **12**: 186-191.

Owen, P. L. and C. K. Thornhill (1948). The flow in an axially-symmetric supersonic jet from a nearly-sonic orifice into a vacuum.

Paquet, M., F. Moynier, T. Yokoyama, W. Dai, Y. Hu, Y. Abe, J. Aléon, C. M. O'D. Alexander, S. Amari, Y. Amelin, K.-i. Bajo, M. Bizzarro, A. Bouvier, R. W. Carlson, M. Chaussidon, B.-G. Choi, N. Dauphas, A. M. Davis, T. Di Rocco, W. Fujiya, R. Fukai, I. Gautam, M. K. Haba, Y. Hibiya, H. Hidaka, H. Homma, P. Hoppe, G. R. Huss, K. Ichida, T. Iizuka, T. R. Ireland, A. Ishikawa, M. Ito, S. Itoh, N. Kawasaki, N. T. Kita, K. Kitajima, T. Kleine, S.

Komatani, A. N. Krot, M.-C. Liu, Y. Masuda, K. D. McKeegan, M. Morita, K. Motomura, I. Nakai, K. Nagashima, D. Nesvorný, A. N. Nguyen, L. Nittler, M. Onose, A. Pack, C. Park, L. Piani, L. Qin, S. S. Russell, N. Sakamoto, M. Schönbächler, L. Tafla, H. Tang, K. Terada, Y. Terada, T. Usui, S. Wada, M. Wadhwa, R. J. Walker, K. Yamashita, Q.-Z. Yin, S. Yoneda, E. D. Young, H. Yui, A.-C. Zhang, T. Nakamura, H. Naraoka, T. Noguchi, R. Okazaki, K. Sakamoto, H. Yabuta, M. Abe, A. Miyazaki, A. Nakato, M. Nishimura, T. Okada, T. Yada, K. Yogata, S. Nakazawa, T. Saiki, S. Tanaka, F. Terui, Y. Tsuda, S.-i. Watanabe, M. Yoshikawa, S. Tachibana and H. Yurimoto (2022). Contribution of Ryugu-like material to Earth's volatile inventory by Cu and Zn isotopic analysis. *Nature Astronomy*.

Paquet, M., P. A. Sossi and F. Moynier (2023). Origin and abundances of volatiles on Mars from the zinc isotopic composition of Martian meteorites. *Earth and Planetary Science Letters* **611**: 118126.

Paul, W. and H. Steinwedel (1953). Notizen: Ein neues massenspektrometer ohne magnetfeld. *Zeitschrift für Naturforschung A* **8**: 448-450.

Payne, J. L., A. V. Turchyn, A. Paytan, D. J. DePaolo, D. J. Lehrmann, M. Yu and J. Wei (2010). Calcium isotope constraints on the end-Permian mass extinction. *Proceedings of the National Academy of Sciences* **107**: 8543-8548.

Petibon, C. M., H. P. Longerich, I. Horn and M. N. Tubrett (2002). Neon inductively coupled plasma for laser ablation-inductively coupled plasma-mass spectrometry. *Applied Spectroscopy* **56**: 658-664.

Pfeifer, M., N. S. Lloyd, S. T. M. Peters, F. Wombacher, B. M. Elfers, T. Schulz and C. Münker (2017). Tantalum isotope ratio measurements and isotope abundances determined by MC-ICP-MS using amplifiers equipped with 1010, 1012 and 1013 Ohm resistors. *Journal of Analytical Atomic Spectrometry* **32**: 130-143.

Plucker, J. and J. W. Hittorf (1865). I. On the spectra of ignited gases and vapours, with especial regard to the different spectra of the same elementary gaseous substance. *Philosophical Transactions of the Royal Society of London* **155**: 1-29.

Pogge von Strandmann, P. A. E., M. T. Jones, A. J. West, M. J. Murphy, E. W. Stokke, G. Tarbuck, D. J. Wilson, C. R. Pearce and D. N. Schmidt (2021). Lithium isotope evidence for enhanced weathering and erosion during the Paleocene-Eocene Thermal Maximum. *Science Advances* **7**: eabh4224.

Pogge von Strandmann, P. A. E., E. E. Stüeken, T. Elliott, S. W. Poulton, C. M. Dehler, D. E. Canfield and D. C. Catling (2015). Selenium isotope evidence for progressive oxidation of the Neoproterozoic biosphere. *Nature Communications* **6**: 10157.

Poitrasson, F., A. N. Halliday, D.-C. Lee, S. Levasseur and N. Teutsch (2004). Iron isotope differences between Earth, Moon, Mars and Vesta as possible records of contrasted accretion mechanisms. *Earth and Planetary Science Letters* **223**: 253-266.

Powell, M. J., D. W. Boomer and R. J. McVicars (1986). Introduction of gaseous hydrides into an inductively coupled plasma mass spectrometer. *Analytical Chemistry* **58**: 2864-2867.

Pringle, E. A. and F. Moynier (2017). Rubidium isotopic composition of the Earth, meteorites, and the Moon: Evidence for the origin of volatile loss during planetary accretion. *Earth and Planetary Science Letters* **473**: 62-70.

Pringle, E. A., F. Moynier, P. Beck, R. Paniello and D. C. Hezel (2017). The origin of volatile element depletion in early solar system material: Clues from Zn isotopes in chondrules. *Earth and Planetary Science Letters* **468**: 62-71.

Prytulak, J., S. G. Nielsen and A. N. Halliday (2011). Determination of precise and accurate $^{51}V/^{50}V$ isotope ratios by multi-collector ICP-MS, Part 2: Isotopic composition of six reference materials plus the Allende chondrite and verification tests. *Geostandards and Geoanalytical Research* **35**: 307-318.

Qu, R. and G. Han (2023). Potassium isotopes of fertilizers as potential markers of anthropogenic input in ecosystems. *Environmental Chemistry Letters* **21**: 41-45.

Rademacher, L. K., C. C. Lundstrom, T. M. Johnson, R. A. Sanford, J. Zhao and Z. Zhang (2006). Experimentally determined uranium isotope fractionation during reduction of hexavalent U by bacteria and zero valent iron. *Environmental Science & Technology* **40**: 6943-6948.

Reed, T. B. (1961). Growth of refractory crystals using the induction plasma torch. *Journal of Applied Physics* **32**: 2534-2535.

Reed, T. B. (1961). Induction‐Coupled Plasma Torch. *Journal of Applied Physics* **32**: 821-824.

Rehkämper, M. and A. N. Halliday (1999). The precise measurement of Tl isotopic compositions by MC-ICPMS: Application to the analysis of geological materials and meteorites. *Geochimica et Cosmochimica Acta* **63**: 935-944.

Ripperger, S. and M. Rehkämper (2007). Precise determination of cadmium isotope fractionation in seawater by double spike MC-ICPMS. *Geochimica et Cosmochimica Acta* **71**: 631-642.

Robin, J. P., J. M. Mermet, M. H. Abdallah, A. Batal and C. Trassy (1982). Role of plasma gas in emission spectroscopy. Recent Advances in Analytical Spectroscopy. K. Fuwa, Pergamon**:** 75-82.

Rouxel, O., A. Galy and H. Elderfield (2006). Germanium isotopic variations in igneous rocks and marine sediments. *Geochimica et Cosmochimica Acta* **70**: 3387-3400.

Rouxel, O., J. Ludden, J. Carignan, L. Marin and Y. Fouquet (2002). Natural variations of Se isotopic composition determined by hydride generation multiple collector inductively coupled plasma mass spectrometry. *Geochimica et Cosmochimica Acta* **66**: 3191-3199.

Rouxel, O., J. Ludden and Y. Fouquet (2003). Antimony isotope variations in natural systems and implications for their use as geochemical tracers. *Chemical Geology* **200**: 25-40.

Rowan, J. T. and R. S. Houk (1989). Attenuation of polyatomic ion interferences in inductively coupled plasma mass spectrometry by gas-phase collisions. *Applied Spectroscopy* **43**: 976-980.

Rudge, J. F., B. C. Reynolds and B. Bourdon (2009). The double spike toolbox. *Chemical Geology* **265**: 420-431.

Saji, N. S., D. Wielandt, C. Paton and M. Bizzarro (2016). Ultra-high-precision Nd-isotope measurements of geological materials by MC-ICPMS. *Journal of Analytical Atomic Spectrometry* **31**: 1490-1504.

Sakata, K. i. and K. Kawabata (1994). Reduction of fundamental polyatomic ions in inductively coupled plasma mass spectrometry. *Spectrochimica Acta Part B: Atomic Spectroscopy* **49**: 1027-1038.

Savage, P., M. Boyet and F. Moynier (2014). Zinc isotope anomalies in bulk chondrites. 77th Annual Meeting of the Meteoritical Society.

Savage, P. S., F. Moynier and M. Boyet (2022). Zinc isotope anomalies in primitive meteorites identify the outer solar system as an important source of Earth's volatile inventory. *Icarus* **386**: 115172.

Scheffler, G. L. and D. Pozebon (2014). Advantages, drawbacks and applications of mixed Ar–N_2 sources in inductively coupled plasma-based techniques: An overview. *Analytical Methods* **6**: 6170-6182.

Schiller, M., M. Bizzarro and V. A. Fernandes (2018). Isotopic evolution of the protoplanetary disk and the building blocks of Earth and the Moon. *Nature* **555**: 507-510.

Schiller, M., M. Bizzarro and J. Siebert (2020). Iron isotope evidence for very rapid accretion and differentiation of the proto-Earth. *Science Advances* **6**: eaay7604.

Schilling, K., A. Basu, A. Kaplan and W. T. Perkins (2021). Metal distribution, bioavailability and isotope variations in polluted soils from Lower Swansea Valley, UK. *Environmental Geochemistry and Health* **43**: 2899-2912.

Schilling, K., A. L. Harris, A. N. Halliday, C. J. Schofield, H. Sheldon, S. Haider and F. Larner (2022). Investigations on zinc isotope fractionation in breast cancer tissue using in vitro cell culture uptake-efflux experiments. *Frontiers in Medicine* **8**.

Schilling, K., R. E. T. Moore, K. V. Sullivan, M. S. Capper, M. Rehkämper, K. Goddard, C. Ion, R. C. Coombes, L. Vesty-Edwards, A. D. Lamb, A. N. Halliday and F. Larner (2021). Zinc stable isotopes in urine as diagnostic for cancer of secretory organs. *Metallomics* **13**.

Schoenberg, R., T. F. Nägler and J. D. Kramers (2000). Precise Os isotope ratio and Re–Os isotope dilution measurements down to the picogram level using multicollector inductively coupled plasma mass spectrometry. *International Journal of Mass Spectrometry* **197**: 85-94.

Schoenberg, R., S. Zink, M. Staubwasser and F. von Blanckenburg (2008). The stable Cr isotope inventory of solid Earth reservoirs determined by double spike MC-ICP-MS. *Chemical Geology* **249**: 294-306.

Schönbächler, M., M. Rehkämper, D.-C. Lee and A. N. Halliday (2004). Ion exchange chromatography and high precision isotopic measurements of zirconium by MC-ICP-MS. *Analyst* **129**: 32-37.

Sesi, N. N., A. Mackenzie, K. E. Shanks, P. Yang and G. M. Hieftje (1994). Fundamental studies of mixed-gas inductively coupled plasmas. *Spectrochimica Acta Part B: Atomic Spectroscopy* **49**: 1259-1282.

Shalev, N., I. Segal, B. Lazar, I. Gavrieli, J. Fietzke, A. Eisenhauer and L. Halicz (2013). Precise determination of $\delta^{88/86}$Sr in natural samples by double-spike MC-ICP-MS and its TIMS verification. *Journal of Analytical Atomic Spectrometry* **28**: 940-944.

Sharp, B. L. (1988). Pneumatic nebulisers and spray chambers for inductively coupled plasma spectrometry. A review. Part 1. Nebulisers. *Journal of Analytical Atomic Spectrometry* **3**: 613-652.

She, J.-X., W. Li, S. An and Y. Cai (2023). High-precision double-spike Sn isotope analysis of geological materials by MC-ICP-MS. *Journal of Analytical Atomic Spectrometry* **38**: 142-155.

Shen, J., R. Yin, S. Zhang, T. J. Algeo, D. J. Bottjer, J. Yu, G. Xu, D. Penman, Y. Wang, L. Li, X. Shi, N. J. Planavsky, Q. Feng and S. Xie (2022). Intensified continental chemical weathering and carbon-cycle perturbations linked to volcanism during the Triassic–Jurassic transition. *Nature Communications* **13**: 299.

Siebert, C., T. F. Nägler and J. D. Kramers (2001). Determination of molybdenum isotope fractionation by double-spike multicollector inductively coupled plasma mass spectrometry. *Geochemistry, Geophysics, Geosystems* **2**.

Siebert, C., A. Ross and J. McManus (2006). Germanium isotope measurements of high-temperature geothermal fluids using double-spike hydride generation MC-ICP-MS. *Geochimica et Cosmochimica Acta* **70**: 3986-3995.

Sio, C. K. I., N. Dauphas, F.-Z. Teng, M. Chaussidon, R. T. Helz and M. Roskosz (2013). Discerning crystal growth from diffusion profiles in zoned olivine by in situ Mg–Fe isotopic analyses. *Geochimica et Cosmochimica Acta* **123**: 302-321.

Smith, F. G. and R. S. Houk (1990). Alleviation of polyatomic ion interferences for determination of chlorine isotope ratios by inductively coupled plasma mass spectrometry. *Journal of the American Society for Mass Spectrometry* **1**: 284-287.

Smith, F. G., D. R. Wiederin, R. S. Houk, C. B. Egan and R. E. Serfass (1991). Measurement of boron concentration and isotope ratios in biological samples by inductivey coupled plasma mass spectrometry with direct injection nebulization. *Analytica Chimica Acta* **248**: 229-234.

Steinmann, L. K., M. Oeser, I. Horn, H.-M. Seitz and S. Weyer (2019). In situ high-precision lithium isotope analyses at low concentration levels with femtosecond-LA-MC-ICP-MS. *Journal of Analytical Atomic Spectrometry* **34**: 1447-1458.

Steller, T., C. Burkhardt, C. Yang and T. Kleine (2022). Nucleosynthetic zinc isotope anomalies reveal a dual origin of terrestrial volatiles. *Icarus* **386**: 115171.

Stephens, J. A., M. N. Ducea, D. J. Killick and J. Ruiz (2021). Use of non-traditional heavy stable isotopes in archaeological research. *Journal of Archaeological Science* **127**: 105334.

Stephens, W. E. (1946). A Pulsed Mass Spectrometer with Time Disaersion. Proceedings of the American Physical Society, Cambridge, Phys. Rev.

Stirling, C. H., A. N. Halliday and D. Porcelli (2005). In search of live ^{247}Cm in the early solar system. *Geochimica et Cosmochimica Acta* **69**: 1059-1071.

Stüeken, E. E. (2017). Selenium isotopes as a biogeochemical proxy in deep time. *Reviews in Mineralogy and Geochemistry* **82**: 657-682.

Stüeken, E. E., R. Buick and A. D. Anbar (2015). Selenium isotopes support free O_2 in the latest Archean. *Geology* **43**: 259-262.

Sullivan, K. V., J. A. Kidder, T. P. Junqueira, F. Vanhaecke and M. I. Leybourne (2022). Emerging applications of high-precision Cu isotopic analysis by MC-ICP-MS. *Science of The Total Environment* **838**: 156084.

Sullivan, K. V., R. E. T. Moore and F. Vanhaecke (2023). The influence of physiological and lifestyle factors on essential mineral element isotopic compositions in the human body: implications for the design of isotope metallomics research. *Metallomics* **15**.

Sun, X., P. Andersson, M. Land, C. Humborg and C.-M. Mörth (2010). Stable silicon isotope analysis on nanomole quantities using MC-ICP-MS with a hexapole gas-collision cell. *Journal of Analytical Atomic Spectrometry* **25**: 156-162.

Tacail, T., S. Le Houedec and J. L. Skulan (2020). New frontiers in calcium stable isotope geochemistry: Perspectives in present and past vertebrate biology. *Chemical Geology* **537**: 119471.

Tan, S. H. and G. Horlick (1986). Background spectral features in inductively coupled plasma/mass spectrometry. *Applied Spectroscopy* **40**: 445-460.

Tanner, S. D. (1992). Space charge in ICP-MS: calculation and implications. *Spectrochimica Acta Part B: Atomic Spectroscopy* **47**: 809-823.

Tanner, S. D. (1995). Characterization of ionization and matrix suppression in inductively coupled 'cold' plasma mass spectrometry. *Journal of Analytical Atomic Spectrometry* **10**: 905-921.

Tanner, S. D., V. I. Baranov and D. R. Bandura (2002). Reaction cells and collision cells for ICP-MS: a tutorial review. *Spectrochimica Acta Part B: Atomic Spectroscopy* **57**: 1361-1452.

Tanner, S. D., L. M. Cousins and D. J. Douglas (1994). Reduction of space charge effects using a three-aperture gas dynamic vacuum interface for inductively coupled plasma-mass spectrometry. *Applied Spectroscopy* **48**: 1367-1372.

Tanner, S. D., D. J. Douglas and J. B. French (1994). Gas and Ion Dynamics of a Three-Aperture Vacuum Interface for Inductively Coupled Plasma-Mass Spectrometry. *Applied Spectroscopy* **48**: 1373-1378.

Tanner, S. D., M. Paul, S. A. Beres and E. R. Denoyer (1995). The application of cold plasma conditions for the determination of trace levels of Fe, Ca, K, Na, and Li by ICP-MS. *Atomic Spectroscopy* **16**: 16-18.

Taylor, H. E. (2001). Inductively coupled plasma-mass spectrometry: practices and techniques, Academic press.

Télouk, P., E. Albalat, B. Bourdon, F. Albarède and V. Balter (2023). Performance of the double-Wien filter of the Neoma MC-ICPMS/MS with an application to copper stable isotope compositions. *Journal of Analytical Atomic Spectrometry* **38**: 1973-1983.

Télouk, P., E. Albalat, T. Tacail, F. Arnaud-Godet and V. Balter (2022). Steady analyses of potassium stable isotopes using a Thermo Scientific Neoma MC-ICP-MS. *Journal of Analytical Atomic Spectrometry* **37**: 1259-1264.

Teng, F.-Z., N. Dauphas and R. T. Helz (2008). Iron Isotope Fractionation During Magmatic Differentiation in Kilauea Iki Lava Lake. *Science* **320**: 1620-1622.

Teng, F.-Z., N. Dauphas and J. M. Watkins (2017). Non-traditional stable isotopes.

Teng, F.-Z., W.-Y. Li, S. Ke, B. Marty, N. Dauphas, S. Huang, F.-Y. Wu and A. Pourmand (2010). Magnesium isotopic composition of the Earth and chondrites. *Geochimica et Cosmochimica Acta* **74**: 4150-4166.

Teng, F.-Z., W.-Y. Li, S. Ke, W. Yang, S.-A. Liu, F. Sedaghatpour, S.-J. Wang, K.-J. Huang, Y. Hu, M.-X. Ling, Y. Xiao, X.-M. Liu, X.-W. Li, H.-O. Gu, C. K. Sio, D. A. Wallace, B.-X. Su, L. Zhao, J. Chamberlin, M. Harrington and A. Brewer (2015). Magnesium Isotopic Compositions of International Geological Reference Materials. *Geostandards and Geoanalytical Research* **39**: 329-339.

Teng, F.-Z., M. Wadhwa and R. T. Helz (2007). Investigation of magnesium isotope fractionation during basalt differentiation: Implications for a chondritic composition of the terrestrial mantle. *Earth and Planetary Science Letters* **261**: 84-92.

Thomas, R. (2013). Practical guide to ICP-MS: a tutorial for beginners.

Thompson, M., B. Pahlavanpour, S. J. Walton and G. F. Kirkbright (1978). Simultaneous determination of trace concentrations of arsenic, antimony, bismuth, selenium and tellurium in aqueous solution by introduction of the gaseous hydrides into an inductively coupled plasma source for emission spectrometry. Part I. Preliminary studies. *Analyst* **103**: 568-579.

Thompson, M., B. Pahlavanpour, S. J. Walton and G. F. Kirkbright (1978). Simultaneous determination of trace concentrations of arsenic, antimony, bismuth, selenium and tellurium in aqueous solution by introduction of the gaseous hydrides into an inductively coupled plasma source for emission spectrometry. Part II. Interference studies. *Analyst* **103**: 705-713.

Thomson, J. J. (1897). Cathode Rays. *Philosophical Magazine* **44**: 293-316.

Thomson, J. J. (1912). XIX. Further experiments on positive rays. *The London, Edinburgh, and Dublin Philosophical Magazine and Journal of Science* **24**: 209-253.

Thomson, J. J. (1913). Bakerian Lecture: Rays of positive electricity. *Proceedings of the Royal Society of London. Series A* **89**: 1-20.

Tian, S., X. Ding, Y. Qi, F. Wu, Y. Cai, R. M. Gaschnig, Z. Xiao, W. Lv, R. L. Rudnick and F. Huang (2023). Dominance of felsic continental crust on Earth after 3 billion years ago is recorded by vanadium isotopes. *Proceedings of the National Academy of Sciences* **120**: e2220563120.

Tian, Z., T. Magna, J. M. D. Day, K. Mezger, E. E. Scherer, K. Lodders, R. C. Hin, P. Koefoed, H. Bloom and K. Wang (2021). Potassium isotope composition of Mars reveals a mechanism of planetary volatile retention. *Proceedings of the National Academy of Sciences* **118**: e2101155118.

Tissot, F. L. H. and N. Dauphas (2015). Uranium isotopic compositions of the crust and ocean: Age corrections, U budget and global extent of modern anoxia. *Geochimica et Cosmochimica Acta* **167**: 113-143.

Tissot, F. L. H., N. Dauphas and L. Grossman (2016). Origin of uranium isotope variations in early solar nebula condensates. *Science Advances* **2**: e1501400.

Todolí, J.-L. (2019). Atomic Mass Spectrometry | Inductively Coupled Plasma Mass spectrometry. Encyclopedia of Analytical Science (Third Edition). P. Worsfold, C. Poole, A. Townshend and M. Miró. Oxford, Academic Press**:** 209-217.

Todoli, J.-L. and J.-M. Mermet (2011). Liquid sample introduction in ICP spectrometry: A practical guide, Elsevier.

Todolí, J. L. and J. M. Mermet (2006). Sample introduction systems for the analysis of liquid microsamples by ICP-AES and ICP-MS. *Spectrochimica Acta Part B: Atomic Spectroscopy* **61**: 239-283.

Tomascak, P. B., R. W. Carlson and S. B. Shirey (1999). Accurate and precise determination of Li isotopic compositions by multi-collector sector ICP-MS. *Chemical Geology* **158**: 145-154.

Tomascak, P. B., F. Tera, R. T. Helz and R. J. Walker (1999). The absence of lithium isotope fractionation during basalt differentiation: new measurements by multicollector sector ICP-MS. *Geochimica et Cosmochimica Acta* **63**: 907-910.

Tompkins, H. G. D., L. J. Zieman, M. Ibañez-Mejia and F. L. H. Tissot (2020). Zirconium stable isotope analysis of zircon by MC-ICP-MS: methods and application to evaluating intra-crystalline zonation in a zircon megacryst. *Journal of Analytical Atomic Spectrometry* **35**: 1167-1186.

Trinquier, A., T. Elliott, D. Ulfbeck, C. Coath, A. N. Krot and M. Bizzarro (2009). Origin of Nucleosynthetic Isotope Heterogeneity in the Solar Protoplanetary Disk. *Science* **324**: 374-376.

Tsuno, K. and D. Ioanoviciu (2013). Early History of Wien Filters. Advances in Imaging and Electron Physics, Elsevier. **176:** 1-6.

Turner, P., T. Merren, J. Speakman, C. Haines, G. Holland and S. Tanner (1997). Interface studies in the ICP-MS spectrometer. *Special Publications of the Royal Society of Chemistry* **202**: 28-34.

Valente, S. E. and W. G. Schrenk (1970). The Design and Some Emission Characteristics of an Economical dc Arc Plasmajet Excitation Source for Solution Analysis. *Applied Spectroscopy* **24**: 197-205.

Van Acker, T., S. Theiner, E. Bolea-Fernandez, F. Vanhaecke and G. Koellensperger (2023). Inductively coupled plasma mass spectrometry. *Nature Reviews Methods Primers* **3**: 52.

van den Boorn, S. H. J. M., P. Z. Vroon, C. C. van Belle, B. van der Wagt, J. Schwieters and M. J. van Bergen (2006). Determination of silicon isotope ratios in silicate materials by high-resolution MC-ICP-MS using a sodium hydroxide sample digestion method. *Journal of Analytical Atomic Spectrometry* **21**: 734-742.

van der Velde-Koerts, T. and J. L. M. de Boer (1994). Minimization of spectral interferences in inductively coupled plasma mass spectrometry by simplex optimization and nitrogen addition to the aerosol carrier gas for multi-element environmental analysis. *Journal of Analytical Atomic Spectrometry* **9**: 1093-1098.

van Kooten, E. and F. Moynier (2019). Zinc isotope analyses of singularly small samples (<5 ng Zn): Investigating chondrule-matrix complementarity in Leoville. *Geochimica et Cosmochimica Acta* **261**: 248-268.

Vanhaecke, F. and P. Degryse (2012). Isotopic analysis: Fundamentals and applications using ICP‐MS, Wiley.

Vanhaecke, F., L. Moens, R. Dams and P. Taylor (1996). Precise measurement of isotope ratios with a double-focusing magnetic Sector ICP mass spectrometer. *Analytical Chemistry* **68**: 567-569.

Vanhaecke, F., M. van Holderbeke, L. Moens and R. Dams (1996). Evaluation of a commercially available microconcentric nebulizer for inductively coupled plasma mass spectrometry. *Journal of Analytical Atomic Spectrometry* **11**: 543-548.

Vervoort, J. D., P. J. Patchett, G. E. Gehrels and A. P. Nutman (1996). Constraints on early Earth differentiation from hafnium and neodymium isotopes. *Nature* **379**: 624-627.

Vervoort, J. D., P. J. Patchett, U. Söderlund and M. Baker (2004). Isotopic composition of Yb and the determination of Lu concentrations and Lu/Hf ratios by isotope dilution using MC-ICPMS. *Geochemistry, Geophysics, Geosystems* **5**.

Vestal, M. L. and J. H. Futrell (1974). Photodissociation of CH_3Cl^+ and CH_3Br^+ in a tandem quadrupole mass spectrometer. *Chemical Physics Letters* **28**: 559-561.

von Blanckenburg, F., N. von Wirén, M. Guelke, D. J. Weiss and T. D. Bullen (2009). Fractionation of metal stable isotopes by higher plants. *Elements* **5**: 375-380.

Von Zahn, U. and H. Tatarczyk (1964). Metastable molecule ions with lifetimes in the 100 μsec region. *Physics Letters* **12**: 190-191.

Wagatsuma, K. and K. Hirokawa (1989). Quenching mechanisms in argon-nitrogen or neon-nitrogen glow discharge plasmas. *Analytical Chemistry* **61**: 326-329.

Waight, T., J. Baker and B. Willigers (2002). Rb isotope dilution analyses by MC-ICPMS using Zr to correct for mass fractionation: towards improved Rb–Sr geochronology? *Chemical Geology* **186**: 99-116.

Walder, A. J. and P. A. Freedman (1992). Communication. Isotopic ratio measurement using a double focusing magnetic sector mass analyser with an inductively coupled plasma as an ion source. *Journal of Analytical Atomic Spectrometry* **7**: 571-575.

Walder, A. J., D. Koller, N. M. Reed, R. C. Hutton and P. A. Freedman (1993). Communication. Isotope ratio measurement by inductively coupled plasma multiple collector mass spectrometry incorporating a high efficiency nebulization system. *Journal of Analytical Atomic Spectrometry* **8**: 1037-1041.

Wang, B., F. Moynier and Y. Hu (2024). Rubidium isotopic compositions of angrites controlled by extensive evaporation and partial recondensation. *Proceedings of the National Academy of Sciences of the United States of America* **in press**.

Wang, B., F. Moynier, M. G. Jackson, F. Huang, X. Hu, S. Ari Halldórsson, W. Dai and G. Devos (2023). Rubidium isotopic fractionation during magmatic processes and the composition of the bulk silicate Earth. *Geochimica et Cosmochimica Acta* **354**: 38-50.

Wang, J., D.-M. Tang, B.-X. Su, Q.-H. Yuan, W.-J. Li, B.-Y. Gao, K.-Y. Chen, Z.-A. Bao and Y. Zhao (2022). High-precision iron isotopic measurements in low resolution using collision cell (CC)-MC-ICP-MS. *Journal of Analytical Atomic Spectrometry* **37**: 1869-1875.

Wang, J., D.-M. Tang, B.-X. Su, Q.-H. Yuan, W.-J. Li, B.-Y. Gao, K.-Y. Chen, Z.-A. Bao and Y. Zhao (2022). High-precision iron isotopic measurements in low resolution using collision cell (CC)-MC-ICP-MS. *Journal of Analytical Atomic Spectrometry*.

Wang, K. and S. B. Jacobsen (2016). An estimate of the Bulk Silicate Earth potassium isotopic composition based on MC-ICPMS measurements of basalts. *Geochimica et Cosmochimica Acta* **178**: 223-232.

Wang, K. and S. B. Jacobsen (2016). Potassium isotopic evidence for a high-energy giant impact origin of the Moon. *Nature* **538**: 487-490.

Wang, S.-J., W. Wang, J.-M. Zhu, Z. Wu, J. Liu, G. Han, F.-Z. Teng, S. Huang, H. Wu, Y. Wang, G. Wu and W. Li (2021). Nickel isotopic evidence for late-stage accretion of Mercury-like differentiated planetary embryos. *Nature Communications* **12**: 294.

Wang, X., Q. Amet, C. Fitoussi and B. Bourdon (2018). Tin isotope fractionation during magmatic processes and the isotope composition of the bulk silicate Earth. *Geochimica et Cosmochimica Acta* **228**: 320-335.

Wang, X., C. Fitoussi, B. Bourdon and Q. Amet (2017). A new method of Sn purification and isotopic determination with a double-spike technique for geological and cosmochemical samples. *Journal of Analytical Atomic Spectrometry* **32**: 1009-1019.

Wang, X., M. Viczian, A. Lasztity and R. M. Barnes (1988). Lead hydride generation for isotope analysis by inductively coupled plasma mass spectrometry. *Journal of Analytical Atomic Spectrometry* **3**: 821-827.

Wasserman, N. L. and T. M. Johnson (2020). Measurements of mass-dependent Te isotopic variation by hydride generation MC-ICP-MS. *Journal of Analytical Atomic Spectrometry* **35**: 307-319.

Weiss, D. J., M. Rehkämper, R. Schoenberg, M. McLaughlin, J. Kirby, P. G. C. Campbell, T. Arnold, J. Chapman, K. Peel and S. Gioia (2008). Application of Nontraditional Stable-Isotope Systems to the Study of Sources and Fate of Metals in the Environment. *Environmental Science & Technology* **42**: 655-664.

Wendt, R. H. and V. A. Fassel (1965). Induction-coupled plasma spectrometric excitation source. *Analytical Chemistry* **37**: 920-922.

Weyer, S., A. D. Anbar, A. Gerdes, G. W. Gordon, T. J. Algeo and E. A. Boyle (2008). Natural fractionation of $^{238}U/^{235}U$. *Geochimica et Cosmochimica Acta* **72**: 345-359.

Weyer, S. and D. A. Ionov (2007). Partial melting and melt percolation in the mantle: The message from Fe isotopes. *Earth and Planetary Science Letters* **259**: 119-133.

Weyer, S. and J. B. Schwieters (2003). High precision Fe isotope measurements with high mass resolution MC-ICPMS. *International Journal of Mass Spectrometry* **226**: 355-368.

Wiedenbeck, M., R. Bugoi, M. J. M. Duke, T. Dunai, J. Enzweiler, M. Horan, K. P. Jochum, K. Linge, J. Košler, S. Merchel, L. F. G. Morales, L. Nasdala, R. Stalder, P. Sylvester, U. Weis and A. Zoubir (2012). GGR Biennial Critical Review: Analytical Developments Since 2010. *Geostandards and Geoanalytical Research* **36**: 337-398.

Wiederhold, J. G. (2015). Metal stable isotope signatures as tracers in environmental geochemistry. *Environmental Science & Technology* **49**: 2606-2624.
Wien, W. (1898). Untersuchungen über die electrische entladung in verdünnten gasen. *Annalen der Physik* **301**: 440-452.
Wieser, M. E., J. R. De Laeter and M. D. Varner (2007). Isotope fractionation studies of molybdenum. *International Journal of Mass Spectrometry* **265**: 40-48.
Wieser, M. E. and J. B. Schwieters (2005). The development of multiple collector mass spectrometry for isotope ratio measurements. *International Journal of Mass Spectrometry* **242**: 97-115.
Wiley, W. C. and I. H. McLaren (1955). Time‐of‐Flight Mass Spectrometer with Improved Resolution. *Review of Scientific Instruments* **26**: 1150-1157.
Williams, H. M., C. A. McCammon, A. H. Peslier, A. N. Halliday, N. Teutsch, S. Levasseur and J.-P. Burg (2004). Iron Isotope Fractionation and the Oxygen Fugacity of the Mantle. *Science* **304**: 1656-1659.
Wolff, M. M. and W. E. Stephens (1953). A pulsed mass spectrometer with time dispersion. *Review of Scientific Instruments* **24**: 616-617.
Wombacher, F., M. Rehkämper, K. Mezger, A. Bischoff and C. Münker (2008). Cadmium stable isotope cosmochemistry. *Geochimica et Cosmochimica Acta* **72**: 646-667.
Wombacher, F., M. Rehkämper, K. Mezger and C. Münker (2003). Stable isotope compositions of cadmium in geological materials and meteorites determined by multiple-collector ICPMS. *Geochimica et Cosmochimica Acta* **67**: 4639-4654.
Wu, F., Y. Qi, H. Yu, S. Tian, Z. Hou and F. Huang (2016). Vanadium isotope measurement by MC-ICP-MS. *Chemical Geology* **421**: 17-25.
Yamazaki, E., S. Nakai, rsquo, Ich, T. Yokoyama, S. Ishihara and H. Tang (2013). Tin isotope analysis of cassiterites from Southeastern and Eastern Asia. *Geochemical Journal* **47**: 21-35.
Yang, L. (2009). Accurate and precise determination of isotopic ratios by MC-ICP-MS: A review. *Mass Spectrometry Reviews* **28**: 990-1011.
Yang, L., S. Tong, L. Zhou, Z. Hu, Z. Mester and J. Meija (2018). A critical review on isotopic fractionation correction methods for accurate isotope amount ratio measurements by MC-ICP-MS. *Journal of Analytical Atomic Spectrometry* **33**: 1849-1861.
Yin, Q., S. B. Jacobsen, K. Yamashita, J. Blichert-Toft, P. Télouk and F. Albarède (2002). A short timescale for terrestrial planet formation from Hf–W chronometry of meteorites. *Nature* **418**: 949-952.
Yin, R., X. Feng and W. Shi (2010). Application of the stable-isotope system to the study of sources and fate of Hg in the environment: A review. *Applied Geochemistry* **25**: 1467-1477.
Yost, R. A. (2022). The triple quadrupole: Innovation, serendipity and persistence. *Journal of Mass Spectrometry and Advances in the Clinical Lab* **24**: 90-99.
Yost, R. A. (2022). Why tandem mass spectrometry for trace analysis: Concepts of tandem analytical techniques. *Rapid Communications in Mass Spectrometry* **36**: e9310.
Yost, R. A. and C. G. Enke (1978). Selected ion fragmentation with a tandem quadrupole mass spectrometer. *Journal of the American Chemical Society* **100**: 2274-2275.
Yost, R. A. and C. G. Enke (1979). Triple quadrupole mass spectrometry for direct mixture analysis and structure elucidation. *Analytical Chemistry* **51**: 1251-1264.

Young, E. D., E. Tonui, C. E. Manning, E. Schauble and C. A. Macris (2009). Spinel–olivine magnesium isotope thermometry in the mantle and implications for the Mg isotopic composition of Earth. *Earth and Planetary Science Letters* **288**: 524-533.

Yu, T.-Y., T. M. H. Cheng, V. Kempter and F. W. Lampe (1972). Ionic reactions in monosilane. Radiation chemistry implications. *The Journal of Physical Chemistry* **76**: 3321-3330.

Yuan, H.-L., S. Gao, M.-N. Dai, C.-L. Zong, D. Günther, G. H. Fontaine, X.-M. Liu and C. Diwu (2008). Simultaneous determinations of U–Pb age, Hf isotopes and trace element compositions of zircon by excimer laser-ablation quadrupole and multiple-collector ICP-MS. *Chemical Geology* **247**: 100-118.

Yuan, W., J. B. Chen, J.-L. Birck, Z. Y. Yin, S. L. Yuan, H. M. Cai, Z. W. Wang, Q. Huang and Z. H. Wang (2016). Precise analysis of gallium isotopic composition by MC-ICP-MS. *Analytical Chemistry* **88**: 9606-9613.

Zhang, F., S. Xiao, B. Kendall, S. J. Romaniello, H. Cui, M. Meyer, G. J. Gilleaudeau, A. J. Kaufman and A. D. Anbar (2018). Extensive marine anoxia during the terminal Ediacaran Period. *Science Advances* **4**: eaan8983.

Zhang, H., F. Zhang, J.-b. Chen, D. H. Erwin, D. D. Syverson, P. Ni, M. Rampino, Z. Chi, Y.-f. Cai, L. Xiang, W.-q. Li, S.-A. Liu, R.-c. Wang, X.-d. Wang, Z. Feng, H.-m. Li, T. Zhang, H.-m. Cai, W. Zheng, Y. Cui, X.-k. Zhu, Z.-q. Hou, F.-y. Wu, Y.-g. Xu, N. Planavsky and S.-z. Shen (2021). Felsic volcanism as a factor driving the end-Permian mass extinction. *Science Advances* **7**: eabh1390.

Zhang, J., N. Dauphas, A. M. Davis, I. Leya and A. Fedkin (2012). The proto-Earth as a significant source of lunar material. *Nature Geoscience* **5**: 251-255.

Zhang, L. S. and S. M. Combs (1996). Using the installed spray chamber as a gas-liquid separator for the determination of germanium, arsenic, selenium, tin, antimony, tellurium and bismuth by hydride generation inductively coupled plasma mass spectrometry. *Journal of Analytical Atomic Spectrometry* **11**: 1043-1048.

Zhang, T., L. Zhou, L. Yang, Q. Wang, L.-p. Feng and Y.-s. Liu (2016). High precision measurements of gallium isotopic compositions in geological materials by MC-ICP-MS. *Journal of Analytical Atomic Spectrometry* **31**: 1673-1679.

Zhang, X.-Y., L.-H. Chen, X.-J. Wang, T. Hanyu, A. W. Hofmann, T. Komiya, K. Nakamura, Y. Kato, G. Zeng, W.-X. Gou and W.-Q. Li (2022). Zinc isotopic evidence for recycled carbonate in the deep mantle. *Nature Communications* **13**: 6085.

Zheng, X.-Y., X.-Y. Chen, W. Ding, Y. Zhang, S. Charin and Y. Gérard (2022). High precision analysis of stable potassium (K) isotopes by the collision cell MC-ICP-MS "Sapphire" and a correction method for concentration mismatch. *Journal of Analytical Atomic Spectrometry* **37**: 1273-1287.

Zhu, J.-M., T. M. Johnson, S. K. Clark and X.-K. Zhu (2008). High precision measurement of selenium isotopic composition by hydride generation multiple collector inductively coupled plasma mass spectrometry with a ^{74}Se-^{77}Se double spike. *Chinese Journal of Analytical Chemistry* **36**: 1385-1390.

Zhu, X.-K., R. K. O'Nions, Y. Guo and B. C. Reynolds (2000). Secular Variation of Iron Isotopes in North Atlantic Deep Water. *Science* **287**: 2000-2002.

Zirakparvar, N. A., B. Manard, C. Hexel, D. Dunlap, S. Metzger, D. Bostick, V. Bradley and B. Ticknor (2023). Faraday detector uranium isotope ratio measurement: Insights from solution- and laser ablation-based sampling methodologies on the Neoma MC-ICP-MS. *International Journal of Mass Spectrometry* **492**: 117114.

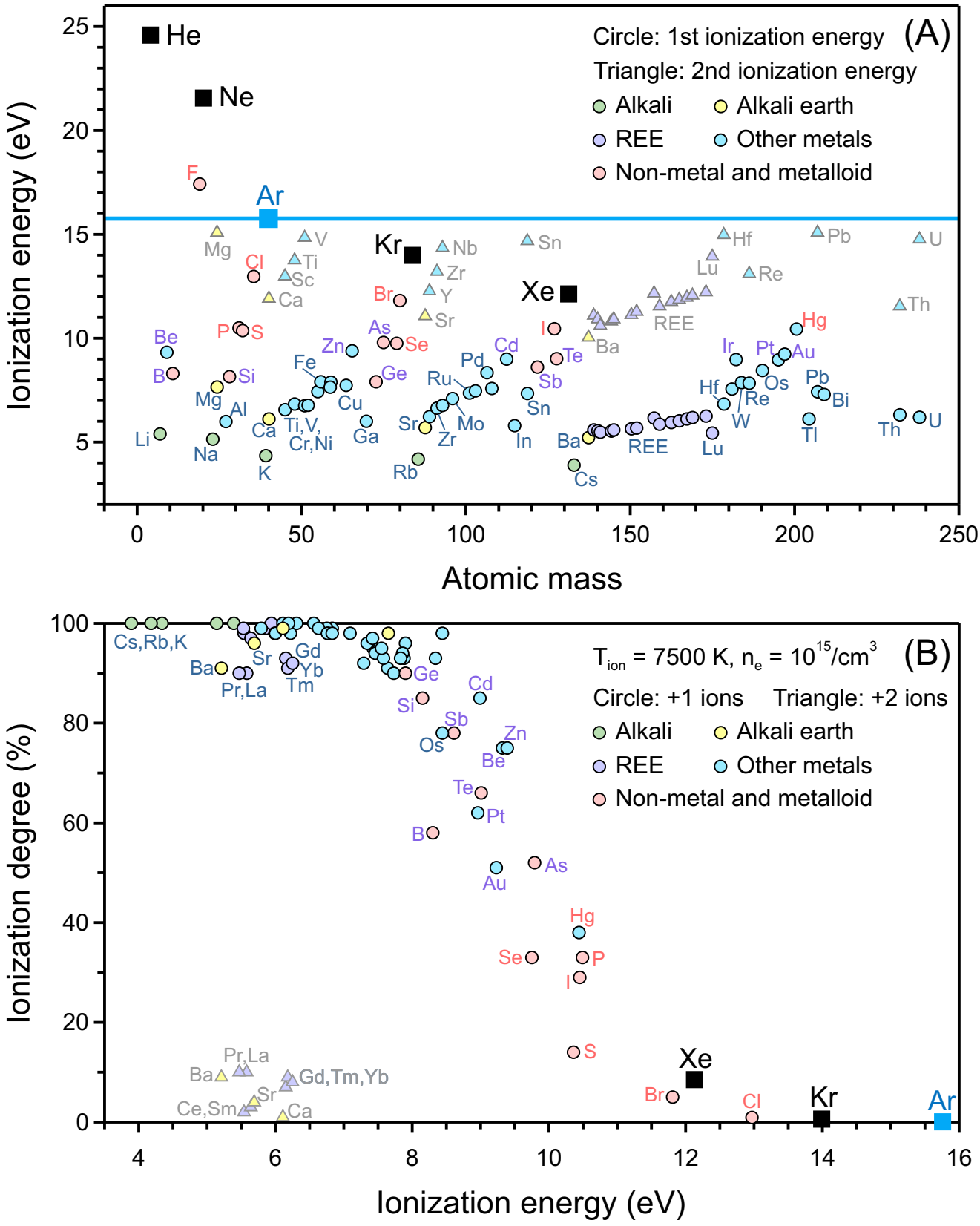
(A)
Circle: 1st ionization energy
Triangle: 2nd ionization energy
Alkali
Alkali earth
REE
Other metals
Non-metal and metalloid
He
Ne
Ar
Kr
Xe
Ionization energy (eV)
Atomic mass
(B)
T_{ion} = 7500 K, n_e = 10^{15}/cm^3
Circle: +1 ions
Triangle: +2 ions
Ionization degree (%)
Ionization energy (eV)

Fig. 1

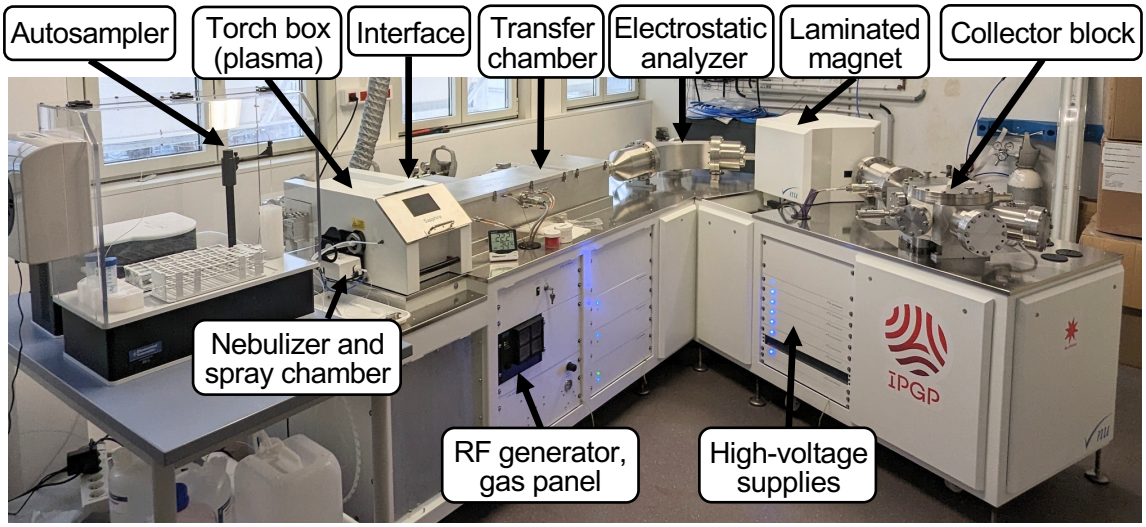
Autosampler
Torch box (plasma)
Interface
Transfer chamber
Electrostatic analyzer
Laminated magnet
Collector block
Nebulizer and spray chamber
RF generator, gas panel
High-voltage supplies
IPGP

Fig. 2

(A) Concentric nebulizer

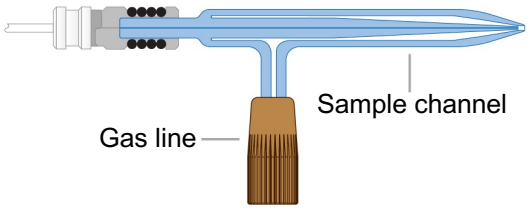

(B) Crossflow nebulizer

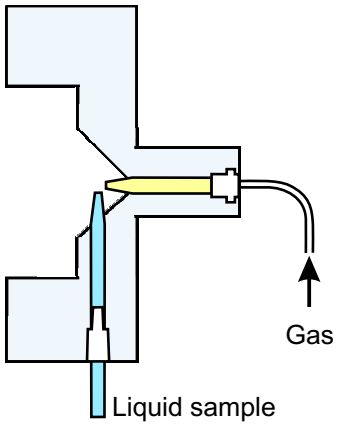

(C) Nebulizer transport efficiency

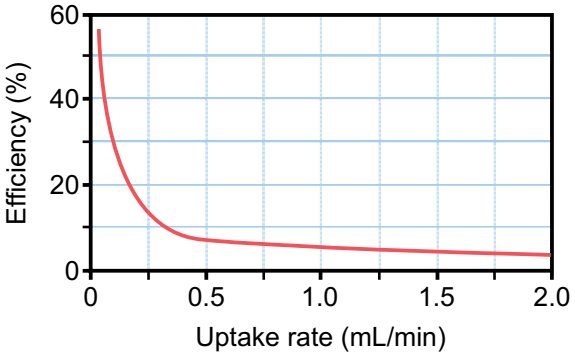

Fig. 3

(A) Cyclonic spray chamber

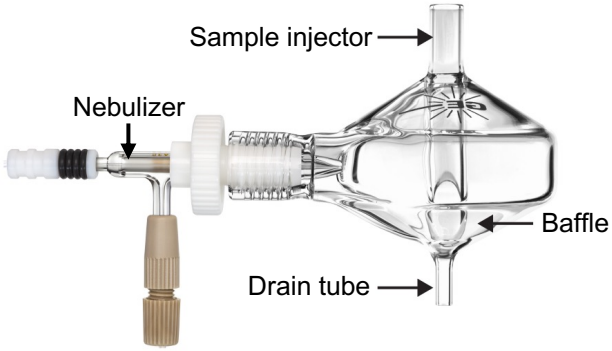

(B) Dual Scott/cyclonic spray chamber

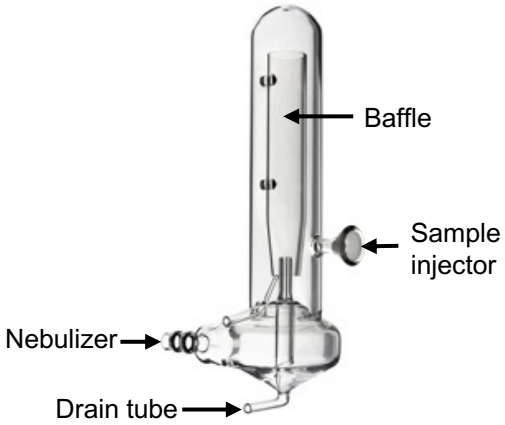

Fig. 4

(A) CETAC Aridus 3

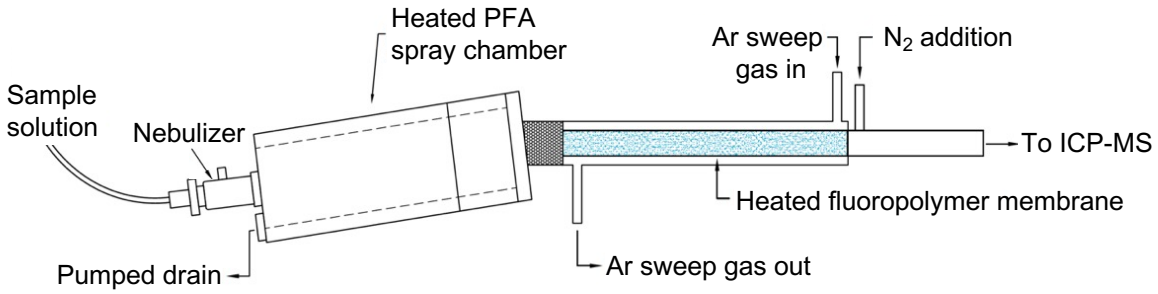

(B) ESI Apex Omega

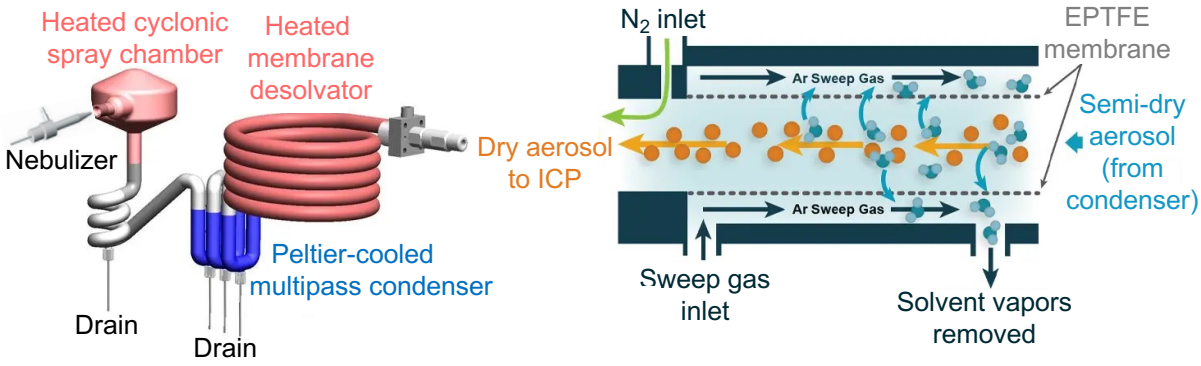

Fig. 5

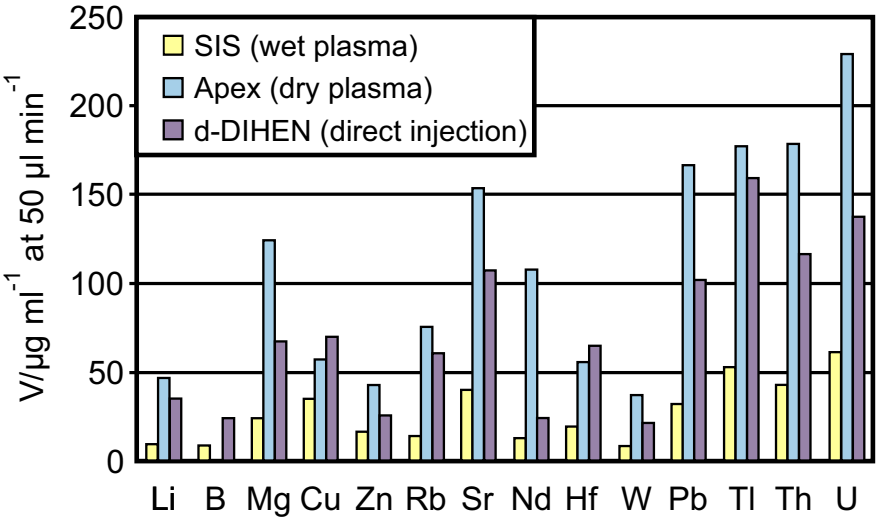
SIS (wet plasma)
Apex (dry plasma)
d-DIHEN (direct injection)
V/µg ml-1 at 50 µl min-1
250
200
150
100
50
0
Li
B
Mg
Cu
Zn
Rb
Sr
Nd
Hf
W
Pb
Tl
Th
U

Fig. 6

(a) Torch illustration

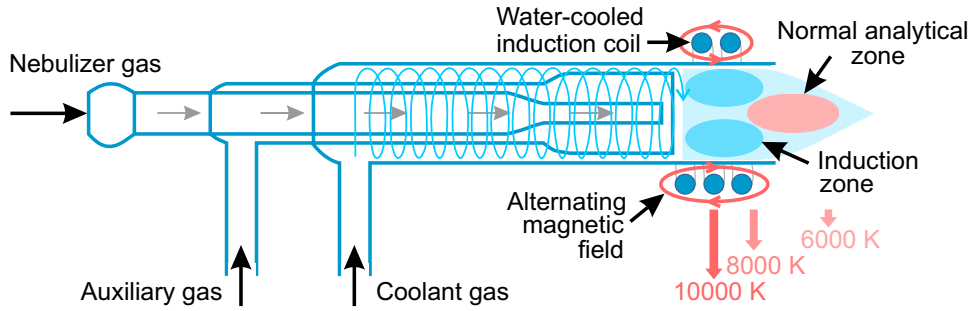

(b) Torch box configuration

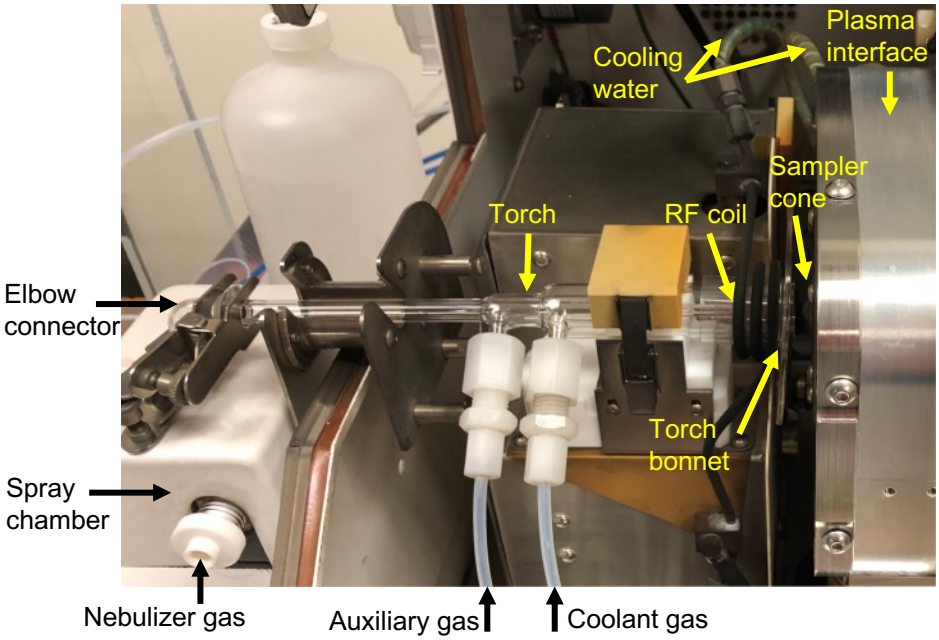

Fig. 7

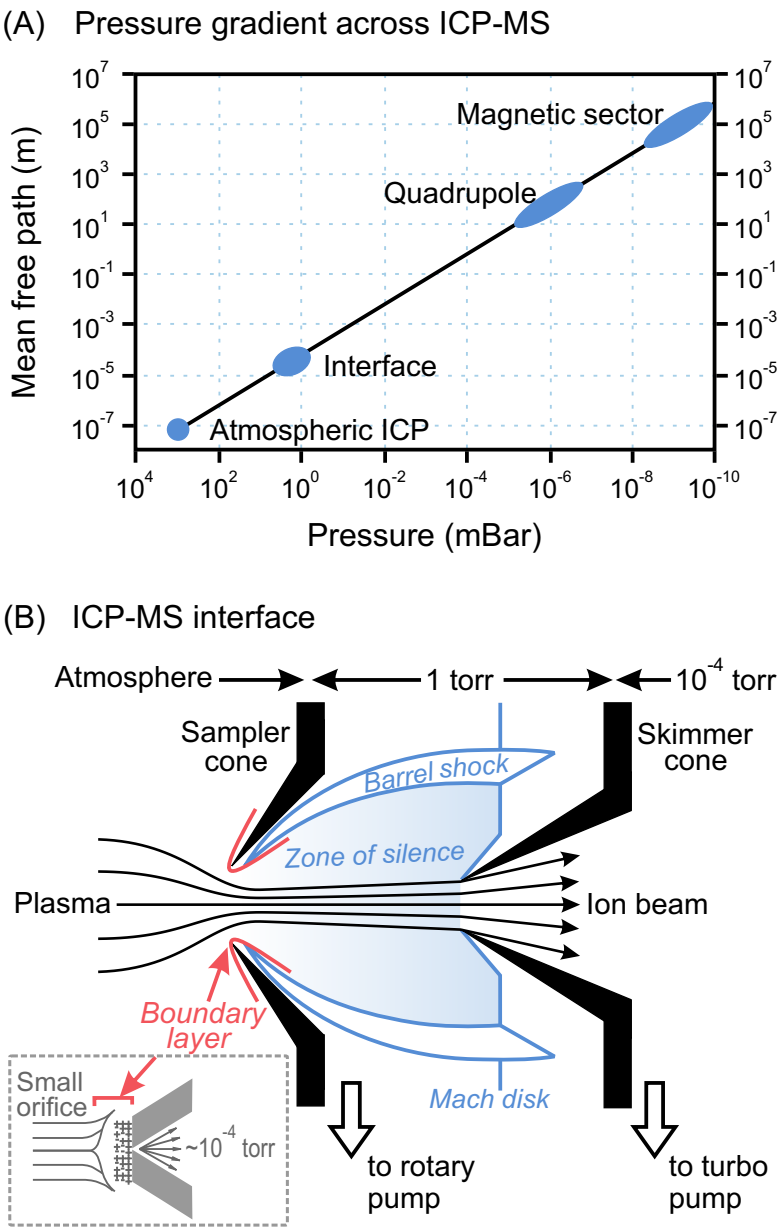
(A) Pressure gradient across ICP-MS
Mean free path (m)
Pressure (mBar)
Magnetic sector
Quadrupole
Interface
Atmospheric ICP
(B) ICP-MS interface
Atmosphere
1 torr
10-4 torr
Sampler cone
Skimmer cone
Barrel shock
Zone of silence
Plasma
Ion beam
Boundary layer
Small orifice
~10-4 torr
Mach disk
to rotary pump
to turbo pump

Fig. 8

(A) Increased dispersion of U isotopes

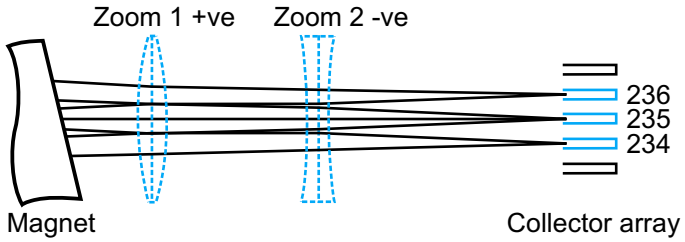

(B) Natural dispersion of Sr isotopes

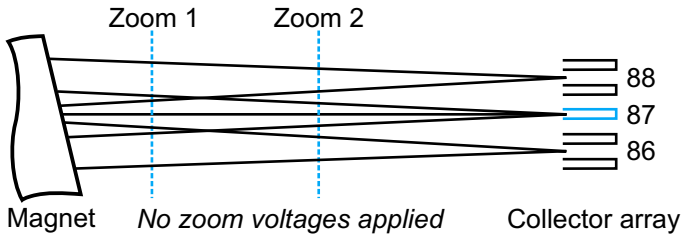

(C) Adjusted dispersion of Sr isotopes

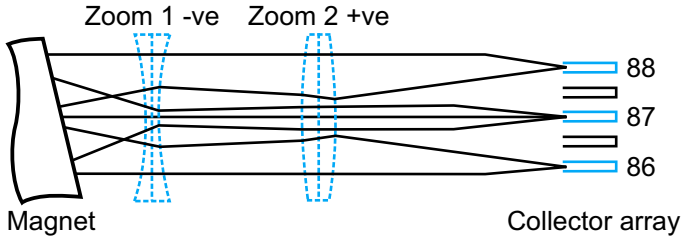

Fig. 9

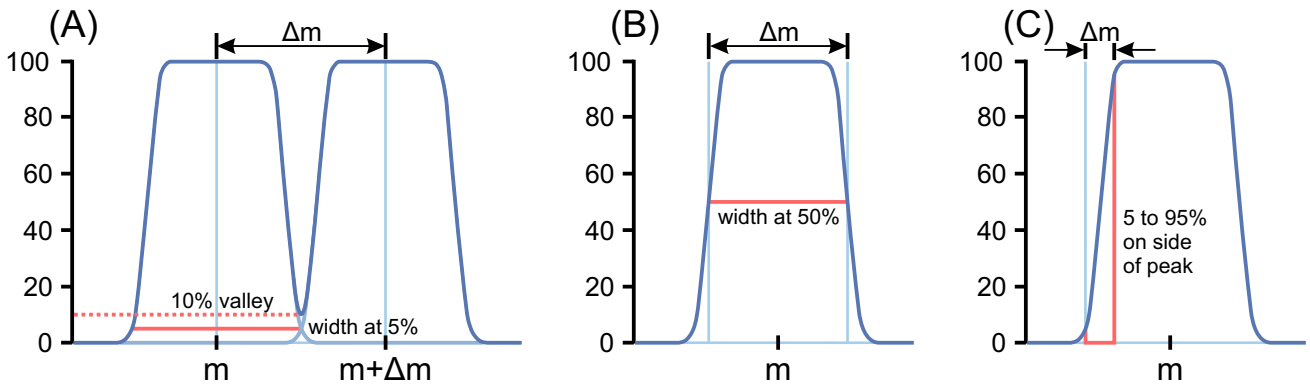
(A)
Δm
100
80
60
40
20
0
10% valley
width at 5%
m
m+Δm
(B)
Δm
100
80
60
40
20
0
width at 50%
m
(C)
Δm
100
80
60
40
20
0
5 to 95%
on side
of peak
m

Fig. 10

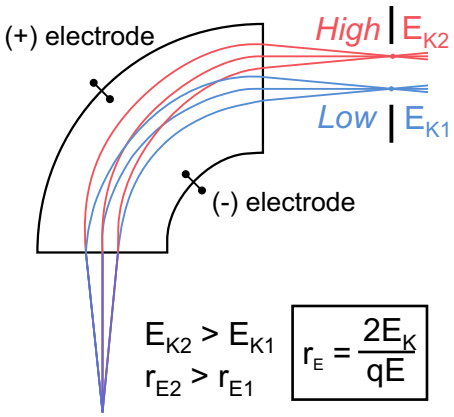
(+) electrode
High
E_{K2}
Low
E_{K1}
(-) electrode
$E_{K2} > E_{K1}$
$r_{E2} > r_{E1}$
$r_E = \frac{2E_K}{qE}$

Fig. 11

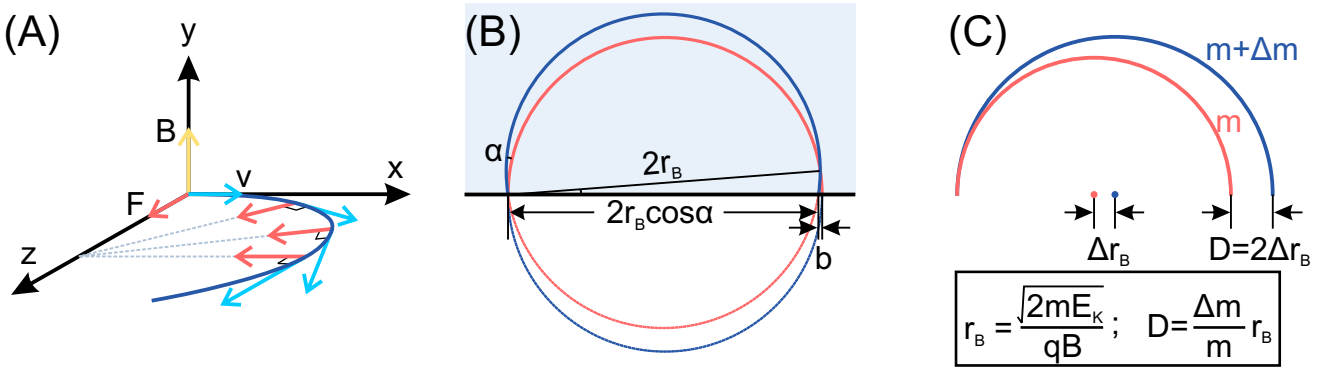

Fig. 12

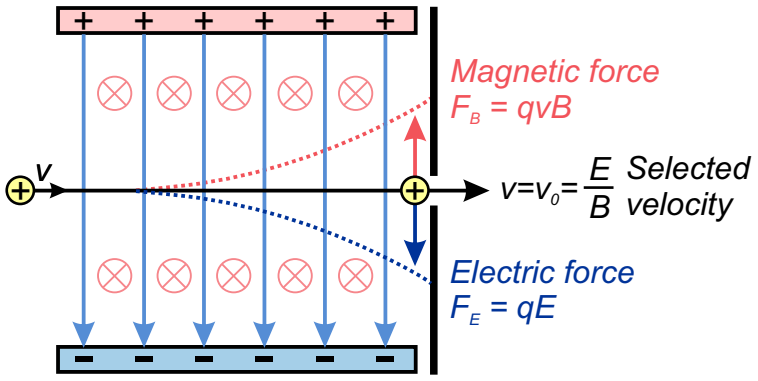
Magnetic force
$F_B = qvB$
v
$v=v_0=\frac{E}{B}$ Selected velocity
Electric force
$F_E = qE$

Fig. 13

(A) Mattauch-Herzog geometry

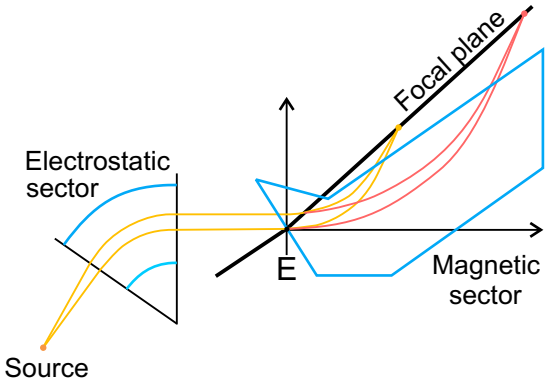

(B) Forward Nier-Johnson geometry

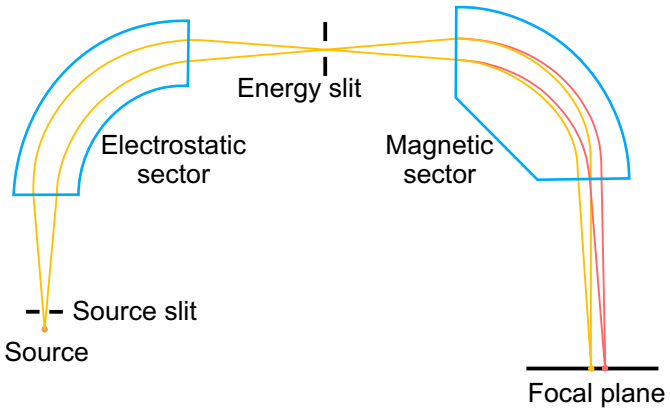

Fig. 14

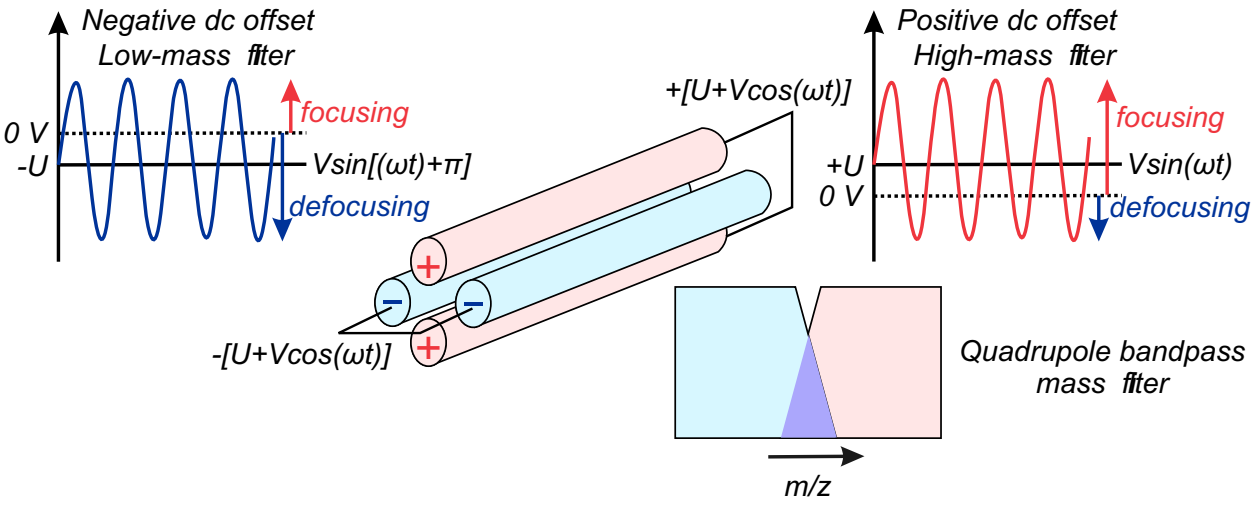
Negative dc offset
Low-mass filter
0 V
-U
focusing
Vsin[(ωt)+π]
defocusing
+[U+Vcos(ωt)]
-[U+Vcos(ωt)]
Positive dc offset
High-mass filter
+U
0 V
focusing
Vsin(ωt)
defocusing
Quadrupole bandpass
mass filter
m/z

Fig. 15

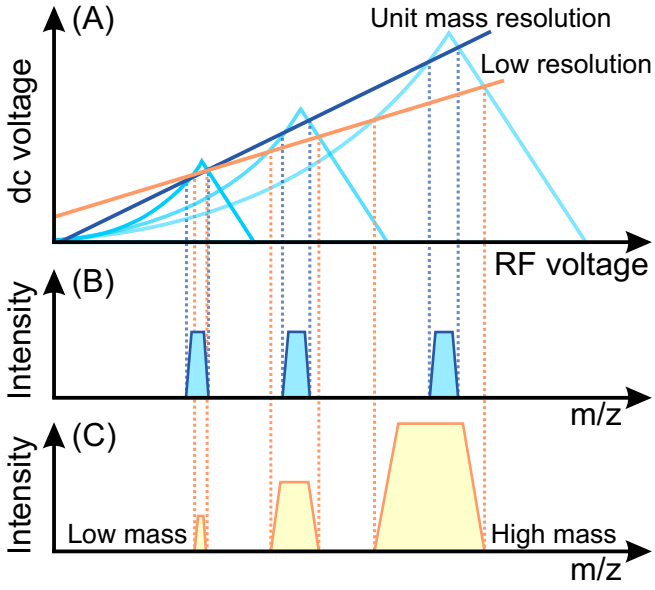
(A)
Unit mass resolution
Low resolution
dc voltage
RF voltage
(B)
Intensity
m/z
(C)
Intensity
Low mass
High mass
m/z

Fig. 16

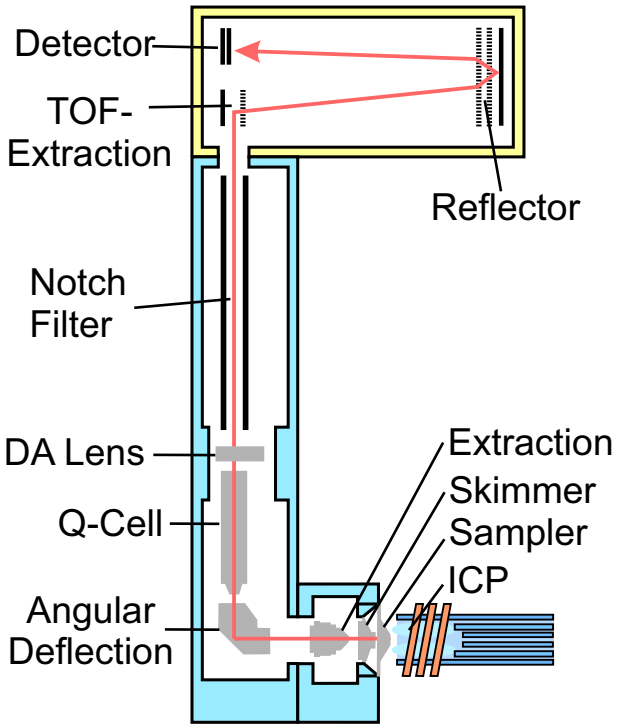
Detector
TOF-
Extraction
Reflector
Notch
Filter
DA Lens
Q-Cell
Angular
Deflection
Extraction
Skimmer
Sampler
ICP

Fig. 17

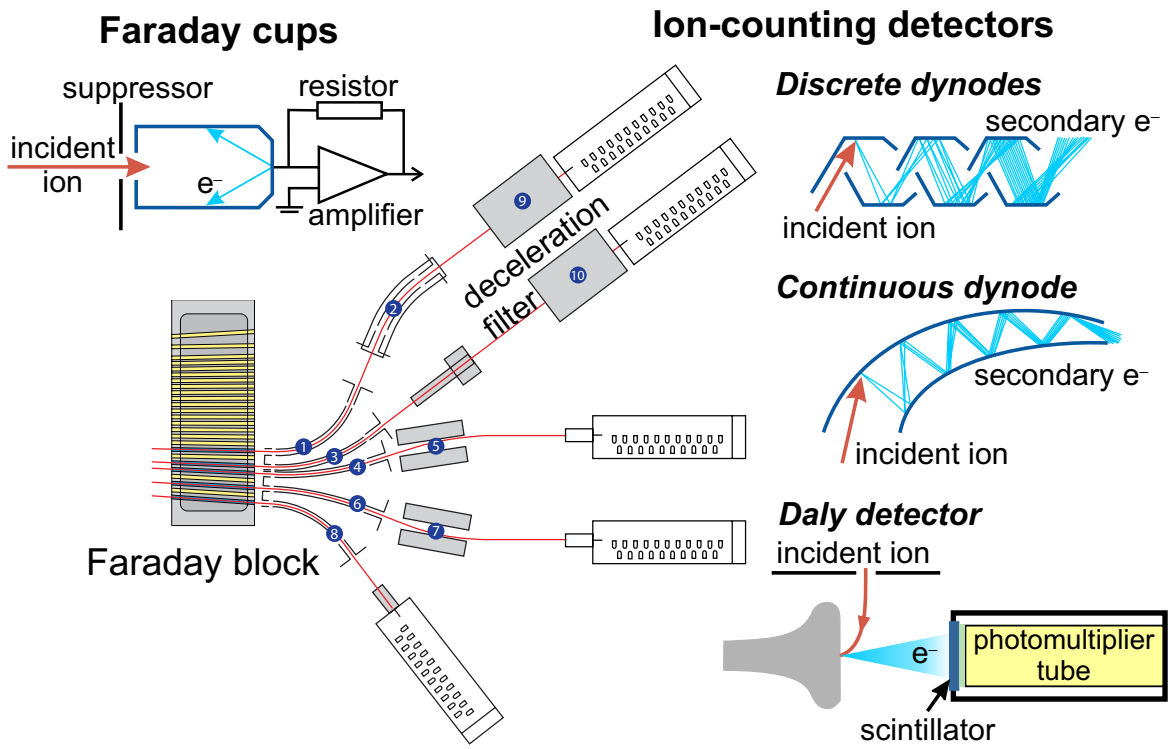
Faraday cups
suppressor
resistor
incident
ion
e⁻
amplifier
deceleration
filter
Faraday block
Ion-counting detectors
Discrete dynodes
secondary e⁻
incident ion
Continuous dynode
secondary e⁻
incident ion
Daly detector
incident ion
e⁻
photomultiplier
tube
scintillator

Fig. 18

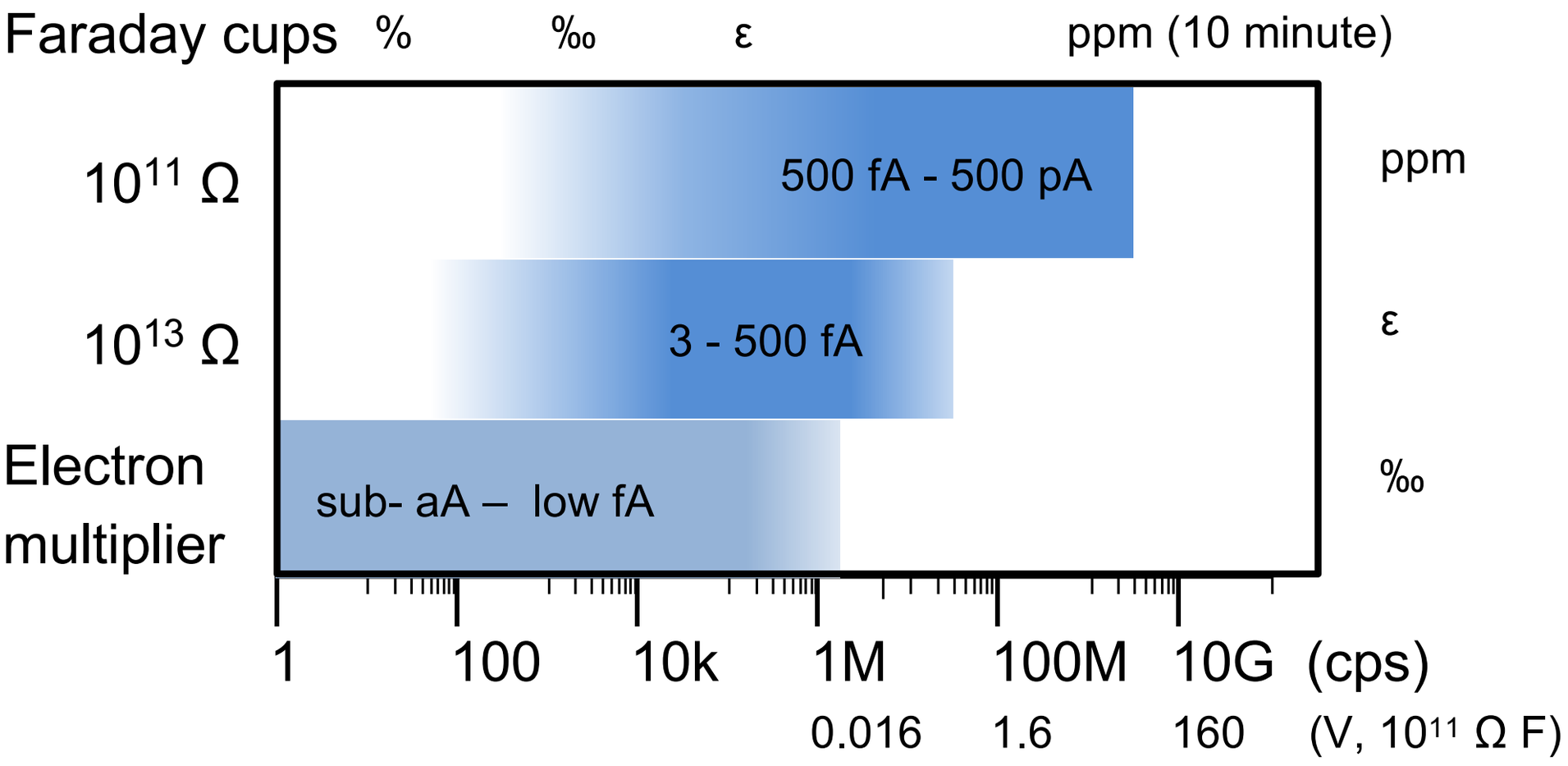
Faraday cups
%
‰
ε
ppm (10 minute)
10^11 Ω
500 fA - 500 pA
ppm
10^13 Ω
3 - 500 fA
ε
Electron multiplier
sub- aA – low fA
‰
1
100
10k
1M
100M
10G
(cps)
0.016
1.6
160
(V, 10^11 Ω F)
Beam intensity (log scale)

Fig. 19

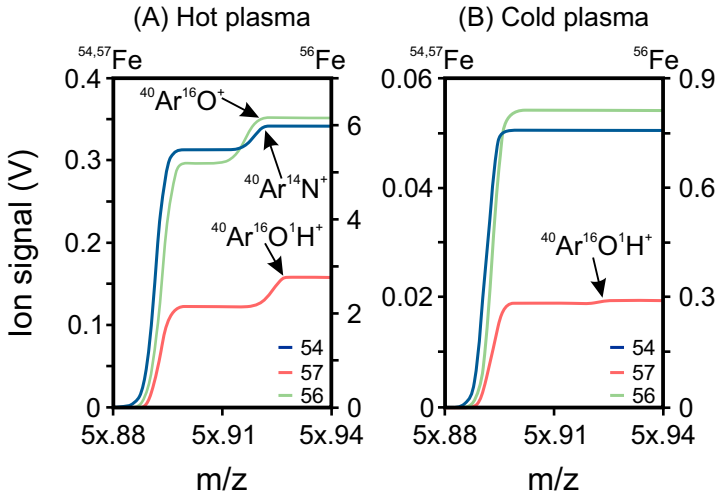
(A) Hot plasma
(B) Cold plasma
54,57Fe
56Fe
40Ar16O+
40Ar14N+
40Ar16O1H+
54
57
56
Ion signal (V)
m/z
5x.88
5x.91
5x.94
0.4
0.3
0.2
0.1
0
6
4
2
0.06
0.04
0.02
0.9
0.6
0.3

Fig. 20

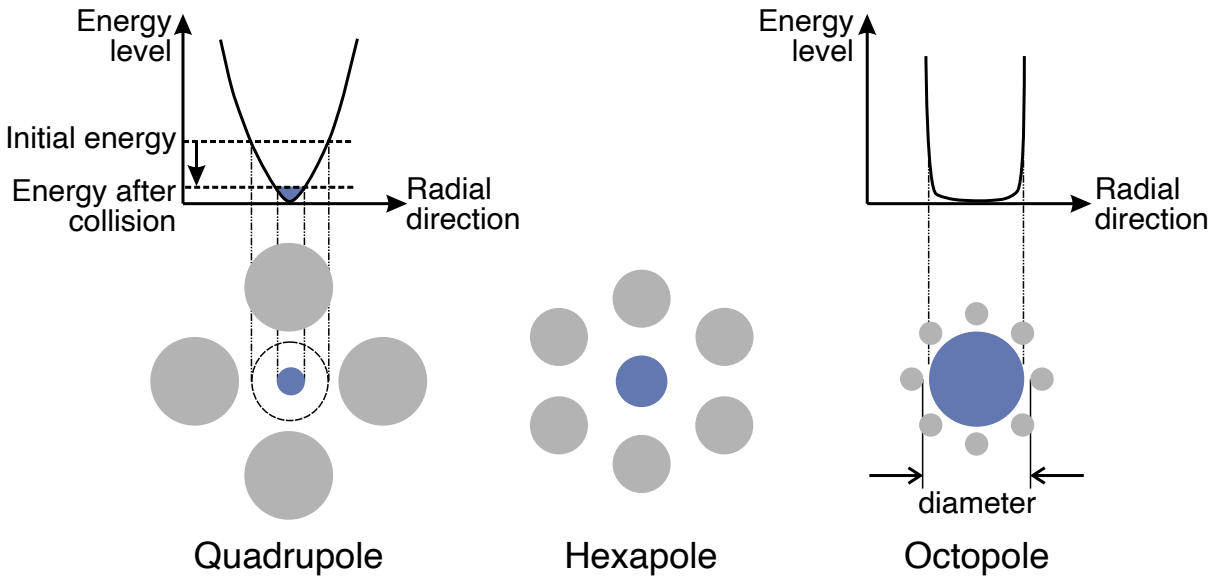
Energy level
Initial energy
Energy after collision
Radial direction
Quadrupole
Hexapole
Energy level
Radial direction
diameter
Octopole

Fig. 21

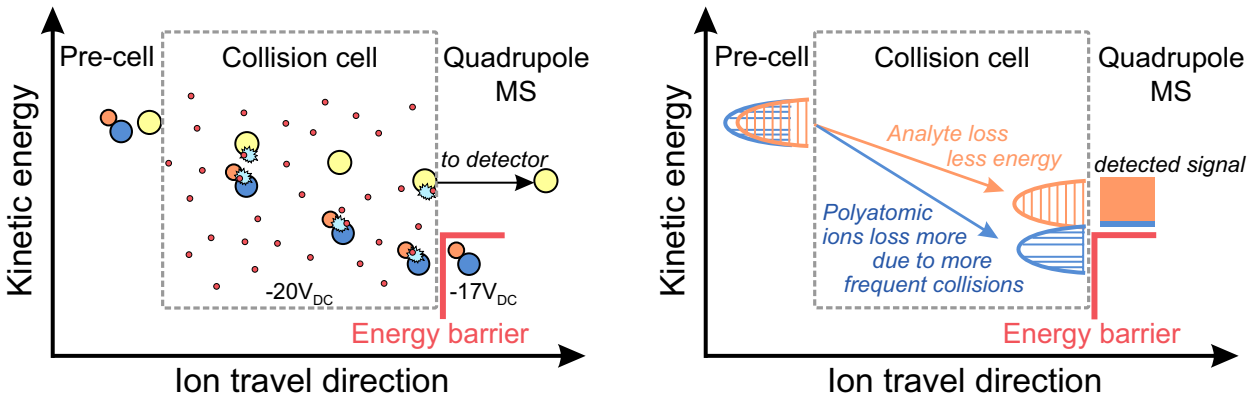
Pre-cell
Collision cell
Quadrupole MS
Kinetic energy
to detector
-20V$_{DC}$
-17V$_{DC}$
Energy barrier
Ion travel direction
Pre-cell
Collision cell
Quadrupole MS
Kinetic energy
Analyte loss less energy
detected signal
Polyatomic ions loss more due to more frequent collisions
Energy barrier
Ion travel direction

Fig. 22

(A) Collision mode

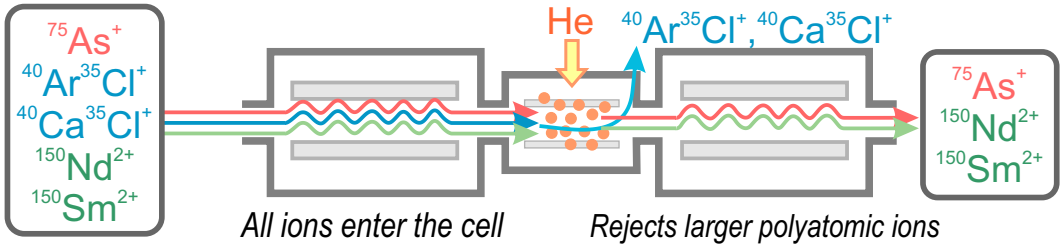

(B) On-mass reaction mode

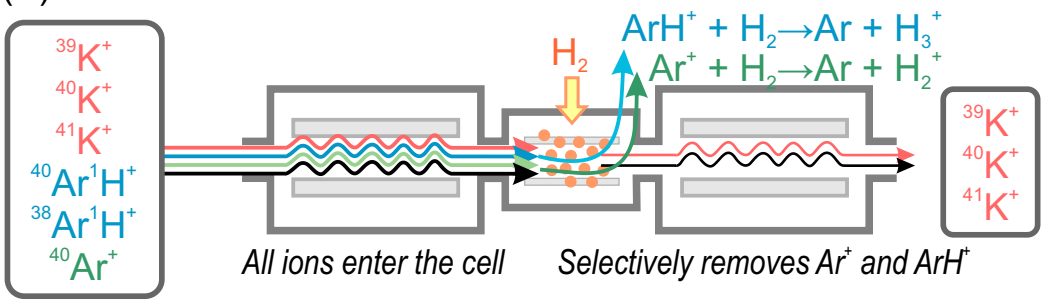

(C) Conventional mass-shift mode

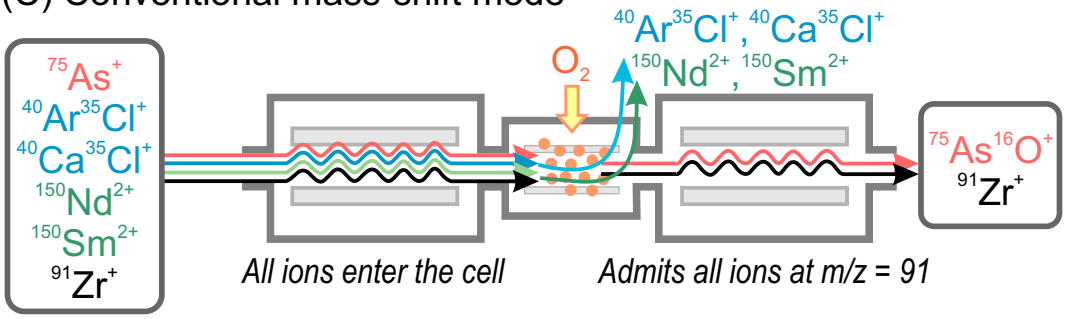

(D) Mass-shift mode with pre-cell mass filtering

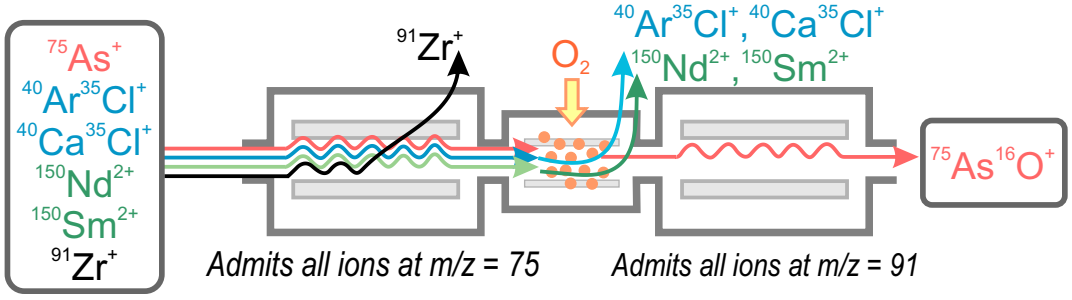

Fig. 23

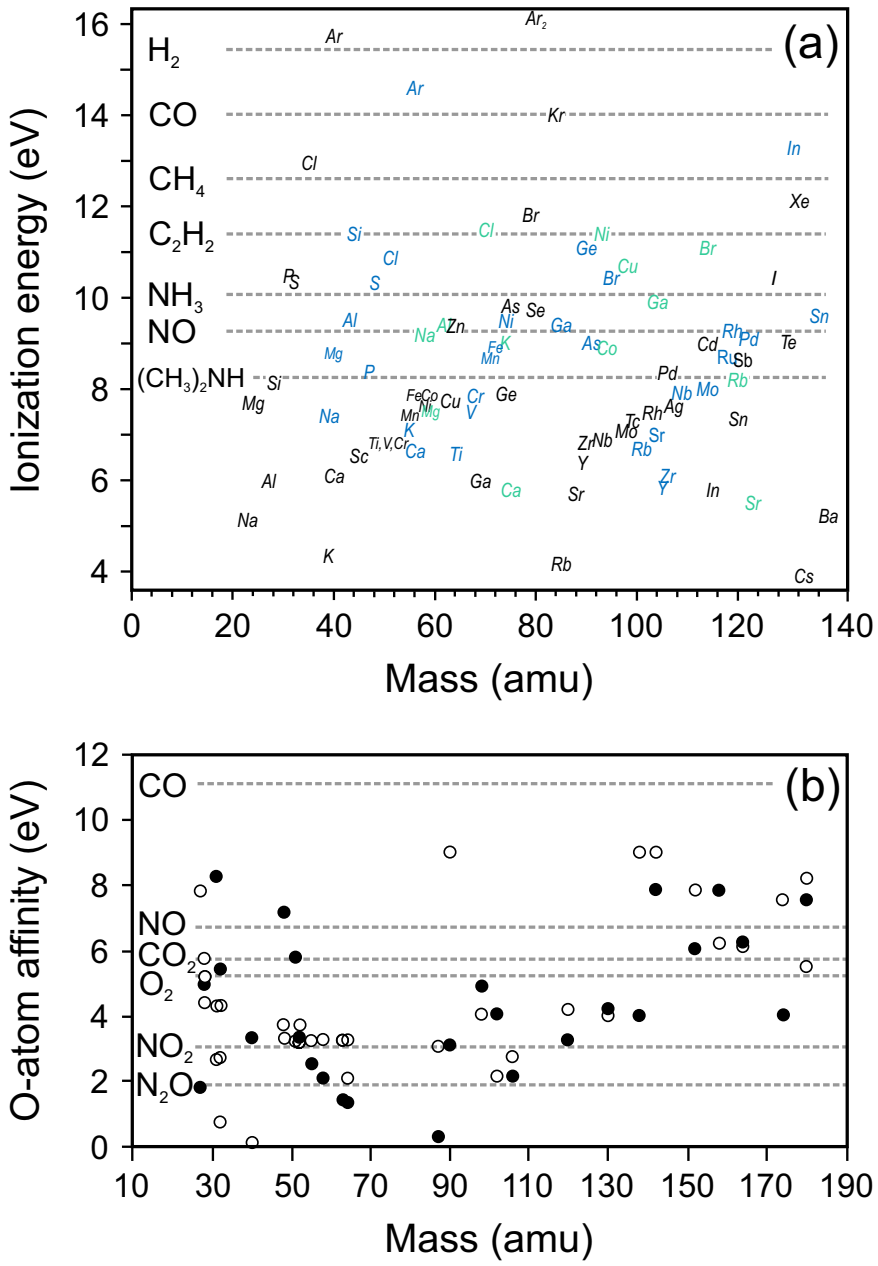
(a)
H2
CO
CH4
C2H2
NH3
NO
(CH3)2NH
Ionization energy (eV)
Mass (amu)
(b)
CO
NO
CO2
O2
NO2
N2O
O-atom affinity (eV)
Mass (amu)

Fig. 24

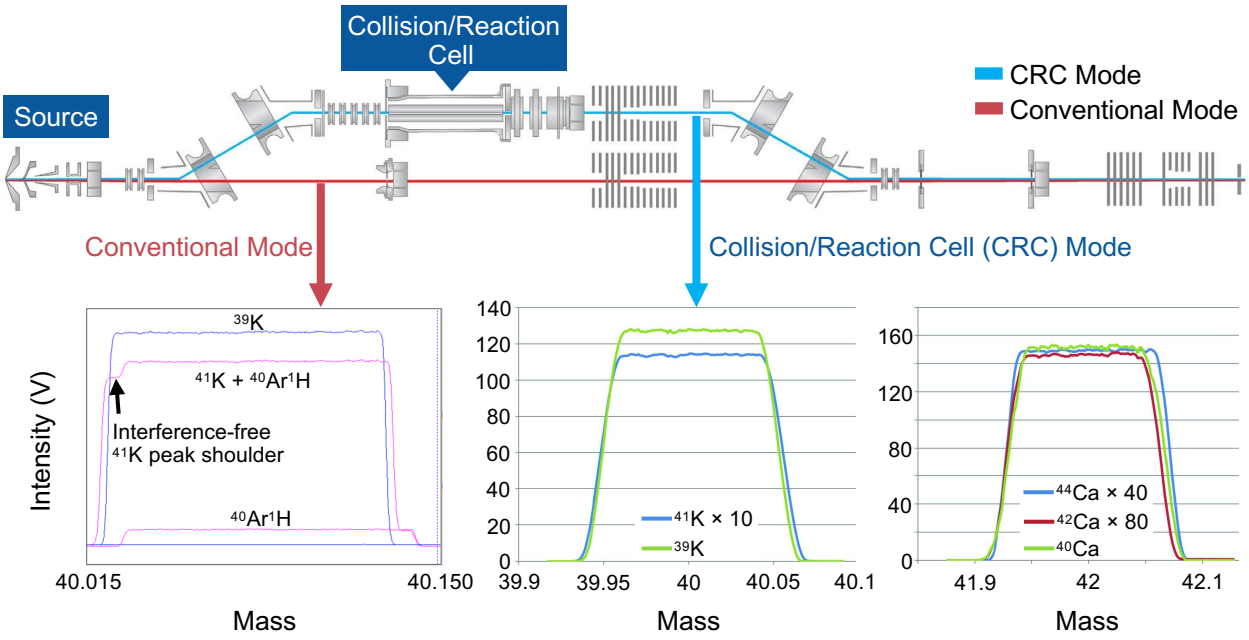
Collision/Reaction Cell
Source
CRC Mode
Conventional Mode
Conventional Mode
Collision/Reaction Cell (CRC) Mode
Intensity (V)
39K
41K + 40Ar1H
Interference-free
41K peak shoulder
40Ar1H
40.015
40.150
Mass
140
120
100
80
60
40
20
0
41K × 10
39K
39.9
39.95
40
40.05
40.1
Mass
160
120
80
40
0
44Ca × 40
42Ca × 80
40Ca
41.9
42
42.1
Mass

Fig. 25

(A) Prototype: Proteus

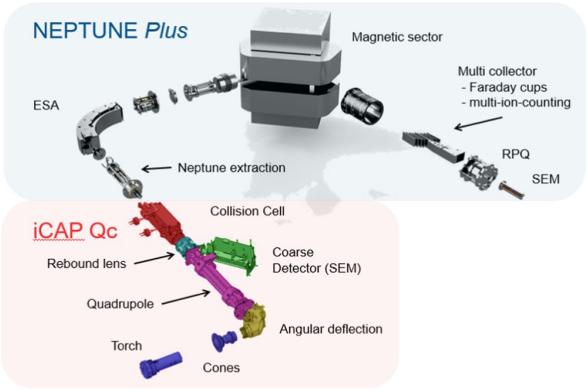

(B) Prototype: Vienna

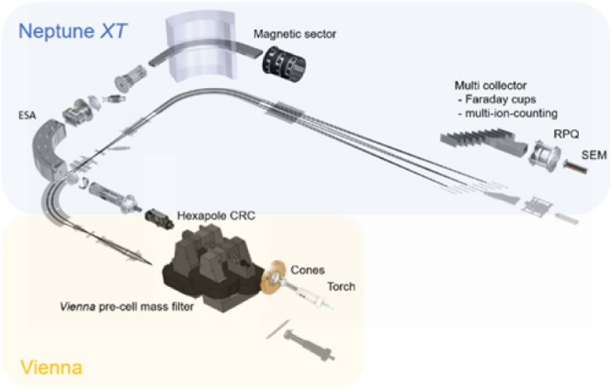

(C) Neoma

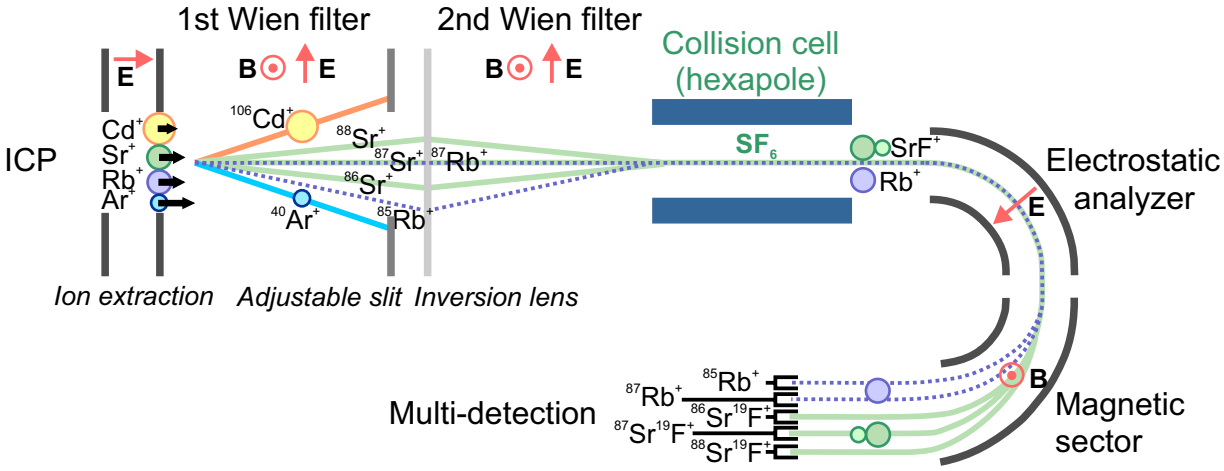

Fig. 26

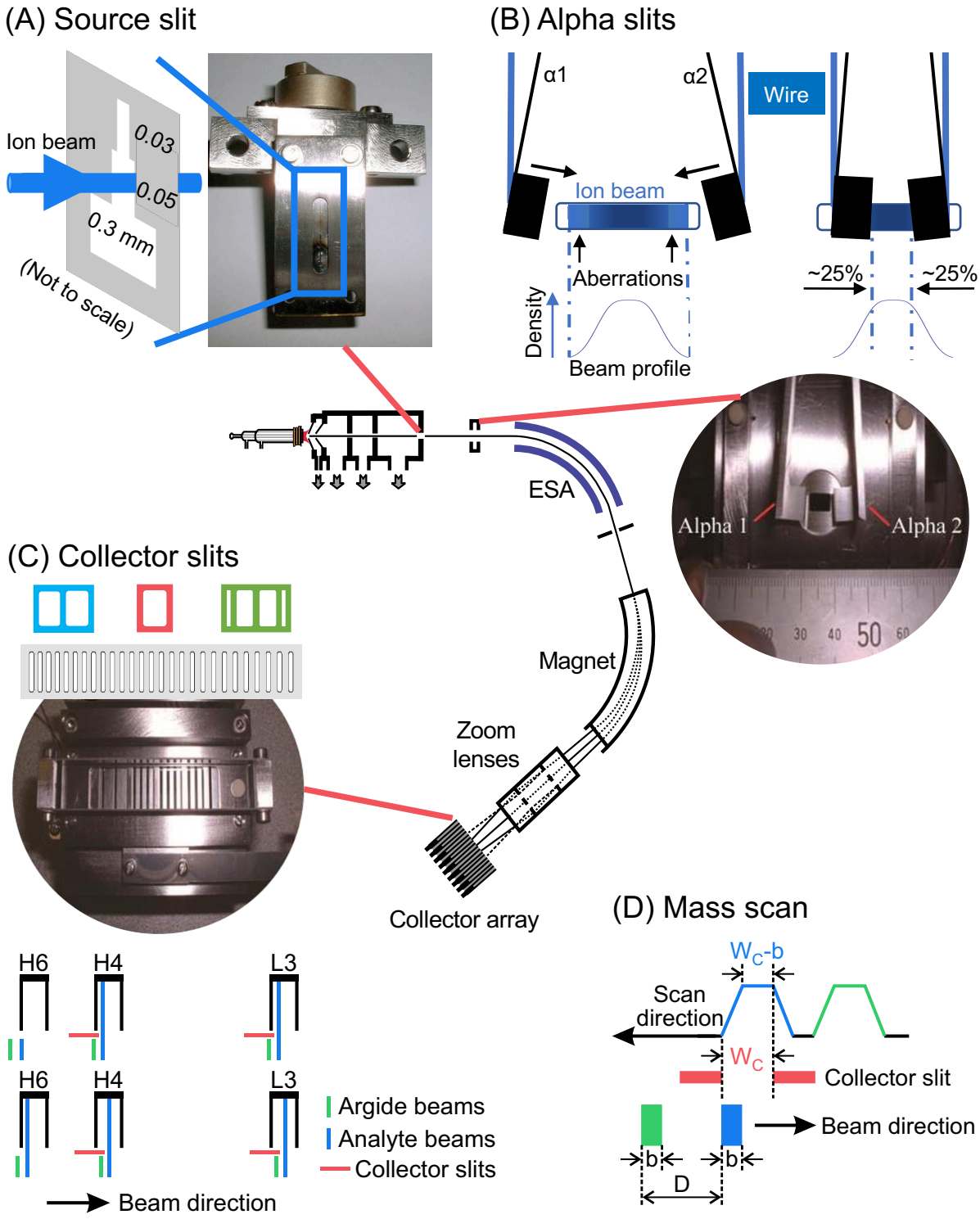
(A) Source slit
Ion beam
0.03
0.05
0.3 mm
(Not to scale)
(B) Alpha slits
α1
α2
Wire
Ion beam
Aberrations
Density
Beam profile
~25%
~25%
ESA
Alpha 1
Alpha 2
(C) Collector slits
Magnet
Zoom lenses
Collector array
(D) Mass scan
W_c-b
Scan direction
W_c
Collector slit
Beam direction
b
b
D
H6
H4
L3
H6
H4
L3
Argide beams
Analyte beams
Collector slits
Beam direction

Fig. 27

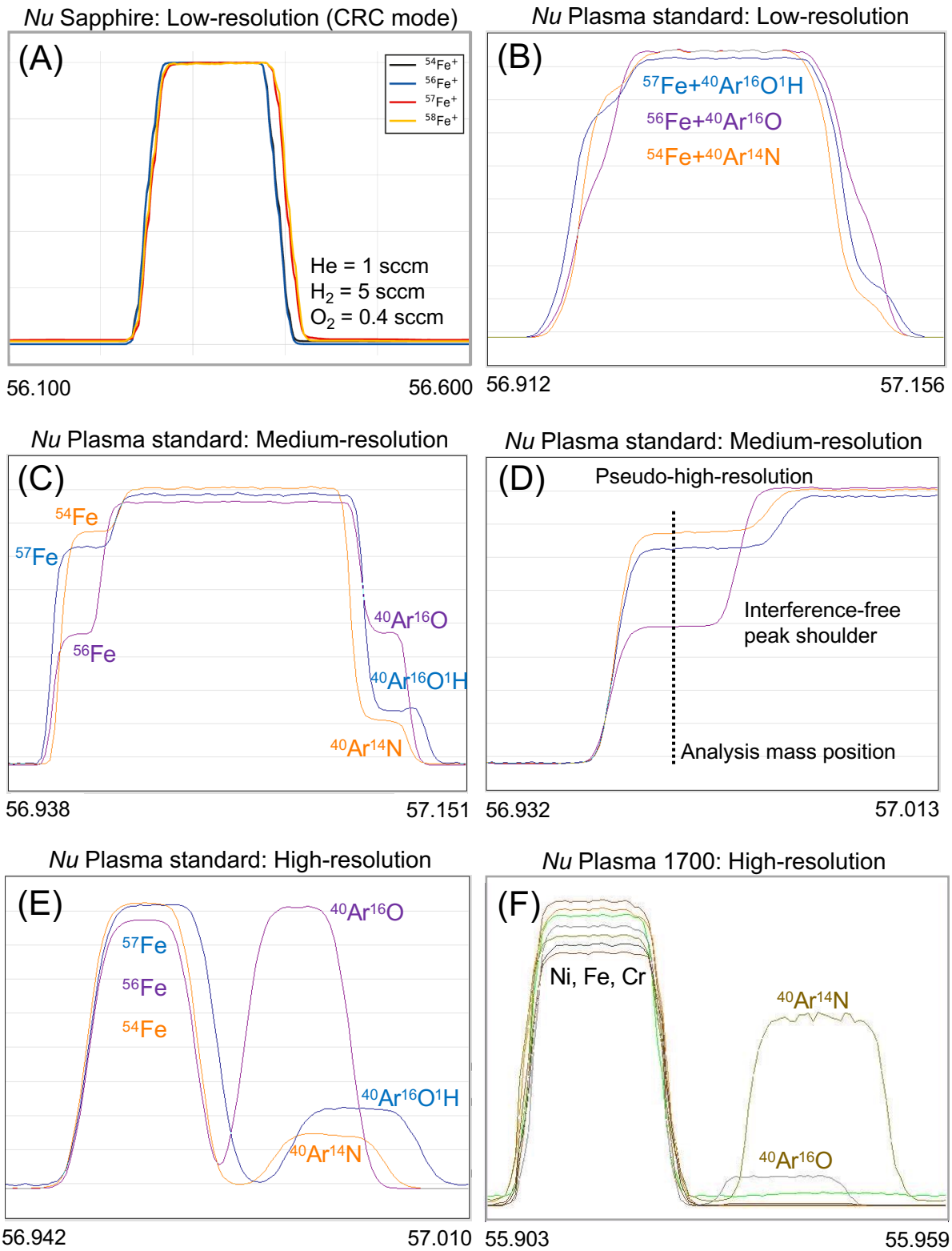
Nu Sapphire: Low-resolution (CRC mode)
(A)
$^{54}Fe^{+}$
$^{56}Fe^{+}$
$^{57}Fe^{+}$
$^{58}Fe^{+}$
He = 1 sccm
H_2 = 5 sccm
O_2 = 0.4 sccm
56.100
56.600
Nu Plasma standard: Low-resolution
(B)
$^{57}Fe+^{40}Ar^{16}O^{1}H$
$^{56}Fe+^{40}Ar^{16}O$
$^{54}Fe+^{40}Ar^{14}N$
56.912
57.156
Nu Plasma standard: Medium-resolution
(C)
^{54}Fe
^{57}Fe
^{56}Fe
$^{40}Ar^{16}O$
$^{40}Ar^{16}O^{1}H$
$^{40}Ar^{14}N$
56.938
57.151
Nu Plasma standard: Medium-resolution
(D)
Pseudo-high-resolution
Interference-free peak shoulder
Analysis mass position
56.932
57.013
Nu Plasma standard: High-resolution
(E)
$^{40}Ar^{16}O$
^{57}Fe
^{56}Fe
^{54}Fe
$^{40}Ar^{16}O^{1}H$
$^{40}Ar^{14}N$
56.942
57.010
Nu Plasma 1700: High-resolution
(F)
Ni, Fe, Cr
$^{40}Ar^{14}N$
$^{40}Ar^{16}O$
55.903
55.959

Fig. 28

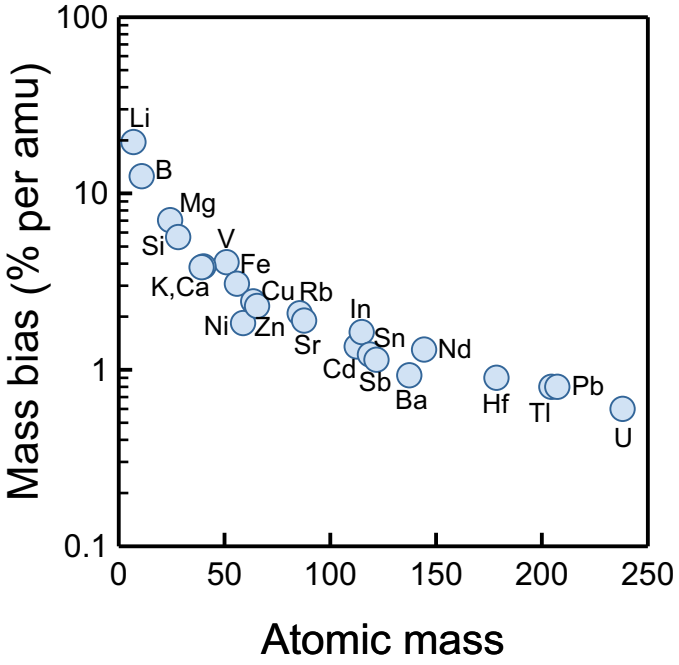
Mass bias (% per amu)
Atomic mass
100
10
1
0.1
0
50
100
150
200
250
Li
B
Mg
Si
V
Fe
K,Ca
Cu
Rb
In
Ni
Zn
Sr
Sn
Nd
Cd
Sb
Ba
Hf
Tl
Pb
U

Fig. 29